Optimization of Radiofrequency Coils for Human Brain Magnetic Resonance Spectroscopy at Ultra-High Field Strength

Dissertation

der Mathematisch-Naturwissenschaftlichen Fakultät

der Eberhard Karls Universität Tübingen

zur Erlangung des Grades eines

Doktors der Naturwissenschaften

(Dr. rer. nat.)

vorgelegt von

Andreas Manfred Pfrommer

aus Nagold

Tübingen

2017

Gedruckt mit Genehmigung der Mathematisch-Naturwissenschaftlichen Fakultät der Eberhard Karls Universität Tübingen.

Tag der mündlichen Qualifikation:	12.01.2018
Dekan:	Prof. Dr. Wolfgang Rosenstiel
1. Berichterstatter:	Prof. Dr. Anke Henning
2. Berichterstatter:	Prof. Dr. Klaus Scheffler

Acknowledgments

This PhD thesis would not have been possible without the support of many people who gave me inspiration and motivation to conduct this work.

I am very grateful to my supervisor Prof. Anke Henning for giving me the opportunity to do this PhD project, for her advice and fruitful discussions and for believing in my scientific ability. Further, I would like to thank my co-supervisor Prof. Klaus Scheffler for his continuous support and the board of examiners Prof. Fritz Schick and Prof. Reinhold Kleiner for the assessment of this thesis.

I am very grateful to all my former and current colleagues and friends at the Max Planck Institute: I enjoyed working with them and learning from them. In particular, it was a pleasure to collaborate with Nikolai and I appreciated our technical discussions about RF coil design. I learned a lot from his RF engineering skills. Also, I would like to thank Jens for his advice in electromagnetic field simulations and his postprocessing scripts for the SAR evaluation. I thank Ioannis for being my office mate and all the vital conversations we had during the PhD. Moreover, I thank Sahar, Andrew and Paul for proofreading this thesis.

Finally, and most importantly, I would like to express my heartfelt thanks to my parents Marianne and Manfred, to my siblings Susanne and Tobias and to my beloved Teresa. They gave me the most cordial encouragement, I could ever receive.

In deep gratitude, I thank the Lord.

Tübingen, October 2017   Andreas Pfrommer

Contents

Abbreviations

DGF . . . .   dyadic Green's function

FDTD . . . . . .   finite difference time domain

FEM . . . .   finite element method

FFT . . . .   fast Fourier transform

g-factor . . . . .   geometry factor

GPU . . . .   graphics processing unit

IEC . . . .   International Electrotechnical Commission

MR . . . .   magnetic resonance

MRS . . . .   magnetic resonance spectroscopy

NMR . . . .   nuclear magnetic resonance

RF . . . .   radiofrequency

ROI . . . .   region of interest

SAR . . . .   specific absorption rate

SNR . . . .   signal-to-noise ratio

UISNR . . . . .   ultimate intrinsic signal-to-noise ratio

Symbols

B_0 . . . .   static magnetic field

γ . . . .   gyromagnetic ratio

ω_0 . . . .   Larmor frequency

M_0 . . . .   equilibrium magnetization

B_1^+ . . . .   circularly polarized component of RF magnetic field, rotating with nuclear precession

B_1^- . . . .   circularly polarized component of RF magnetic field, rotating against nuclear precession

ϵ . . . .   electric permittivity

μ_0 . . . .   vacuum permeability

σ . . . .   electric conductivity

k . . . .   complex wave number

i . . . .   imaginary unit

$\mathbf{E}$ . . . .   electric field vector

$\mathbf{H}$ . . . .   magnetic field vector

$\mathbf{r}$ . . . .   position vector in 3D space

$\mathbf{r}'$ . . . .   source vector in 3D space

$\bar{\mathbf{G}}(\mathbf{r}, \mathbf{r}')$ . . . . .   dyadic Green's function

$\bar{\mathbf{I}}$ . . . .   unit dyad

$\mathbf{J}_\mathrm{s}$ . . . .   equivalent electric surface current density

$\mathbf{M}_\mathrm{s}$ . . . .   equivalent magnetic surface current density

$\delta_{nn'}$ . . . .   Kronecker delta

$\delta(\mathbf{v} - \mathbf{v}')$ . . .   Dirac's Delta distribution

α_i ....   expansion coefficient for basis set of equivalent surface currents

$\mathbf{K}_{\mathrm{bc}}$ ....   birdcage surface current distribution

φ ....   azimuthal variable in cylindrical coordinate system

z ....   z variable in cylindrical coordinate system

$H(z)$ ....   Heaviside step function

$w_{\mathrm{bc}}^{\mathrm{M}}$ ....   expansion coefficients for birdcage coil

J_0 ....   Bessel function of first kind and zeroth order

$\mathbf{K}$ ....   equivalent surface current distribution

$\alpha_{l,m}^{\mathrm{M}}$ ....   expansion coefficient for div-free current

$\alpha_{l,m}^{\mathrm{E}}$ ....   expansion coefficient for curl-free current

$\mathbf{X}_{l,m}$ ....   vector spherical harmonic

ϑ ....   elevation variable in spherical coordinates

ζ ....   total UISNR obtained from curl- and divergence-free current patterns

ζ^{E} ....   best possible SNR achievable with curl-free current patterns only

ζ^{M} ....   best possible SNR achievable with div-free current patterns only

ζ^{Φ} ....   best possible SNR achievable with Φ-directed current patterns only

ζ^{Z} ....   best possible SNR achievable with Z-directed current patterns only

ϑ_0 ....   spherical cap angle

Z_{12} ....   complex mutual impedance

k_{e} ....   electric coupling coefficient

k_{m} ....   magnetic coupling coefficient

R_{12} ....   mutual resistance

L_{12} ....   mutual inductance

R ....   total loop resistance

L ....   loop inductance

Q ....   quality factor of a loop

S_{12} ....   transmission scattering parameter

α_{cm} ....   critical overlap angle with $k_{\mathrm{m}} = 0$

α_{ce} ....   critical overlap angle with $k_{\mathrm{e}} = 0$

Abstract

Magnetic resonance spectroscopy (MRS) is a non-invasive and non-ionizing technique to acquire localized spectra of metabolites in vivo. With increasing static magnetic field strength B_0, the spectral separation of the metabolites and the signal-to-noise ratio (SNR) of the spectrum increase. Consequently, the number of detectable metabolites and the spatial specificity are enhanced at ultra-high fields ($B_0 \geq 7$ T). At the same time, the wavelength of the radiofrequency (RF) field is decreased. For proton spectroscopy at ultra-high fields, the wavelength of the RF field in tissue is smaller than the typical dimension of a human head. From the perspective of electromagnetic theory, this means that a quasistatic approximation of Maxwell's equations is not valid anymore and the electromagnetic field must be calculated with the full system of coupled partial differential equations. Therefore, RF coil designs based on the quasistatic approximation, such as the birdcage coil or loop-only receive arrays, have suboptimal performance at ultra-high fields.

This PhD project explored the optimization of RF coils for ultra-high field MRS. The optimization was based on an equivalent surface current distribution surrounding a human head model. It could be shown, that the equivalent surface current distribution can be separated into curl- and divergence-free components. The full-wave electromagnetic field problem was solved by a newly developed dyadic Green's functions approach.

As a first optimization goal, the SNR was maximized in a spherical- and later in a realistic human head model. By optimizing the complete set of curl- and divergence-free surface current components, an upper threshold for the achievable SNR of any receive array could be calculated; this so-called ultimate intrinsic SNR (UISNR) was studied at all practically relevant B_0 field strengths regarding human head applications. The UISNR increased superlinearly with B_0 in central regions of the human brain. In a next step, the SNR optimization was done separately for curl- and divergence-free current components. This yielded a direct performance measure of how close loop-only and dipole-only receive arrays were able to approach the UISNR in the human head. Based upon this analysis, field strength specific design guidelines for RF receive arrays were

deduced. In conclusion, at ultra-high field strength a combination of loop and dipole elements is necessary to achieve the best possible SNR at any position in the human head.

As a second optimization goal, the coupling of multi-channel RF arrays was minimized. For that, a fast analytical model describing the complex mutual coupling between two surface loops was introduced. To understand and eliminate both electric and magnetic coupling between the loops, the influence of the loop geometry and loading by the sample was systematically examined. For the first time, it was demonstrated that at 400 MHz it is possible to eliminate both, electric and magnetic coupling simultaneously by proper adjustment of the loop width and overlap. A fully decoupled two channel prototype array was constructed having superior transmit and receive performance over a previously used gapped design.

Zusammenfassung

Die Magnetresonanz-Spektroskopie ist ein nichtinvasives und nichtionisierendes In-vivo-Verfahren mit dem Stoffwechselvorgänge im menschlichen Körper ortsaufgelöst erfasst werden können. Mit zunehmender statischer Feldstärke B_0 vergrößert sich sowohl die relative Frequenzverschiebung der Metaboliten zueinander, als auch das Signal-zu-Rauschverhältnis (SNR) des gesamten Spektrums. Infolgedessen können im Ultrahochfeld ($B_0 \geq$ 7 T) eine größere Anzahl an Metaboliten unterschieden werden. Ein weiterer Vorteil der Ultrahochfeld-Spektroskopie besteht darin, dass sich die Metaboliten mit höherer örtlicher Spezifität erfassen lassen. Gleichzeitig weist das von einer Hochfrequenzspule angeregte elektromagnetische Wechselfeld eine kürzere Wellenlänge auf. In menschlichem Gewebe unterschreitet die Wellenlänge des Hochfrequenzfeldes bei Protonenanregung im Ultrahochfeld die typischen Abmessungen des menschlichen Kopfes. Vom Standpunkt der elektromagnetischen Feldtheorie aus betrachtet bedeutet dies, dass eine quasistatische Näherung der Maxwell-Gleichungen nicht mehr anwendbar ist und das vollständige, gekoppelte, partielle Differentialgleichungssystem gelöst werden muss. Daher ist die Leistungsfähigkeit herkömmlicher Spulenkonzepte (z.B. Birdcage Spule oder Schleifenarrays), die auf einer quasistatischen Näherung beruhen, im Ultrahochfeld suboptimal.

Im Rahmen dieser Promotion wurde die Optimierung von Hochfrequenzspulen für die Hochfeldmagnetresonanz-Spektroskopie erforscht. Als Optimierungsvariable wurde eine äquivalente Oberflächenstromverteilung definiert, die den menschlichen Kopf umgab. Es wurde gezeigt, dass diese Oberflächenstromverteilung in divergenz- und rotationsfreie Komponenten zerlegt werden kann. Das elektromagnetische Feldproblem wurde mithilfe eines neuartigen Ansatzes, der auf dyadischen Green'schen Funktionen beruht, gelöst.

Das erste Optimierungsziel bestand darin, das SNR in einem kugelförmigen, später in einem realistischen Kopfmodell zu maximieren. Zunächst wurde die vollständige Oberflächenstromverteilung aus divergenz- und rotationsfreien Komponenten optimiert. Auf diese Weise konnte das bestmöglich erzielbare SNR beliebiger Empfangsarrays ange-

geben werden. Dieses optimale intrinsische SNR (UISNR) wurde für sämtliche, praktisch relevante Magnetfeldstärken im menschlichen Kopf untersucht. Dabei stieg das UISNR in zentralen Hirnregionen überproportional mit der Magnetfeldstärke an. Als nächstes wurde die Fragestellung eruiert, inwieweit sich der zuvor theoretisch ermittelte SNR-Grenzwert mit Schleifen- bzw. Dipolarrays erreichen lässt. Dazu wurde die Optimierung jeweils mit divergenz- und rotationsfreien Oberflächenstromkomponenten separat durchgeführt und entsprechende Kenngrößen für die Empfangseigenschaften von Schleifen- und Dipolarrays abgeleitet. Aus diesen Ergebnissen wurden frequenzabhängige Designrichtlinien für Hochfrequenz-Empfangsspulen formuliert. Es zeigte sich, dass eine Kombination aus Schleifen- und Dipolelementen im Ultrahochfeld unerlässlich ist, um das bestmögliche SNR im menschlichen Kopf zu erzielen.

Das zweite Optimierungsziel bestand darin, die Kopplung von Mehrkanal-Antennenarrays zu minimieren. Zunächst wurden der elektrische und magnetische Koppelfaktor zweier benachbarter Leiterschleifen durch ein neu entwickeltes analytisches Modell beschrieben. Mithilfe des neu entwickelten Modells wurden anschließend die Schleifengeometrie und der Abstand der Schleifen zu einem zylinderförmigen Kopfmodell systematisch variiert. So konnte erstmals gezeigt werden, dass durch geschickte Überlappung und eine optimierte Schleifenbreite bei 400 MHz die elektrische und die magnetische Kopplung gleichzeitig ausgelöscht werden können. Als Machbarkeitsstudie wurde ein vollständig entkoppeltes Zweikanalarray aufgebaut und mit einem früheren Design aus nicht-überlappenden Schleifenelementen verglichen. Das neu entwickelte, überlappende Arraydesign zeigte signifikant verbesserte Sende- und Empfangseigenschaften gegenüber der früheren Version.

Publication List

First-author articles, on which this thesis is based

1. Pfrommer A, Henning A. On the contribution of curl-free current patterns to the ultimate intrinsic signal-to-noise ratio at ultra-high field strength. *NMR Biomed.* 2017;30:e3691.

2. Pfrommer A, Henning A. The ultimate intrinsic signal-to-noise ratio of loop- and dipole-like current patterns in a realistic human head model. *Magn Reson Med.* 2018. doi: 10.1002/mrm.27169.

3. Pfrommer A, Henning A. On the superlinear increase of the ultimate intrinsic signal-to-noise ratio with regard to main magnetic field strength in a spherical sample. *IEEE International Conference on Electromagnetics in Advanced Applications (ICEAA).* 2017; 684-687.

4. Avdievich* NI, Pfrommer* A, Giapitzakis IA, Henning A. Analytical modeling provides new insight into complex mutual coupling between surface loops at ultrahigh fields. *NMR in Biomed.* 2017;30:e3759. (* . . . shared first-authorship)

Co-authored articles, which are not part of this thesis

5. Avdievich NI, Hoffmann J, Shajan G, Pfrommer A, Giapitzakis IA, Scheffler K, Henning A. Evaluation of transmit efficiency and SAR for a tight fit transceiver human head phased array at 9.4 T. *NMR in Biomed.* 2017;30:e3680.

6. Avdievich NI, Giapitzakis IA, Pfrommer A, Henning A. Decoupling of a tight-fit transceiver phased array for human brain imaging at 9.4T: loop overlapping rediscovered. *Magn Reson Med.* 2018;79:1200-1211 .

7. Avdievich NI, Giapitzakis IA, Pfrommer A, Borbath T, Henning A. Combination of surface and "vertical" loop elements improves receive performance of a human head transceiver array at 9.4 T. *NMR Biomed.* 2018;31:e3878 .

First-author conference proceedings, which resulted in an oral presentation

8. Pfrommer A, Henning A. On the contribution of electric-type current patterns to UISNR for a spherical geometry at 9.4 T. *Proceedings of the 23rd Annual Meeting of ISMRM*, Toronto, Canada; 2015. p 856. (summa cum laude).

9. Pfrommer A, Henning A. Optimal arrangement of finite element loop arrays for parallel magnetic resonance imaging in the human head at 400 MHz. *IEEE MTT-S International Microwave Symposium*, Phoenix, USA; 2015. p 1-4.

10. Pfrommer A, Henning A. About the ultimate SNR for cylindrical and spherical RF arrays in a realistic human head model. *Proceedings of the 24th Annual Meeting of ISMRM*, Singapore, Singapore; 2016. p 175.

11. Pfrommer A, Henning A. Comparison of the ultimate intrinsic SNR in a spherical phantom vs a realistic human head model at 9.4 T. *Proceedings of the 33rd Annual Meeting of the ESMRMB*, Vienna, Austria; 2016. p 329.

12. Pfrommer A, Henning A. The ultimate intrinsic SNR in a spherical phantom with regard to an open-pole surface current distribution at 9.4T. *Proceedings of the 25th Annual Meeting of ISMRM*, Honolulu, USA; 2017. p 749.

Other contributions to conference proceedings

13. Pfrommer A, Avdievich N, Henning A. Four channel transceiver array for functional magnetic resonance spectroscopy in the human visual cortex at 9.4 T. *Proceedings of the 22nd Annual Meeting of ISMRM*, Milano, Italy; 2014. p 1305.

14. Avdievich NI, Pfrommer A, Hoffmann J, Chadzynski GL, Scheffler K, Henning A. Transceive phased array with high transmit performance for human brain application at 9.4 T. *Proceedings of the 22nd Annual Meeting of ISMRM*, Milano, Italy; 2014. p 622.

15. Pfrommer A, Henning A. Optimal arrangement of finite element loop arrays for parallel imaging in a spherical geometry at 9.4 T. *Proceedings of the 23rd Annual Meeting of ISMRM*, Toronto, Canada; 2015. p 3165.

16. Pfrommer A, Avdievich NI, Henning A. Effect of the RF shield on the mutual coupling between adjacent and non-adjacent array elements. *Proceedings of the 24th Annual Meeting of the ISMRM*, Singapore, Singapore; 2016. p 2159.

17. Avdievich NI, Pfrommer A, Giapitzakis IA, Henning A. Analytical modeling of the coupling within a human head surface loop transmit phased array at ultra-high fields. *Proceedings of the 24th Annual Meeting of ISMRM*, Singapore, Singapore; 2016. p 3525.

18. Avdievich NI, Giapitzakis IA, Pfrommer A, Henning A. Optimization of the transceiver phased array for human brain imaging at 9.4T: loop overlapping rediscovered. *Proceedings of the 24th Annual Meeting of ISMRM*, Singapore, Singapore; 2016. p 169.

Statement of Contributions

<u>PUBLICATION 1:</u> Pfrommer A, Henning A. On the contribution of curl-free current patterns to the ultimate intrinsic signal-to-noise ratio at ultra-high field strength. *NMR Biomed.* 2017;30:e3691.

A. Pfrommer	He had the idea to systematically investigate the different contributions of curl- and divergence-free current patterns to the UISNR in a spherical head model. He developed the necessary Matlab code to do the electromagnetic simulations. Moreover, he prepared the manuscript.
A. Henning	She was the project supervisor and gave advice on the manuscript.

<u>PUBLICATION 2:</u> Pfrommer A, Henning A. The ultimate intrinsic signal-to-noise ratio of loop- and dipole-like current patterns in a realistic human head model. *Magn Reson Med.* 2018. doi: 10.1002/mrm.27169.

A. Pfrommer	He had the idea to expand the work of the first publication to a realistic human head model. He developed the necessary Matlab code for the electromagnetic simulations by himself, except for the fast volume integral equation solver "MARIE", which was written by Jorge Villena, Athanasios Polimeridis and José Serrallés at Massachusetts Institute of Technology. Andreas Pfrommer prepared the manuscript.
A. Henning	She was the project supervisor and gave advice on the manuscript.

<u>PUBLICATION 3:</u> Pfrommer A, Henning A. On the superlinear increase of the ultimate intrinsic signal-to-noise ratio with regard to main magnetic field strength in a spherical sample. *IEEE International Conference on Electromagnetics in Advanced Applications (ICEAA).* 2017; 684-687.

A. Pfrommer He had the idea to study the increase of the UISNR with regard to main magnetic field strength. He wrote the Matlab code and did all the simulations. He prepared the manuscript.

A. Henning She was the project supervisor and gave advice on the manuscript.

PUBLICATION 4: Avdievich* NI, Pfrommer* A, Giapitzakis IA, Henning A. Analytical modeling provides new insight into complex mutual coupling between surface loops at ultrahigh fields. *NMR in Biomed.* 2017;30:e3759.

A. Pfrommer He, together with Nikolai Avdievich, had the idea to investigate the complex mutual coupling between surface loops. Andreas Pfrommer developed the analytic model and programmed Matlab code for the electromagnetic simulations. Moreover, he was responsible for the FEM simulations in CST Mircowave Studio. Together with Nikolai Avdievich, he prepared the manuscript.

N. Avdievich He constructed the prototype arrays and was responsible for the bench measurements with the network analyzer. Moreover, he prepared the manuscript together with Andreas Pfrommer.

I. Giapitzakis He did the SNR and B_1^+ measurements at the 9.4 T scanner. He reconstructed the measured data.

A. Henning She was the project supervisor and gave advice on the manuscript.

1 Introduction

1.1 The Role of RF Coils in MR Spectroscopy

To start with, let a proton be exposed to a constant, homogeneous magnetic field $\mathbf{B}_0 = B_0\mathbf{e}_z$. Then, the expectation value of its magnetic moment is precessing around the z-axis. The Larmor frequency of this precession is given by

$$\omega_0 = -\gamma B_0, \qquad\qquad [1.1]$$

where γ is the gyromagnetic ratio of the isotope (e.g. ^{1}H = 42.576 MHz/T). For an ensemble of spins, it can be shown, that in thermodynamic equilibrium, the net nuclear magnetization vector $\mathbf{M}$ only has a longitudinal component (1): $\mathbf{M} = M_0\mathbf{e}_z$. Here, M_0 is the equilibrium magnetization and is constant in time. However, the longitudinal net nuclear magnetization is about four orders of magnitude lower than the diamagnetism of the electrons and therefore hardly detectable (1). For this reason, in MRS the net magnetization, which is perpendicular to the magnetic field B_0, is measured. In order to generate transverse magnetization, a transmit RF coil is used. Thereby, a modulated RF pulse is played out at the carrier frequency ω_0 and fed to the coil. The circularly polarized component $B_1^+ = 0.5\,(B_x + \mathrm{i}B_y)$ of the coil's RF magnetic field rotates in the same direction as nuclear precession $(2,3)$ and flips the net magnetization by the flip angle α from the z-axis. The specific value of α depends on the parameters of the pulse and the state of the spin system. Directly after the RF pulse, there is a transverse component of the net magnetization vector, which is proportional to $\sin(\alpha)$. This transverse component oscillates with the Larmor frequency and induces an electromotive force in a sensitive receive RF coil. The receive sensitivity of the RF coil is determined by the circularly polarized component $B_1^- = 0.5\,(B_x - \mathrm{i}B_y)^*$ rotating in opposite direction as nuclear precession $(2,3)$.

1.2 A Basis Set for the Equivalent Surface Current Distribution

For the optimization of RF coils, it is useful to optimize a current distribution with respect to a given objective function. This current distribution can be spanned by a basis set of equivalent surface current modes, which are able to excite all possible solutions of Maxwell's equations in the sample of interest (e.g. the human head). In the following, a mathematical derivation of the basis set of equivalent surface currents is provided.

A simple, two-region model for the scattering problem of an RF antenna irradiating a dielectric sample is given in figure 1.1. The RF antenna is placed in free-space exterior to the sample, which occupies a regular region $\mathcal{D}$ and is bounded by the closed surface S. Let us assume linear, time-invariant, homogeneous and isotropic material properties with permittivity ϵ and conductivity σ. Suppose, there are no free volume charges within the dielectric sample and hence $\nabla \mathbf{E} = 0$. Then the homogeneous vector Helmholtz equation for the electric field is given by:

$$\nabla \times \nabla \times \mathbf{E}(\mathbf{r}) - k^2 \mathbf{E}(\mathbf{r}) = 0 \quad \text{with } \mathbf{r} \in \mathcal{D}. \qquad [1.2]$$

According to equation [8.1.27] in (4), the solution of the electromagnetic field in the sample can be expressed as a surface integral :

$$\mathbf{E}(\mathbf{r}) = \oint_S -\mathrm{i}\omega\mu_0 \bar{\mathbf{G}}(\mathbf{r}, \mathbf{r}') \cdot \mathbf{n}' \times \mathbf{H}(\mathbf{r}') + (\nabla' \times \bar{\mathbf{G}}(\mathbf{r}, \mathbf{r}')) \cdot \mathbf{n}' \times \mathbf{E}(\mathbf{r}') \, dS' \quad \text{with } \mathbf{r} \in \mathcal{D}. \ [1.3]$$
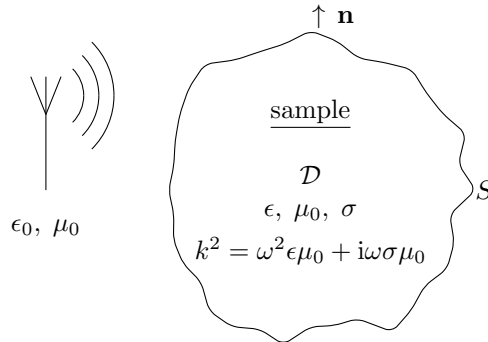

Figure 1.1: Simple mathematical model for the homogeneous Helmholtz equation in a dielectric, lossy sample.

Here, $\bar{\mathbf{G}}(\mathbf{r}, \mathbf{r}')$ is the unbounded medium dyadic Green's function:

$$\bar{\mathbf{G}}(\mathbf{r}, \mathbf{r}') = \left(\bar{\mathbf{I}} + \frac{\nabla \nabla}{k^2} \right) \frac{\mathrm{e}^{\mathrm{i}k|\mathbf{r} - \mathbf{r}'|}}{4\pi |\mathbf{r} - \mathbf{r}'|}. \tag{1.4}$$

The terms $-\mathbf{n}' \times \mathbf{H}(\mathbf{r}')$ and $\mathbf{n}' \times \mathbf{E}(\mathbf{r}')$ in equation 1.3 specify the boundary conditions on S and can be interpreted as equivalent electric and magnetic surface currents $\mathbf{J}_{\mathrm{s}}$ and $\mathbf{M}_{\mathrm{s}}$. Theses currents are induced from the RF antenna in the exterior region and can be obtained by solving a system of integral equations of the scattering problem. For the ongoing discussion, not the whole scattering problem is regarded but the equivalent surface currents are treated as direct sources exciting an electromagnetic field in the sample. Under the assumption of a lossy sample ($\sigma > 0$), the uniqueness theorem states (5), that the electromagnetic field in the sample is uniquely defined by either $\mathbf{J}_{\mathrm{s}}$ or $\mathbf{M}_{\mathrm{s}}$ or parts of both over the entire surface S. As a result, the electromagnetic field can be expressed in terms of an equivalent electric surface current density $\mathbf{J}_{\mathrm{s}}$:

$$\mathbf{E}(\mathbf{r}) = \oint_S \mathrm{i}\omega\mu_0 \bar{\mathbf{G}}(\mathbf{r}, \mathbf{r}') \cdot \mathbf{J}_{\mathrm{s}}(\mathbf{r}') \, dS'. \tag{1.5}$$

In the next step, an eigenfunction expansion of $\bar{\mathbf{G}}(\mathbf{r}, \mathbf{r}')$ is required. According to equation 4.64 in (6), the unbounded dyadic Green's function (DGF) may be represented by a combination of discrete and improper continuous eigenfunctions:

$$\bar{\mathbf{G}}(\mathbf{r}, \mathbf{r}') = \sum_{n=1}^{\infty} \frac{\mathbf{x}_n(\mathbf{r})\mathbf{x}_n^*(\mathbf{r}')}{\lambda_n - k^2} + \int_{\mathbf{v}} \frac{\mathbf{x}(\mathbf{r}, \mathbf{v})\mathbf{x}^*(\mathbf{r}', \mathbf{v})}{\lambda(\mathbf{v}) - k^2} \, d\mathbf{v}. \tag{1.6}$$

The discrete eigenfunctions are defined by the eigenvalue problem $\nabla \times \nabla \times \mathbf{x}_n(\mathbf{r}) = \lambda_n \mathbf{x}_n(\mathbf{r})$ and form an orthonormal set with $\langle \mathbf{x}_n(\mathbf{r}), \mathbf{x}_{n'}(\mathbf{r}) \rangle = \delta_{nn'}$. The improper eigenfunctions satisfy the equation $\nabla \times \nabla \times \mathbf{x}(\mathbf{r}, \mathbf{v}) = \lambda(\mathbf{v})\mathbf{x}(\mathbf{r}, \mathbf{v})$ and obey the completeness relation $\langle \mathbf{x}(\mathbf{r}, \mathbf{v}), \mathbf{x}(\mathbf{r}, \mathbf{v}') \rangle = \delta(\mathbf{v} - \mathbf{v}')$. Further, let $\langle \mathbf{x}_n(\mathbf{r}), \mathbf{x}(\mathbf{r}, \mathbf{v}) \rangle = 0$. Now, the electric surface current density $\mathbf{J}_{\mathrm{s}}$ can be defined. It is favorable to use a similar spectral representation as for the DGF in equation 1.6:

$$\mathbf{J}_{\mathrm{s}} = \sum_{n=1}^{\infty} \alpha_n \mathbf{y}_n(\mathbf{r}) + \int_{\mathbf{v}} \alpha(\mathbf{v})\mathbf{y}(\mathbf{r}, \mathbf{v}) \, d\mathbf{v}. \tag{1.7}$$

The eigenfunctions $\mathbf{y}_n(\mathbf{r})$ and $\mathbf{y}(\mathbf{r}, \mathbf{v})$ may fulfill the following conditions:

$$\oint_S \mathbf{x}_n^*(\mathbf{r}') \cdot \mathbf{y}_{n'}(\mathbf{r}') \, dS' = \delta_{n,n'} \qquad [1.8]$$

$$\oint_S \mathbf{x}^*(\mathbf{r}', \mathbf{v}) \cdot \mathbf{y}(\mathbf{r}', \mathbf{v}') \, dS' = \delta(\mathbf{v} - \mathbf{v}') \qquad [1.9]$$

$$\oint_S \mathbf{x}_n^*(\mathbf{r}') \cdot \mathbf{y}(\mathbf{r}', \mathbf{v}) \, dS' = 0 \qquad [1.10]$$

$$\oint_S \mathbf{x}^*(\mathbf{r}', \mathbf{v}) \cdot \mathbf{y}_{n'}(\mathbf{r}') \, dS' = 0. \qquad [1.11]$$

Then, the basis set defined in equation 1.7 is able to excite all possible solutions of the homogeneous Helmholtz equation in the sample domain $\mathcal{D}$. To represent this basis set on a computer with finite numerical precision, the continuous eigenvectors $\mathbf{y}(\mathbf{r}, \mathbf{v})$ need to be discretized:

$$\mathbf{J}_s(\mathbf{r}) = \sum_{n=1}^{\infty} \alpha_n \mathbf{y}_n(\mathbf{r}) + \sum_{v=1}^{\infty} \alpha_v \mathbf{y}_v(\mathbf{r}) = \sum_{i=1}^{\infty} \alpha_i \mathbf{y}_i(\mathbf{r}). \qquad [1.12]$$

Additionally, the infinite sum needs to be truncated:

$$\mathbf{J}_s(\mathbf{r}) = \sum_{i=1}^{N} \alpha_i \mathbf{y}_i(\mathbf{r}). \qquad [1.13]$$

Equation 1.13 can be used as a basis set for the optimization process. If the surface S is confined to a Cartesian, cylindrical or spherical coordinate system (which is the case throughout this thesis), there are closed-form expressions of equation 1.6 and 1.7. More details can be found in (7–9).

1.3 The Optimization Problem

With the basis set of equivalent surface currents from equation 1.13 it is possible to formulate an optimization problem. The optimization variables are the complex expansion coefficients α_i from the basis set of equivalent surface current modes. The most common optimization goals are summarized in table 1.1. The solution of the optimization problem yields expansion coefficients α_i^{opt}. The optimal surface current distribution is given by:

$$\mathbf{J}_{\mathrm{s}}^{\mathrm{opt}}(\mathbf{r}) = \sum_{i=1}^{N} \alpha_i^{\mathrm{opt}} \mathbf{y}_i(\mathrm{r}). \qquad [1.14]$$

Transmit Mode	
$\min\limits_{\alpha_i} \mathrm{std}\lvert B_1^+\rvert$	Homogeneous B_1^+-component over a specified region of interest (ROI): This criterion is important to ensure a homogeneous distribution of the flip angle over the ROI.
$\max\limits_{\alpha_i} \lvert B_1^+\rvert/\sqrt{P_{\mathrm{in}}}$	High transmit efficiency: The input RF power to the RF coil P_{in} is limited by the maximum power available from the RF amplifier minus the losses on the transmission lines connecting the amplifier with the coil.
$\max\limits_{\alpha_i} \lvert B_1^+\rvert/\sqrt{\mathrm{SAR}}$	High safety excitation efficiency: The specific absorption rate (SAR) describes the amount of dissipated power per tissue mass and gives an estimate of tissue temperature rise during an MR scan. The International Electrotechnical Commission (IEC) defines SAR limits for safe human applications in IEC standard 60601-2-33.
$\min\limits_{\alpha_i} \lvert S_{i,j}\rvert \,\forall i \neq j$	Low inter-element coupling in phased arrays: Minimize the off-diagonal elements of the N-port scattering matrix S to simplify tuning and matching of individual array elements.
Receive Mode	
$\max\limits_{\alpha_i} \mathrm{SNR}$	High signal-to-noise ratio (SNR): In NMR the SNR is defined by the ratio of the signal- to the noise voltage $\mathrm{SNR} = V_{\mathrm{s}}/V_{\mathrm{n}}$.
$\min\limits_{\alpha_i} g$	Low geometry-factor (g-factor): The g-factor describes the ability of the array to separate aliased voxels when parallel imaging is applied. It is defined as $g = \mathrm{SNR}_{\mathrm{full}}/(\sqrt{\rho}\,\mathrm{SNR}_{\mathrm{red}})$, where ρ is the factor by which k-space is undersampled.

Table 1.1: Optimization goals

1.4 Electrodynamic Scaling of Human Brain MRS

Let us consider again the scattering problem of an RF antenna irradiating a homogeneous dielectric sample with wave number k (s. figure 1.1). Let the entire sample be enclosed in a sphere of radius R. Then the electrodynamic scaling of the model is determined by the product $k \cdot R$. If $k \cdot R \ll 1$ the electromagnetic field problem is of "low"-frequency type and Maxwell's equations can be simplified by neglecting the electric displacement term $\partial/\partial t\, \epsilon \mathbf{E}$ (10). Under this quasistatic approximation, the magnetic and electric fields are partially decoupled: The magnetic field excited by the RF coil is given by the Biot-Savart law (ignoring field diffusion in the dielectric sample). After the calculation of the magnetic field, the electric field can be obtained by applying Faraday's induction law. In the quasistatic regime, there is no detachment of electromagnetic waves from the RF coil. However, if the quasistatic condition $k \cdot R \ll 1$ is violated, the electromagnetic problem is said to be of "high"-frequency type and Maxwell's displacement current density cannot be neglected anymore. Now, the electric and magnetic field are coupled and there is wave propagation from the RF coil to the sample. The electrodynamic scaling for human brain MRS is illustrated in figure 1.2. Apparently, the quasistatic regime is valid for frequencies up to 10 MHz. The scope of this work is the optimization of RF coils at ultra-high field strength ($B_0 \geq 7$ T), which corresponds to Larmor frequencies above 300 MHz for proton MRS. Therefore, the quasistatic approximation is not applicable and a full-wave solution to Maxwell's equations is required.
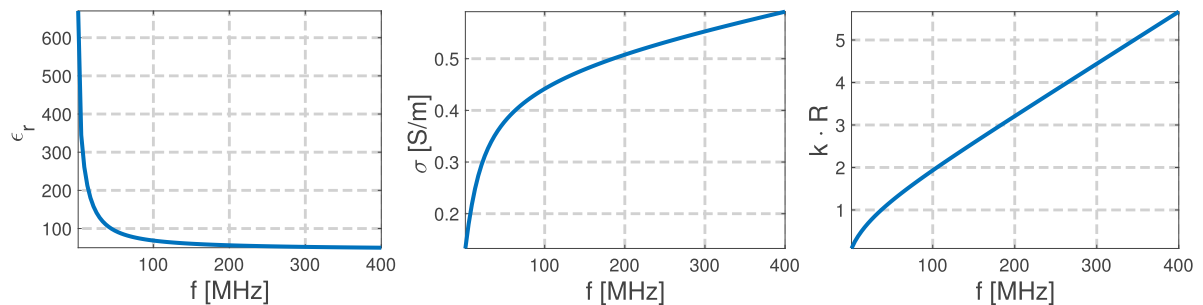
Figure 1.2: Relative permittivity (left) and electric conductivity (middle) averaged over gray and white matter in the human brain according to the Gabriel database (11). Right: electrodynamic scaling in the human brain (R=9 cm) measured as the product $k \cdot R$.

1.5 The Birdcage as an Optimal Low-Frequency Coil

A divergence-free surface current density $\mathbf{K}_{\text{bc}}$ is running on a cylinder of length $2c$ with sinusoidal φ-dependence. From (8), the surface current distribution is given by:

$$\mathbf{K}_{\text{bc}} = \nabla \times M_{\text{bc}} \mathrm{e}^{-\mathrm{i}\varphi} \left(\mathrm{H}(z+c) - \mathrm{H}(z-c) \right) \mathbf{e}_r. \qquad [1.15]$$

Here, M_{bc} is a magnetic dipole surface density, $\mathrm{H}(z)$ is the Heaviside step function and $\mathbf{e}_r$ is the unit vector in radial direction referring to a cylindrical coordinate system. This so-called birdcage current distribution is plotted in figure 1.3. It can be represented as a Fourier integral and Fourier series:

$$\mathbf{K}_{\text{bc}} = \int_{h=-\infty}^{\infty} dh \sum_{n=-\infty}^{\infty} w_{\text{bc}}^{\text{M}}(n,c,h) \nabla \times \mathrm{e}^{\mathrm{i}n\varphi} \mathrm{e}^{\mathrm{i}hz} \mathbf{e}_r. \qquad [1.16]$$

The Fourier expansion coefficients w_{bc}^{M} were already determined in (8):

$$w_{\text{bc}}^{\text{M}}(n,c,h) = \frac{M_{\text{bc}}}{\pi} \frac{\sin(hc)}{h} \delta_{n+1}. \qquad [1.17]$$

For an ideal birdcage resonator, the length $2c$ is much larger than the region of interest in the sample. In the limiting case of an infinitely long birdcage coil, the Fourier expansion coefficient w_{bc}^{M} becomes:

$$\lim_{c\to\infty} w_{\text{bc}}^{\text{M}} = M_{\text{bc}} \delta(h) \delta_{n+1}. \qquad [1.18]$$

When applying dyadic Green's functions (7), it is possible to calculate the transmit circularly polarized component (B_1^+) of an ideal birdcage coil inside a cylindrical phantom:

$$B_1^+(kr) \propto \mathrm{J}_0(kr). \qquad [1.19]$$
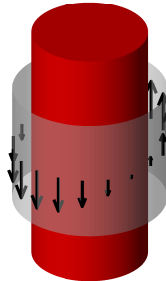
Figure 1.3: Surface current distribution of a birdcage coil surrounding a cylindrical sample.

Thereby, $k^2 = \omega^2 \epsilon \mu_0 + \mathrm{i} \omega \sigma \mu_0$ is the wave number in the dielectric cylinder of permittivity ϵ and electric conductivity σ. A time-harmonic behavior of $\mathrm{e}^{-\mathrm{i}\omega t}$ is assumed. The term J_0 refers to the Bessel function of first kind and zeroth order. Regarding the receive case, an ideal birdcage current distribution rotating in the opposite direction than in equation 1.15 (with $\mathrm{e}^{\mathrm{i}\varphi}$ dependence), results in a receive sensitivity $(B_1^-)^*$, that is also proportional to $\mathrm{J}_0(kr)$. A Taylor-series expansion of $\mathrm{J}_0(kr)$ at $kr = 0$ yields $1 - O(k^2 r^2)$. Therefore, if $|kr| \ll 1$, the Bessel function $\mathrm{J}_0(kr)$ is approximately constant.

Practically speaking, an infinitely-long birdcage current distribution $\mathbf{K}_{\mathrm{bc}}$ results in a homogeneous magnitude of B_1^+ and B_1^-, if the wavelength in the sample is much larger than the dimensions of the sample. To visualize the homogeneous operating regime of an infinitely long birdcage resonator, in figure 1.4 the circularly polarized components of the RF magnetic field in the sample are shown. For the simulation, average properties of gray and white matter were chosen according to the Gabriel database (11). The circularly polarized components of a birdcage resonator start to become inhomogeneous at 64 MHz (B_0=1.5 T for protons) for large head sizes. Clearly, at ultra-high field strength ($B_0 \geq 7$ T, $f \geq 300$ MHz for protons), the birdcage current patterns are not able to excite homogeneous B_1^+ and B_1^- components. However, at low field strength the birdcage current distribution is optimal with regard to flip angle and SNR homogeneity.
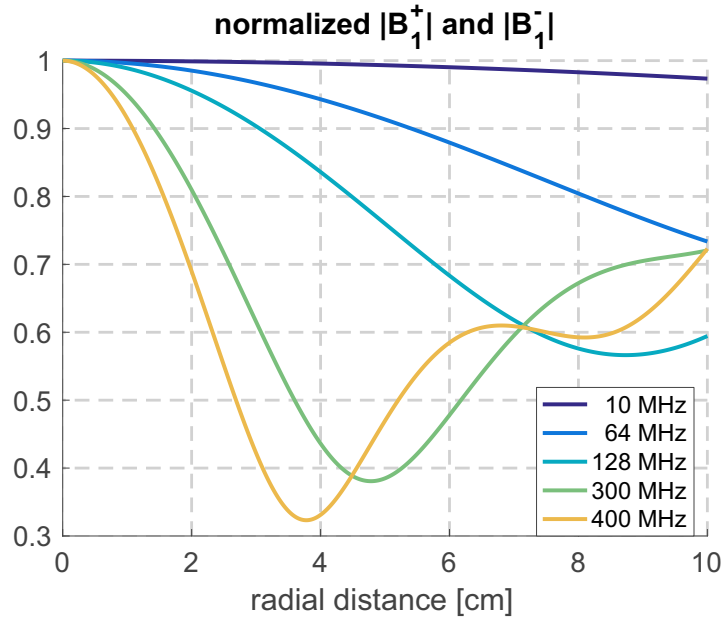
Figure 1.4: The normalized B_1^+ and B_1^- component of an infinitely long birdcage resonator in a cylindrical phantom.

1.6 Research Objectives

The goal of this thesis was to address some of the optimization problems (table 1.1) raised in "high"-frequency RF coil design for human brain MRS. The corresponding optimization problem was solved with the help of equivalent surface currents. Based on the simulation results, field strength specific design guidelines for RF coil design were deduced. The following optimization problems were treated:

The first project (PUBLICATION 1) focused on the optimization problem of maximizing the SNR in a spherical phantom of human head size. It was shown, that the basis set of equivalent surface current patterns yielding the UISNR limit, can be separated into curl- and divergence-free components. The purpose of this study was to systematically investigate the different contributions of curl- and divergence-free current patterns to the UISNR. The different contributions are of high practical relevance, because traditional loop-only receivers are just able to capture the divergence-free SNR limit and miss the contribution of curl-free current patterns.

The second project (PUBLICATION 2) continued the work of the first project by doing a systematic analysis of the best possible SNR of loop- and dipole-like current patterns in relation to the ultimate SNR in a realistic human head model. The objective was to find out, how close loop- and dipole-only receive arrays are able to approach the UISNR threshold, or rather the SNR gain of combining both elements. Moreover, the study examined the influence of the array holder geometry on the SNR efficiency of loop and dipole elements.

The objective of the third project (PUBLICATION 2, PUBLICATION 3) was to quantify the increase of the UISNR in the human head with field strength B_0. For that, a power series model was fitted to the UISNR results of a head-sized sphere and a realistic head model. The spatial distribution of the exponent was plotted to identify regions in the human head with super- and sublinear increase of the UISNR.

The fourth project (PUBLICATION 4) dealt with the optimization problem of minimizing inter-element coupling in phased arrays. The aim of the work was to understand and eliminate the complex mutual coupling between rectangular surface loops surrounding a cylindrical head-sized sample. The hope was to fully compensate the complex mutual impedance by overlapping the loop elements and optimizing their widths. Based on a newly developed analytic model, the optimization problem could be solved and a fully decoupled prototype array was constructed at 400 MHz. No additional decoupling circuitry was needed.

2 Thesis Composition

This PhD thesis is written as integrated accumulation of publications. In this chapter, PUBLICATION 1, PUBLICATION 2, PUBLICATION 3 and PUBLICATION 4 are summarized. The full articles are appended in chapter 4.

2.1 The Ultimate SNR of Curl- and Divergence-Free Currents in a Spherical Head Model

This section summarizes PUBLICATION 1.

Introduction

In NMR, the SNR serves as an important figure of merit to assess the receive performance of an RF coil. It is defined as the ratio between the received signal voltage and the accumulated noise voltage originating from sample and coil losses. Thereby the achievable SNR of any real receive array is inherently limited by Maxwell's equations. This ultimate intrinsic SNR (UISNR) threshold neglects all coil losses and the only source of noise is the RF power dissipated in the sample. It was first studied by Roemer (12) and Wang (13), however, under the quasistatic assumption. Later, Ocali calculated the UISNR in a cylindrical phantom with a full-wave ansatz (14). To find the UISNR, this author formulated a constrained optimization problem: First, a basis set of electromagnetic fields solving the homogeneous Helmholtz equation in the sample is required. Then, expansion coefficients that minimize the noise voltage under the constraint of a constant signal voltage need to be found. Ohliger (15) and Wiesinger (16) extended the UISNR theory to parallel imaging. Based on the weak SENSE reconstruction (17), these authors constrained the net receive sensitivity. All of the previously mentioned studies result in an optimal electromagnetic field distribution in the sample. This is very interesting from a theoretical viewpoint, but for the practical design of RF coils it is more favorable to optimize a current distribution. In section 1.2 it was shown, that it

is possible to define a basis set of equivalent surface currents that are able to excite all possible electromagnetic fields within the sample. Schnell (8) and Lattanzi (9) used such a surface current basis set to find the ideal current distribution yielding the UISNR.

In this study, the human head was approximated by a simple dielectric sphere. For a spherical sample, the basis set of equivalent surface currents is given by (9):

$$\mathbf{K} = \sum_{l=1}^{\infty} \sum_{m=-l}^{l} \alpha_{l,m}^{\mathrm{M}} \mathbf{X}_{l,m}(\vartheta, \varphi) + \alpha_{l,m}^{\mathrm{E}}(\hat{\mathbf{r}} \times \mathbf{X}_{l,m}(\vartheta, \varphi)). \qquad [2.1]$$

The term $\mathbf{X}_{l,m}$ is the vector spherical harmonic defined in equation [9.119] in (10) and $\hat{\mathbf{r}}$ is the unit vector in radial direction. Equation 2.1 is composed of a divergence-free component, $\mathbf{X}_{l,m}$, and a curl-free component, $\hat{\mathbf{r}} \times \mathbf{X}_{l,m}$. The divergence-free component of the current (magnetic-type) has expansion coefficients $\alpha_{l,m}^{\mathrm{M}}$ and the curl-free component (electric-type) has expansion coefficients $\alpha_{l,m}^{\mathrm{E}}$. In order to calculate the UISNR ζ, both curl- and divergence-free current patterns must be used. When allowing only divergence-free current patterns in the optimization process, the achievable UISNR is denoted as ζ^{M}. This value corresponds to the best possible SNR when receiving with loop-only elements, as a uniform current in a loop is divergence-free. The definition of ζ^{E} having only curl-free current patterns follows accordingly. The contribution of divergence-free current patterns to the UISNR is defined as the ratio ζ^{M}/ζ, and the contribution of curl-free current patterns to the UISNR as the ratio ζ^{E}/ζ.

Study Design

The aim of this study was to systematically investigate the contribution of curl- and divergence-free current patterns to the UISNR in a spherical model the size of the human head (9.2 cm radius). This quantitative analysis was done for magnetic fields B_0 of 1.5 T, 3 T, 7 T, 9.4 T and 11.7 T. The corresponding Larmor frequencies for protons (^{1}H was implicitly assumed as the NMR visible isotope throughout this study) fell in the frequency range between 64 MHz and 498 MHz. The frequency dependent permittivity and electric conductivity of the dielectric sphere were chosen to match average tissue properties of gray and white matter according to the Gabriel model (11). The influence of parallel imaging on the ratios ζ^{M}/ζ and ζ^{E}/ζ was studied at 9.4 T.

26

Results

First, it was demonstrated that ideal current patterns yielding the UISNR depend on voxel position and acceleration factor (figure 8 of PUBLICATION 1). It has to be emphasized that only a snapshot is shown, and that the current patterns evolve in time with a $e^{-i\omega t}$ dependence. All these facts make it very challenging to practically implement ideal current patterns. However, it was possible to deduce some very fundamental information from the ideal current patterns, such as the contribution of curl- and divergence-free current components to the UISNR. Those contributions are illustrated in figure 2.1. At 1.5 T and 3 T, divergence-free current patterns are sufficient to achieve more than 96% of the UISNR in all parts of the sphere. Moreover, regarding the peripheral and central regions, divergence-free components saturate the UISNR in the whole frequency range. When increasing the main magnetic field B_0, there is an intermediate region between the center and the periphery, where the divergence-free UISNR is substantially lower than the total UISNR. The minimum ζ^{M}/ζ is about 59% at 11.7 T. On the other hand, with increasing B_0, the curl-free contribution reaches its maximum in this intermediate region. As a consequence, the combination of curl- and divergence-free current patterns boosts the SNR in the intermediate region by 36% (7 T), 57% (9.4 T) and 68% (11.7 T) compared to the SNR of divergence-free current patterns only. In the next step, the influence of parallel imaging was examined. Figure 2 of PUBLICATION 1 visualizes the contributions for different acceleration factors at 9.4 T. Up to an acceleration of 3x3, the
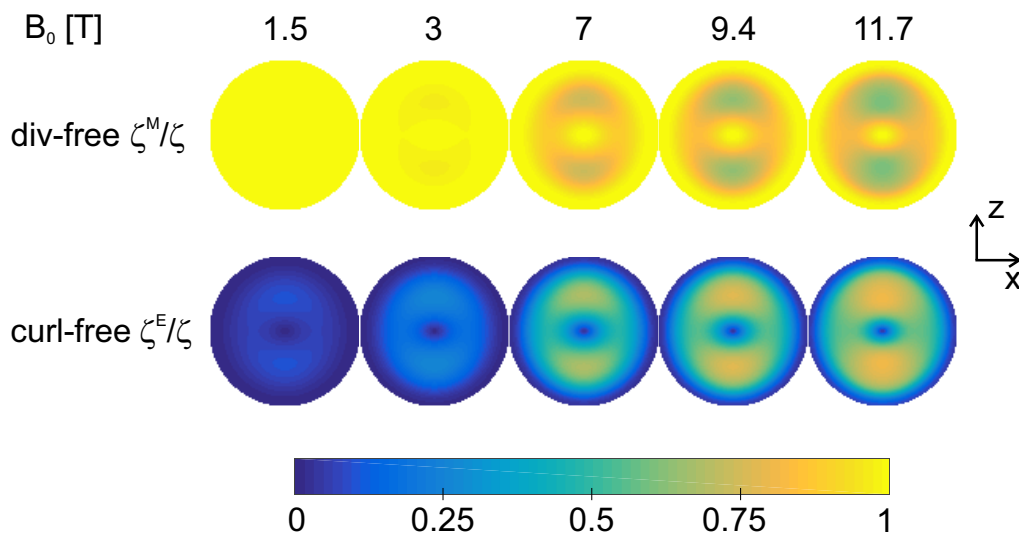
Figure 2.1: The contribution of curl- and divergence-free current patterns to the UISNR in a sphere of human head size. The static magnetic field B_0 is pointing in z-direction. The contributions are rotationally symmetric about the z-axis.

contributions of ζ^{M}/ζ and ζ^{E}/ζ are almost independent of the acceleration factor. For higher acceleration, the contribution of curl-free current patterns decreases. The spatial distribution of ζ^{M}/ζ becomes more homogeneous if $\rho >$5x5. Figure 5 of PUBLICATION 1 shows the dependence of the contributions with regard to the size of the sphere. Focusing on the central voxel, it is interesting that for $B_0 \geq 3$ T and acceleration factors $\geq$ 4x4, the UISNR is not fully recovered by divergence-free current patterns. For the intermediate voxel position, the following trend was observed: The larger the sphere, the more SNR is lost when using only divergence-free components. This is true, if the radius is smaller than approximately 9 cm.

Discussion

According to the results of the last paragraph, practical recommendations for RF coil design for head applications were made. For $B_0 \leq 3$ T, it is sufficient to use loop-only receive arrays, which have a direct correspondence to divergence-free current patterns. However, at ultra-high field strength ($B_0 \geq 7$ T), a combination of curl- and divergence-free current patterns is suggested. Only the combination of these complementary current patterns results in the maximal SNR over the whole sphere. In practice, a combination of curl- and divergence-free current patterns can be realized by using loop and dipole elements together in the array. Regarding body applications, there was an interesting publication investigating the receive performance of finite element loop and dipole arrays in a cylindrical phantom of human body size (18). Due to the fact, that straight, z-directed dipoles consist of both curl- and divergence-free current components (19), an array of 16 dipoles recovered almost 80% of the UISNR in central and intermediate body regions at 7 T and 9.4 T (18). Nevertheless, electric-dipoles alone do not create a complete basis set of equivalent surface currents, as for example peripheral UISNR can only be saturated by loop elements. In a very systematic study (20), the authors elaborated on the SNR performance of finite element loop arrays in a spherical phantom of human head size. In contrast to a cylindrical head model, in the spherical head model central SNR is fully reached by loop elements even at 9.4 T.

In general, it has to be stated that at the time of this thesis, the research with regard to the practical implementation of dipole-only (21–25) or loop-dipole (26–28) head arrays at ultra-high field strength was still at its beginning. The most challenging parts were the shortening of $\lambda/2$ dipoles (29–33) and the decoupling between dipole elements (34). Instead of using dipoles, there are other possibilities in order to realize curl-free current patterns. One option would be to use vertical loop elements (35–

37), which are positioned perpendicular to conventional surface loops. A simultaneous excitation of curl- and divergence-free current patterns can also be realized, by unequally distributing capacitors on loop elements (38).

Conclusion

In this work, for the first time the contribution of curl- and divergence-free current patterns to the UISNR was systematically investigated for different field strengths. Based on these findings, practical guidelines for RF coil design in human head applications were formulated. Moreover, field strength specific recommendations regarding the combination of loop and dipole elements were suggested.

2.2 The Ultimate SNR of Loop- and Dipole-Like Currents in a Realistic Head Model

This section summarizes PUBLICATION 2.

Introduction

At the time of this thesis, there was great interest in using electric dipoles to enhance the SNR of traditional loop-only arrays for human head applications at 7 T and above. Initial studies were done with dipole-only arrays (22–25) or with a combination of loop and dipole elements (26–28). As an alternative to the electric dipole, vertical loop elements were combined with surface loops (39). From a theoretical viewpoint, loop-only receive arrays can be represented by a divergence-free surface current distribution. In order to form a complete electromagnetic basis set, divergence-free current patterns need to be accompanied by curl-free current patterns (40). Furthermore, straight dipoles mounted on a cylindrical holder are represented by Z-directed current patterns. To form a complete basis set, the Z-directed current patterns must be complemented by Φ-directed current patterns. Evaluating the best possible SNR of divergence-free (loop-like) or Z-directed (dipole-like) current patterns relative to the ultimate SNR yields a direct performance measure of how close general loop-only or dipole-only receive arrays are able to achieve the ultimate threshold.

In section 2.1, the best possible SNR of curl- and divergence-free current patterns relative to the UISNR in a spherical phantom of human head size was systematically analyzed. The generic surface current patterns covered the complete spherical surface around the sample. This simple model was useful to understand the basic SNR limitations of loop-only arrays as well as how to overcome them by combining loop and dipole elements in the array. Of course, the human head is not a uniform sphere, and in practice the surface current distribution cannot be entirely closed due to the human neck. For this reason, the aim of the second publication was to perform more realistic simulations: First, the Huygens' surface of equivalent surface currents had an opening for the neck. Following two typical practical designs, a spherical cap (helmet-like structure) and a cylindrical surface were chosen. Second, the spherical model was replaced by a realistic human head model ("Duke") from the virtual family (41).

When this thesis was written, there were very few studies about the UISNR in realistic human body models. The first one was done by Felder, who used a plane wave

expansion to study the UISNR in a human head model at 9.4 T (42). By randomly exciting a large number of elementary electric and magnetic dipoles on a head conformal surface, Guérin, was able to evaluate the UISNR in a head model (43). However, neither of the two mentioned methods is able to separate curl- and divergence-free current patterns, which is essential for estimating the performance of loop and dipole elements. Therefore, in this work a new method was developed to access the best possible SNR of curl- and divergence-free current patterns.

The workflow for calculating the UISNR ζ and the best possible SNR of curl- and divergence-free current patterns (ζ^E, ζ^M), as well as the best possible SNR of Z- and Φ-directed current patterns (ζ^Z, ζ^Φ), is outlined in figure 2.2. The curl- and divergence-free surface current modes $\mathbf{K}^E$ and $\mathbf{K}^M$ excite eigenfunctions of the Helmholtz equation in spherical or cylindrical coordinate systems. Regarding the cylindrical Huygens' surface, there is a linear transform to obtain Φ- and Z-directed current patterns from $\mathbf{K}^M$ and $\mathbf{K}^E$ (19). Using DGF (7), it is possible to calculate the free-space fields $\mathbf{E}_{\mathrm{inc}}$ and $\mathbf{B}_{\mathrm{inc}}$ from the current modes. As a response to the incident fields, polarization currents are excited in the dielectric head. These polarization currents radiate and result in a scattered field (44). The polarization currents and the resulting total fields in the head model were calculated with a fast volume integral equation solver. This Matlab-based
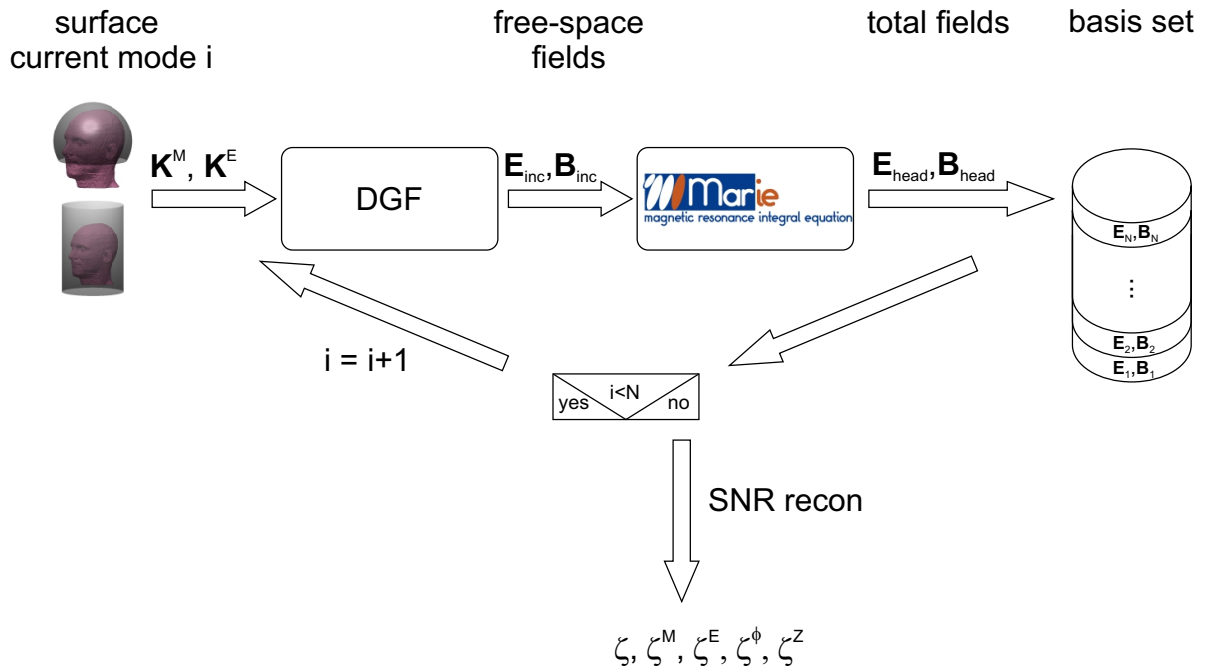
Figure 2.2: Workflow for calculating the UISNR and the best possible SNR of curl- and divergence-free and Z- and Φ- directed current patterns.

solver called "MARIE" is open-source and was developed by a group at Massachusetts Institute of Technology (45–47). In a last step the total fields were stored in a database and the next basis vector was calculated. When the basis set had a sufficiently large number of basis vectors, the UISNR could be reconstructed.

Study Design

The UISNR was calculated at all practically relevant field strengths for human applications between 1.5 T and 11.7 T. The corresponding Larmor frequencies for protons (^{1}H was implicitly assumed as the NMR visible isotope throughout this study) were in between 64 MHz and 498 MHz. The voxel-based model "Duke" consisted of 77 different tissue types and had an isotropic resolution of 2 mm. The frequency dependent electromagnetic properties of each tissue were modeled according to the Gabriel database (11). The spherical cap had a radius of 13 cm and a cap angle of 120°. The cylindrical surface had a radius of 13 cm and a length of 30 cm. All simulations were done on a dedicated high-computing server equipped with two Nvidia P100 GPUs to massively accelerate the FFT-based integral equation solver. The basis set for the spherical cap Huygens' surface consisted of 2550 basis vectors and the cylindrical surface had 3038 basis vectors.

Results

In figure 2.3, the required simulation times to calculate the basis set for the spherical cap Huygens' surface are visualized. Parallel programming and GPU based computing
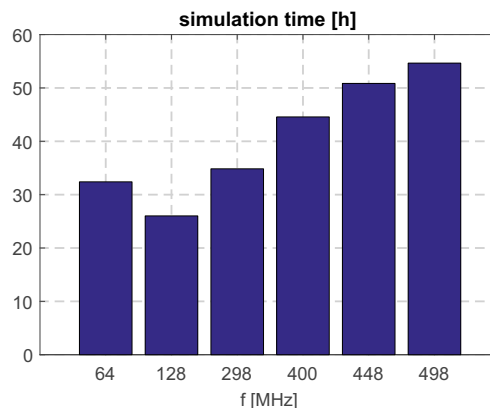
Figure 2.3: Simulation time for calculating the basis set (2550 basis vectors) for the spherical cap Huygens' surface.

was essential to decrease the simulation times to such reasonable values. Figure 6 of PUBLICATION 2 illustrates the best possible SNR of curl- and divergence-free current patterns relative to the UISNR with respect to the spherical cap basis set. At 1.5 T and 3 T, divergence-free current patterns achieve more than 90% of the UISNR in the whole human head. Moreover, divergence-free current patterns saturate the UISNR in the peripheral and central head regions for all field strengths. However, at ultra-high fields ($B_0 \geq 7$ T), there are regions in the human head, where loop-like current patterns are not able to reach the UISNR threshold. In those regions, adding curl-free current patterns to the divergence-free basis set substantially improves the SNR by 24% (7 T), 45% (9.4 T) and 49% (11.7 T). Moving on to the cylindrical basis set, figure 7 in PUBLICATION 2 visualizes the best possible SNR of curl- and divergence-free current patterns relative to the UISNR. Similar to the spherical cap basis set, when increasing B_0, the minimum of ζ^{M}/ζ decreases, but the maximum of ζ^{E}/ζ increases. In central head regions, the combination of curl- and divergence-free current patterns boosts the SNR by 21% (7 T), 33% (9.4 T) and 39% (11.7 T) in comparison to divergence-free patterns only. Next, we studied the best possible SNR of Φ- and Z-directed current patterns relative to the UISNR (figure 8 of PUBLICATION 2). Z-directed currents have high SNR in central head regions, but are not very efficient in the periphery. With increasing field strength, their SNR efficiency increases. At 7 T and above, dipole-like current patterns result in 93% of the ultimate SNR in the brain center. Finally, we compared the SNR performance of divergence-free with Z-directed current patterns in figure 9 of PUBLICATION 2. At 1.5 T and 3 T, loop-like currents achieve higher SNR than dipole-like currents in the whole brain. At 7 T, loop-like currents still outperform dipole-like currents in most regions of the human head (except for a small region close to sphenoidal sinus). However, at 9.4 T and above, dipole-like current patterns have superior SNR performance over loop-like currents in central head regions: There, the SNR of Z-directed currents is 24% (9.4 T) and 26% (10.5 T, 11.7 T) higher compared to divergence-free currents.

Discussion

The results presented in the previous paragraph motivate the following design recommendations for RF receive arrays in human head applications: On 1.5T and 3T platforms, loop-only arrays cover more than 90% of the UISNR in the whole human head (both helmet-like and cylindrical surface). In contrast to this, at 7 T and above, there are regions in the human head, where the SNR of loop-only receivers can be substantially increased by adding complementary current patterns.

With regard to the cylindrical coil holder, loop elements can be accompanied by electric dipoles pointing in z-direction. Previously, there have been a few attempts to combine loops and dipoles at ultra-high field strength (26–28). Moreover, the SNR of loop-only arrays can be enhanced by adding vertical loop elements (35–37). As an example, by adding eight vertical loops to an existing eight channel surface loop array (400 MHz), Avdievich measured an SNR increase of almost 30% in the brain center (39). This SNR boost cannot only be attributed to the increased number of receivers, because 16 loop elements result in an SNR increase of about 4% in the center of a head-sized sphere (20). Based on figure 9 of PUBLICATION 2, the usage of dipole-only arrays is not recommended for human head applications lower than 9.4 T. For $B_0 \geq 9.4$ T, dipole-only arrays can achieve higher SNR than loop-only arrays in central head regions. To complement loop elements on a helmet-like design, Θ-directed dipole elements or vertical loop elements could be potential candidates.

As already stated in section 1.2, the equivalent surface current distribution needs to span a closed surface around the sample to form a complete basis set. However, such a closed current distribution is unrealistic for human head applications, because there is no opening for the neck. For this reason, a spherical cap surface current distribution was introduced in this study. Although this basis set is not complete, in figure 4 of PUBLICATION 2 it is shown that for a spherical setup ($\vartheta_0 = 120°$), the UISNR is only underestimated close to the southern pole. Equivalently, for the realistic head model, one can hypothesize that the UISNR could be underestimated in the brainstem and spinal cord. Despite the incompleteness of the spherical cap basis set, the presented UISNR results are optimal with regard to any helmet-like array design. Also, a closed surface can be realized by an infinitely long cylindrical surface current distribution. However, such a current distribution is unrealistic and numerically unstable. The numerical instability arises from the strong correlation of electromagnetic fields of higher order basis vectors. Therefore, a cylinder of finite length having approximately the same coverage in z-direction as the human head voxel model was used for this study.

Comparison of the UISNR results between the spherical model (figure 2.1) and the realistic head model (figure 6 in PUBLICATION 2) reveals that the performance of loop-only arrays is higher in the realistic head model than in the spherical model. One reason for this observation could be the fact that a spherical cap Huygens' surface was used for Duke, whereas a closed spherical surface was used for the spherical model. Formally, this corresponds to a cap angle of $\vartheta_0 = 180°$. In figure 5 of PUBLICATION 2 it is shown that with decreasing cap angle, the minima of ζ^{M}/ζ increase. Despite the different geometry

and inhomogeneity of the "Duke" model, the results obtained from the simple spherical setup qualitatively match the results from a realistic body model.

Conclusion

For the first time, the best possible SNR of loop- and dipole-like current patterns relative to the UISNR was studied in a realistic human head model. This was possible because of a fast and efficient volume integral equation solver running on a dedicated high-computing GPU-based server. The SNR performance of loop and dipole elements for head applications was predicted to guide future RF coil designs at ultra-high frequency.

2.3 The Increase of the Ultimate SNR in the Human Head with B_0

This section summarizes PUBLICATION 2 and PUBLICATION 3.

Introduction

The motivation to build new MR platforms operating at higher static magnetic field strengths B_0 is the increase of the SNR. It is well known, that in the quasistatic regime, the SNR increases linearly with B_0 (48, 49). However, with increasing field strength, the Larmor frequency increases as well and the quasistatic condition is violated. For human head applications, a full-wave solution to Maxwell's equations is required if the Larmor frequency is larger than approximately 10 MHz (s. figure 1.2). Therefore, this study was designed to investigate the increase of the UISNR with regard to B_0 considering the full-wave electromagnetic problem. There were already several publications about the increase of the UISNR at the time of this thesis: the UISNR increase in simple cylindrical or spherical models was investigated in (8, 9, 14, 16); additionally, Guérin published UISNR results in a realistic human head model (43); Pohmann and colleagues measured the SNR increase from 3 T to 7 T and from 7 T to 9.4 T with state-of-the-art receive-only arrays (50). None of the previously mentioned studies did quantitative fitting of the full spatial UISNR to a power series model. The goal of this study was to deduce quantitative maps showing the regions in the human brain where the UISNR increases superlinearly with B_0.

Study Design

The increase of the UISNR was investigated with two different models. First, the UISNR was evaluated in a sphere of human head size. The simulation setup and sample properties were the same as in section 2.1. Moreover, the UISNR was computed in a realistic human head model using a spherical cap basis set (same setup as in section 2.2). Both, for the sphere and the realistic voxel model, the UISNR was simulated at several field strengths B_0 (1.5 T, 3 T, 7 T, 9.4 T, 10.5 T, 11.7 T). Assuming ^{1}H as the NMR visible isotope, the Larmor frequencies were between 64 MHz and 498 MHz. After finishing these simulations, the UISNR at each voxel position $\mathbf{r}$ was fitted to a power series model of the form:

$$\zeta(B_0, \mathbf{r}) = c(\mathbf{r}) B_0^{n(\mathbf{r})}. \tag{2.2}$$

Results

In figure 2.4, the fitted exponent n is plotted for the spherical head model and the realistic voxel model "Duke". Both models show a sublinear increase of the UISNR in
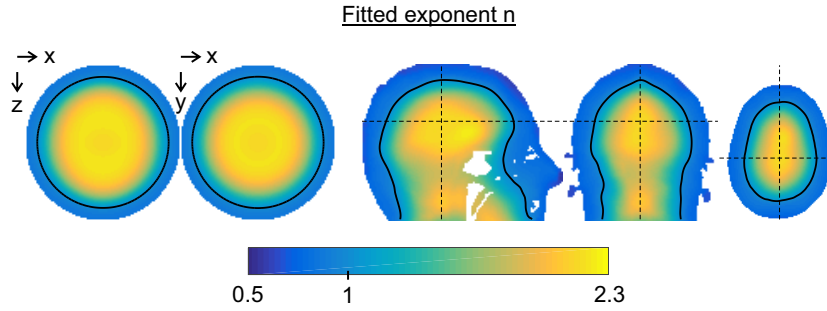

Figure 2.4: The increase of the UISNR as a function $\zeta = cB_0^n$. The fitted exponent n is shown. The black contour lines indicate the linear threshold.

the periphery. In the realistic body model, the linear threshold (black contour line) is about 16 to 20 mm away from the skin. The UISNR grows superlinearly in the central regions of the models. In the inner brain, the UISNR grows with an approximate exponent of $n \approx 1.5$. When increasing B_0 from 3 T to 7 T, the relative UISNR gain in central head regions is about a factor of four (s. figure 2.5). From 7 T to 9.4 T,
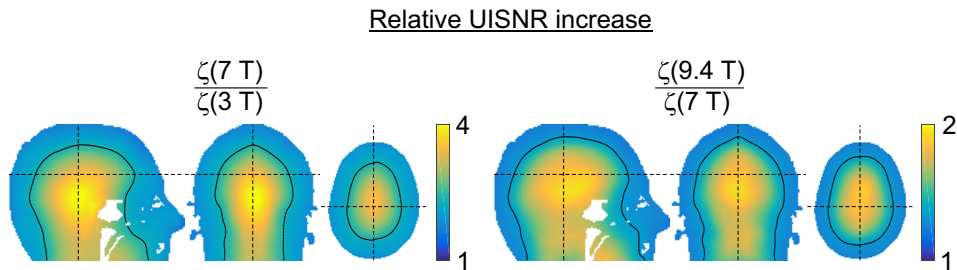
Figure 2.5: The relative gain in UISNR when increasing B_0 from 3 T to 7 T (left) and from 7 T to 9.4 T (right). The black contour lines indicate the linear threshold.

there is gain of almost two in this region. Figure 2.6 compares the experimentally measured SNR increase from 3 T to 7 T and from 7 T to 9.4 T with the corresponding increase of the UISNR. In general, the measured SNR increase seems higher than what is predicted from UISNR simulations. For example, the measured SNR boost from 3 T to 7 T in the cerebellum and in parts of the frontal lobe is larger than a factor of four, whereas the simulations only predict a factor of about three (cerebellum) and two (frontal lobe). Another difference between simulation and experiments is that the

UISNR grows monotonically with B_0, whereas the measurements reveal regions in the very periphery of the brain where the SNR even decreases.

Discussion

The first (full-wave) study about the increase of the UISNR with regard to B_0 was done by Ocali (14). He reported a superlinear increase of the UISNR in the center of a human torso model. Later, Schnell confirmed this result in a cylindrical body model (8). In (16), Wiesinger used a multipole expansion in a spherical model (15 cm radius) and published an exponent of 1.92, 2.05 and 0.9 at a central, intermediate and peripheral voxel position, respectively. Also Lattanzi showed a superlinear increase of the UISNR in the center of a head-sized sphere and a sublinear increase in the periphery (9). In a recent publication (43), Guérin studied inter alia the increase of the UISNR in a realistic human head model. His results are in accordance to this study; he found a sublinear
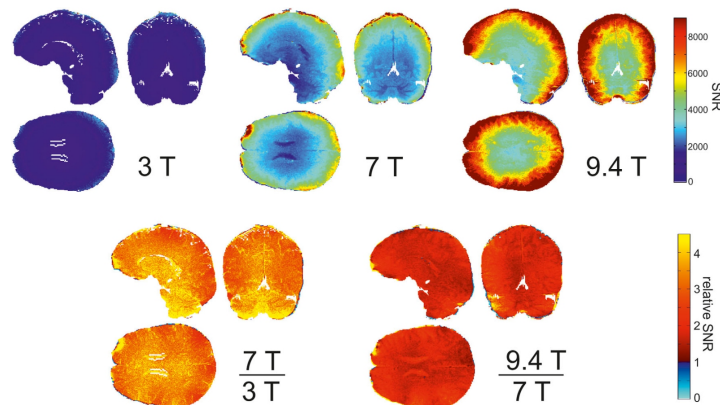
Figure 2.6: a) Experimentally measured increase of the SNR. This figure is copied from reference (50) with the permission of John Wiley & Sons, Inc. b) Simulated increase of the UISNR in voxel model Duke. The color scale is the same as in subfigure a).

increase for a voxel close to the head's surface and a superlinear increase in central brain regions.

The discrepancy between the predicted increase of the UISNR from this study and the measured increase of the SNR by Pohmann et al. can be attributed to different receive sensitivity profiles of the arrays. As the influence of the receive sensitivity was not calibrated out, the measured SNR values depend on the particular coil design. By contrast, the UISNR is a coil independent performance measure. It needs to be conceded, however, that especially at ultra-high field it is very difficult to map the receive sensitivity due to the lack of a homogeneous transmit field. Both, experimental and simulated results reveal, that the SNR increases superlinearly in the cerebrum.

Conclusion

For the first time, the UISNR in a realistic human head model was fitted to a power series model with full spatial coverage. It was shown, that the UISNR increases superlinearly for central head regions within the range $1.5\ \text{T} \leq B_0 \leq 11.7\ \text{T}$. This work confirmed previous theoretical and experimental studies about a superlinear increase of the SNR.

2.4 Understanding and Eliminating Complex Mutual Coupling of Surface Loops

This section summarizes PUBLICATION 4.

Introduction

On ultra-high field MR systems ($B_0 \geq 7$ T), the wavelength of the RF magnetic field in the human brain is smaller than the head size (s. figure 1.2). As a result, single-channel quadrature volume coils, which are based on the idea of birdcage-like current patterns, suffer from flip angle inhomogeneity (51,52). Transceiver (52–56) and transmit (57) phased arrays provide more degrees of freedom to mitigate the B_1^+-inhomogeneity by means of RF shimming (58–61) or parallel transmission (62–64). Thereby, the performance of these techniques is enhanced when the number of transmit channels is increased (60, 65). However, this comes at the cost of higher cross-talk between the array elements. In principle, the cross-talk of any N-port network can be eliminated by using a decoupling network of $2N$ ports having $4N^2$ circuit elements (66). In practice, decoupling is most of the time limited to adjacent array elements as the complexity grows quadratically.

The coupling between two loop elements can be described by a complex mutual impedance $Z_{12} = R_{12} + i\omega L_{12}$. The electric k_e and magnetic k_m coupling coefficients are defined as

$$k_e = \frac{R_{12}}{R} \qquad\qquad [2.3]$$

$$k_m = \frac{L_{12}}{L}, \qquad\qquad [2.4]$$

where R is the total loop resistance, L the loop inductance, R_{12} the mutual resistance and L_{12} the mutual inductance. The quality factor of the loops is given by $Q = \omega L/R$. Then, the scattering parameter S_{12} can be evaluated as

$$S_{12} = \frac{1}{2}\left(k_e + i k_m Q\right) \qquad (|Z_{12}| \ll R). \qquad\qquad [2.5]$$

Instead of using an additional decoupling network, the distance between the centers of the loops can be optimized to eliminate either k_e or k_m (67–69). However, without further optimization there remains a residual S_{12}, due to the presence of the non-suppressed

coupling mechanism. Typically, the two loops are overlapped until k_{m} becomes zero. At 1.5 T for example, the remaining value of k_{e} is about 0.55 (s. figure 3 in PUBLICATION 4) resulting in a residual S_{12} of -11.2 dB.

This study was motivated by the question, if it was possible to simultaneously compensate k_{e} and k_{m} by varying the loop separation and the loop width. Therefore, the complex mutual impedance of two rectangular window loops surrounding a cylindrical phantom (s. figure 2.7) was systematically investigated. Moreover, the dependence of Z_{12} on loop width, loop separation, resonance frequency and sample size was intensively studied. As numerical full-wave electromagnetic methods (e.g. FDTD, FEM) were very time-consuming to explore with all of these aspects, a fast full-wave analytic model based on dyadic Green's functions was developed. When PUBLICATION 4 was written, there were analytic models regarding the SNR calculation of surface loops loaded by a cylinder (18, 70, 71). However, none of these publications described the impedance matrix Z_{12}. Wright described an analytic model to evaluate the Z-matrix in a different setup of two planar surface coils above an infinite half-plane (68).

Study Design

As a first step, the analytic model had to be validated by numerical FEM simulations (CST Microwave Studio) and bench measurements using a network analyzer. Therefore, two rectangular window loops (100x80 mm^2) were mounted on a cylindrical FR4 holder (diameter of 215 mm). The angular separation α between the centers of the loops was varied in the range $0° \leq \alpha \leq 180°$. The array was loaded by a cylindrical phantom (diameter of 170 mm) having tissue equivalent electromagnetic properties at 400 MHz. The complex impedance Z_{12} was simulated and measured at 64 MHz, 124 MHz, 300 MHz and 400 MHz. After validation of the analytic model, it could be demonstrated
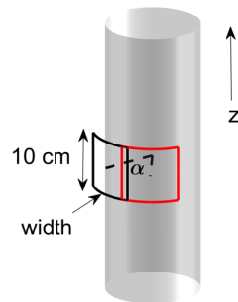

Figure 2.7: Setup to study the mutual impedance between two rectangular window loops.

that by overlapping the loops and optimizing their widths, at 400 MHz both the mutual inductance and the mutual resistance can be eliminated simultaneously. A two-channel prototype transceiver array was built and the SNR and transmit efficiency of the optimized overlapped array was compared to a two-channel gapped array used in other designs (52, 72).

Results

Using the commercial FEM solver of CST, the calculation of the impedance matrix for 16 different angular separations at 400 MHz required about 24 h on a dedicated workstation. In contrast to that, evaluating the analytic model on a standard desktop computer with a much higher angular resolution (100 samples) took only 3 min.

Figure 3 in PUBLICATION 4 visualizes the coupling curves obtained from the analytic model, the FEM simulations and bench measurements. At 64 MHz, the developed model is in very good agreement with the measured and simulated resistive coupling constant k_e. This is also the case for k_m, if $\alpha \geq 40°$. The more the loops overlap, the more the predicted k_m value of model deviates from the experiment and FEM simulation. This phenomenon is also apparent at higher frequencies. At 300 MHz and 400 MHz, there is a large discrepancy between the modeled k_e curve and the numerical simulations and measurements, if $|k_\mathrm{m}| \geq 0.02$. However, for the important practical case of canceled mutual inductance (transformer decoupling), the analytic k_e curve follows the CST simulations and measured data very well in the range $35° \leq \alpha \leq 180°$ (s. figure 4a in PUBLICATION 4).

After validation, the analytic model was used to investigate the dependence of k_e and k_m on frequency, sample size, loop- width and separation. The results are shown in figure 5 of PUBLICATION 4. The magnetic coupling constant k_m experiences a zero-crossing at the critical overlap angle $\alpha = \alpha_\mathrm{cm}$. This angle becomes smaller when the loop width decreases. The k_m curve is almost frequency and load independent, as changing the radius of the sample practically does not affect the curve. The electric coupling coefficient k_e has at least one zero crossing, where the crossing with the lowest angle is denoted $\alpha = \alpha_\mathrm{ce}$. In general k_e depends strongly on frequency and loading: The higher the frequency and the larger the sample, the closer the critical angle α_ce approaches α_cm.

These circumstances motivated a systematic analysis at 400 MHz, where the loop width was gradually increased from 8 to 12 cm (s. figure 2.8). The white and red lines indicate the contours, where $k_\mathrm{e} = 0$ and $k_\mathrm{m} = 0$. The intersection of the two curves is at an angle $\alpha = \alpha_\mathrm{ce} = \alpha_\mathrm{cm}$ of about 50° for a loop width of approximately 10.5 cm. Using

this optimized geometry, the two loop array is fully decoupled for a sample radius of 8.5 cm. To check the robustness of the geometric decoupling method on load variation, figure 2.9 shows the S_{12} value as a function of the sample radius: If the radius varies less than $\pm$ 24 %, decoupling is always better than -14 dB.

Based on these optimization results, an overlapped (loop dimensions 100 x 105 mm^2, $\alpha = 46°$) two-channel transceiver array was built and evaluated against a gapped, transformer decoupled (loop dimensions 100 x 80 mm^2, $\alpha = 49°$) array. Loaded with the cylindrical phantom of 8.5 cm radius, the measured S_{12} were -26 dB and -42 dB for the gapped and overlapped array, respectively. Photographs and performance results of the constructed arrays are presented in figure 8 of PUBLICATION 4. The overlapped array had improved transmit and receive performance compared to the gapped version: The penetration depth was increased and the signal voids were eliminated (s. white arrows).

Discussion

The large discrepancy between the analytic k_e curve and numerical and experimental evaluation for strongly coupled loops ($|k_m| \geq 0.02$) at ultra-high frequency is due to the model assumption that the currents in each loop are independent of each other. However, in the presence of strong mutual inductive coupling, the two current distributions become correlated. As a result, there is a correlation between the electrical fields excited by both loops in the sample. According to Faraday's induction law, this correlation is frequency dependent. For lower frequencies (e.g. 64 MHz), the correlation is low and the model predicts the k_e curve very well. To predict the k_e curve at ultra-high frequency, the
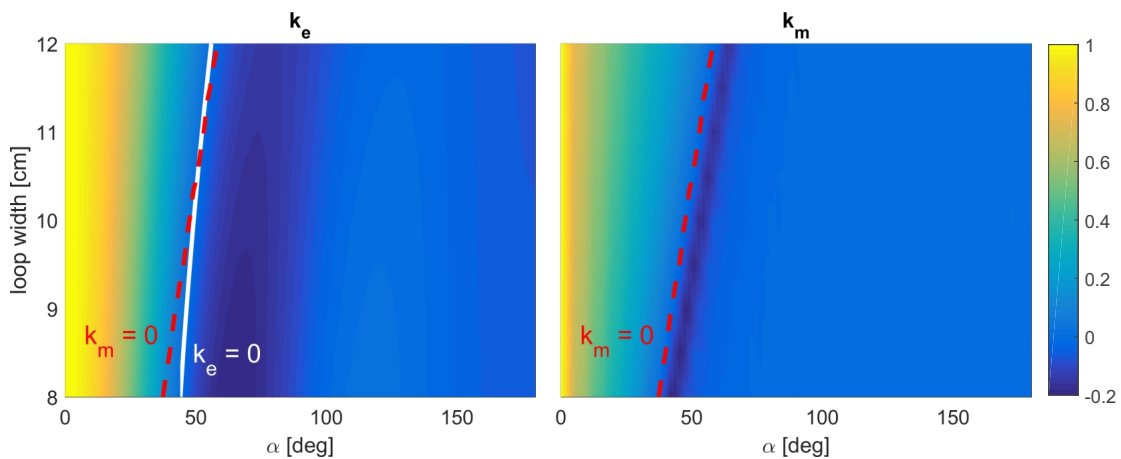

Figure 2.8: Analytic results for k_e and k_m with different loop widths at 400 MHz (85 mm phantom radius).

correlated current distribution on each loop needs to be calculated. A suitable technique for this would be the method of moments for example (73). Nevertheless, the simpler and faster analytic model is sufficient for many practical cases, because most transmit arrays have the mutual inductance compensated by either transformer decoupling or geometrical overlap.

The degree of achievable decoupling for the overlapped array depends on the variation of the head size. It needs to be emphasized that the change in S_{12} for different sample sizes is mainly caused by the variation of the loop's Q-factor and k_e value. In contrast, k_m remains almost unchanged when varying the sample radius (s. figure 5 in PUBLICATION 4). This is an important aspect, because in practice, k_m can be compensated independently of the head size.

Conclusion

An analytic model was developed to quickly evaluate the complex mutual impedance between two rectangular surface loops surrounding a cylindrical sample. Based on the model, the geometry of a two-loop array was optimized so that by overlapping the loops, both k_e and k_m were simultaneously compensated. A prototype array was constructed, which was coupled less than -40 dB without using any additional decoupling circuits. This work proved very helpful to decouple an eight channel, tight fit transceiver phased array at 400 MHz (56).
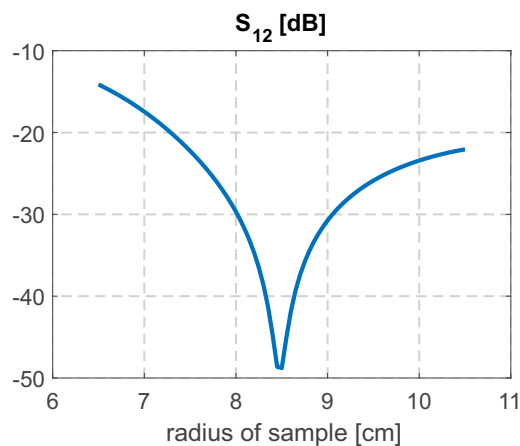
Figure 2.9: Robustness of geometrical decoupling with regard to load variation. The two-channel array is optimized to eliminate both k_e and k_m for a sample radius of 8.5 cm.

3 Bibliography

1. Levitt MH. *Spin dynamics.* Chichester: John Wiley & Sons; 2008.

2. Hoult DI. The principle of reciprocity in signal strength calculations- a mathematical guide. *Concepts Magn Reson.* 2000;12:173-187.

3. Collins CM. Numerical field calculations considering the human subject for engineering and safety assurance in MRI. *NMR Biomed.* 2009;22:919-926.

4. Chew WC. *Waves and fields in inhomogeneous media.* New York: IEEE Press Series on Electromagnetic Waves; 1995.

5. Harrington RF. *Time-harmonic electromagnetic fields.* New York: IEEE Press Series on Electromagnetic Wave Theory; 2001.

6. Hanson GW, Yakovlev AB. *Operator theory for electromagnetics.* New York: Springer; 2002.

7. Tai CT. *Dyadic Green functions in electromagnetic theory.* New York: IEEE Press Series on Electromagnetic Waves; 1994.

8. Schnell W, Renz W, Vester M, Ermert H. Ultimate signal-to-noise-ratio of surface and body antennas for magnetic resonance imaging. *IEEE Trans Antennas Propag.* 2000;48:418-428.

9. Lattanzi R, Sodickson DK. Ideal current patterns yielding optimal signal-to-noise ratio and specific absorption rate in magnetic resonance imaging: computational methods and physical insights. *Magn Reson Med.* 2012;68:286-304.

10. Jackson JD. *Classical Electrodynamics.* New York: John Wiley & Sons; 1999.

11. Gabriel S, Lau RW, Gabriel C. The dielectric properties of biological tissues: III. Parametric models for the dielectric spectrum of tissues. *Phys Med Biol.* 1996;41:2271-2293.

12. Roemer PB, Edelstein WA. Ultimate sensitivity limits of surface coils. *Proceedings of the 6th Annual Meeting of ISMRM*, New York, USA; 1987. p 410.

13. Wang J, Reykowski A, Dickas J. Calculation of the signal-to-noise ratio for simple surface coils and arrays of coils. *IEEE Trans Biomed Eng.* 1995;42:908-917.

14. Ocali O, Atalar E. Ultimate intrinsic signal-to-noise ratio in MRI. *Magn Reson Med.* 1998;39:462-473.

15. Ohliger MA, Grant AK, Sodickson DK. Ultimate intrinsic signal-to-noise ratio for parallel MRI: electromagnetic field considerations. *Magn Reson Med.* 2003;50:1018-1030.

16. Wiesinger F, Boesiger P, Pruessmann KP. Electrodynamics and ultimate SNR in parallel MR imaging. *Magn Reson Med.* 2004;52:376-390.

17. Pruessmann KP, Weiger M, Scheidegger MB, Boesiger P. SENSE: sensitivity encoding for fast MRI. *Magn Reson Med.* 1999;42:952-962.

18. Lattanzi R, Wiggins GC, Zhang B, Duan Q, Brown R, Sodickson DK. Approaching ultimate intrinsic signal-to-noise ratio with loop and dipole antennas. *Magn Reson Med.* 2018;79:1789-1803.

19. Sodickson DK, Wiggins GC, Chen G, Lakshmanan K, Lattanzi R. More than meets the eye: the mixed character of electric dipole coils, and implications for high-field performance. *Proceedings of the 24th Annual Meeting of ISMRM*, Singapore, Singapore, 2016. p. 389.

20. Vaidya MV, Sodickson DK, Lattanzi R. Approaching ultimate intrinsic SNR in a uniform spherical sample with finite arrays of loop coils. *Concepts Magn Reson Part B.* 2014;44:53-65.

21. Chen G, Cloos M, Sodickson D, Wiggins G. A 7T 8 channel transmit-receive dipole array for head imaging: dipole element and coil evaluation. *Proceedings of the 22nd Annual Meeting of ISMRM*, Milan, Italy; 2014. p 621.

22. Lagore RL, DelaBarre L, Tian J, Adriany G, Eryaman Y, Vaughan JT. End-loaded dipole array for 10.5T head imaging. *Proceedings of the 24th Annual Meeting of ISMRM*, Singapore, Singapore; 2016. p 2138.

23. Tian J, Lagore R, Delabarre L, Vaughan JT. Dipole array design considerations for head MRI at 10.5T. *Proceedings of the 24th Annual Meeting of ISMRM*, Singapore, Singapore; 2016. p 3524.

24. Zhang B, Chen G, Cloos M, Yu Z, Walczyk J, Collins C, Brown R, Lattanzi R, Sodickson D, Wiggins G. 29-channel receive-only dense dipole head array for 7T MRI. *Proceedings of the 25th Annual Meeting of ISMRM*, Honolulu, USA; 2017. p 4314.

25. Oh C, Lee C, Kumar S, Yoon J, Jeong H, Kim J, Jo Y, Kim J, Bruns C, Herrmann T, Bernarding J, Cho Z. Top-hat dipole RF coil with large field of view for 7 T brain MR imaging. *Proceedings of the 25th Annual Meeting of ISMRM*, Honolulu, USA; 2017. p 767.

26. Eryaman Y, Guerin B, Kosior R, Adalsteinsson E, Wald LL. Combined loop + dipole arrays for 7 T brain imaging. *Proceedings of the 21st Annual Meeting of ISMRM*, Salt Lake City, USA; 2013. p 393.

27. Chen G, Lakshmanan K, Sodickson D, Wiggins G. A combined electric dipole and loop head coil for 7T head imaging. *Proceedings of the 23rd Annual Meeting of ISMRM*, Toronto, Canada; 2015. p 3133.

28. Woo MK, Lagore RL, DelaBarre L, Lee BY, Eryaman Y, Radder J, Erturk A, Metzger G, van de Moortele PF, Ugurbil K, Adriany G. A geometrically adjustable loop-dipole (LD) head array for 10.5T. *Proceedings of the 25th Annual Meeting of ISMRM*, Honolulu, USA; 2017. p 1051.

29. Raaijmakers AJE, Ipek O, Klomp DWJ, Possanzini C, Harvey PR, Lagendijk JJW, van den Berg CAT. Design of a radiative surface coil array element at 7 T: the single-side adapted dipole antenna. *Magn Reson Med.* 2011;66:1488-1497.

30. Winter L, Özerdem C, Hoffmann W, Santoro D, Müller A, Waiczies H, Seemann R, Graessl A, Wust P, Niendorf T. Design and evaluation of a hybrid radiofrequency applicator for magnetic resonance imaging and RF induced hyperthermia: electromagnetic field simulations up to 14.0 Tesla and proof-of-concept at 7.0 Tesla. *PLOS ONE.* 2013;8:e61661.

31. Wiggins GC, Zhang B, Lattanzi R, Chen G, Sodickson D. The electric dipole array: an attempt to match the ideal current pattern for central SNR at 7 Tesla. *Proceedings of the 20th Annual Meeting of ISMRM*, Melbourne, Australia; 2012. p 541.

32. Raaijmakers AJE, Italiaander M, Voogt IJ, Luijten PR, Hoogduin JM, Klomp DWJ, van den Berg CAT. The fractionated dipole antenna: a new antenna for body imaging at 7 Tesla. *Magn Reson Med.* 2016;75:1366-1374.

33. Steensma B, Andrade AVO, Klomp D, van den Berg N, Luijten P, Raaijmakers A. Body imaging at 7 Tesla with much lower SAR levels: an introduction of the snake antenna array. *Proceedings of the 24th Annual Meeting of ISMRM*, Singapore, Singapore; 2016. p 395.

34. Connell IRO, Menon RS. Decoupling and integration of electric dipoles into RF arrays. *Proceedings of the 25th Annual Meeting of ISMRM*, Honolulu, USA; 2017. p 4295.

35. Wang ZJ. Towards a complete coil array. *MRI.* 2008;26:1310-1315.

36. Wang ZJ. Improving SNR of RF coils using composite coil elements. *NMR Biomed.* 2009;22:952-959.

37. Maunder A, Fallone BG, Daneshmand M, De Zanche N. Experimental verification of SNR and parallel imaging improvements using composite arrays. *NMR in Biomed.* 2015;28:141-153.

38. Lakshmanan K, Cloos M, Lattanzi R, Sodickson D, Wiggins G. The loopole antenna: capturing magnetic and electric dipole fields with a single structure to improve transmit and receive performance. *Proceedings of the 22nd Annual Meeting of ISMRM*, Milan, Italy; 2014. p 397.

39. Avdievich NI, Giapitzakis IA, Pfrommer A, Borbath T, Henning A. Combination of surface and 'vertical' loop elements improves receive performance of a human head transceiver array at 9.4 T. *NMR in Biomed.* 2018;31:e3878.

40. Pfrommer A, Henning A. On the contribution of curl-free current patterns to the ultimate intrinsic signal-to-noise ratio at ultra-high field strength. *NMR Biomed.* 2017;30:e3691.

41. Christ A, Kainz W, Hahn EG, Honegger K, Zefferer M, Neufeld E, Rascher W, Janka R, Bautz W, Chen J, Kiefer B, Schmitt P, Hollenbach HP, Shen J, Oberle M, Szczerba D, Kam A, Guag JW, Kuster N. The virtual family- development of surface-based anatomical models of two adults and two children for dosimetric simulations. *Phys Med Biol.* 2010;55:N23-N38.

42. Felder J, Shah NJ. Ultimate Intrinsic Signal-to-Noise Ratio of the Human Head at 9.4T. *Proceedings of the 19th Annual Meeting of ISMRM*, Montréal, Canada; 2011. p 3878.

43. Guérin B, Villena JF, Polimeridis AG, Adalsteinsson E, Daniel L, White JK, Wald LL. The Ultimate Signal-to-Noise Ratio in Realistic Body Models. *Magn Reson Med.* 2017;78:1969-1980.

44. Davidson DB. *Computational electromagnetics for RF and microwave engineering.* Cambridge: Cambridge university press; 2011.

45. Polimeridis AG, Villena JF, Daniel L, White JK. Stable FFT-JVIE solvers for fast analysis of highly inhomogeneous dielectric objects. *J Comput Phys.* 2014;269:280-296.

46. Villena JF, Polimeridis AG, Wald LL, Adalsteinsson E, White JK, Daniel L. MARIE – a MATLAB-based open source software for the fast electromagnetic analysis of MRI systems. *Proceedings of the 23rd Annual Meeting of ISMRM*, Toronto, Canada; 2015. p 709.

47. Villena JF, Polimeridis AG, Eryaman Y, Adalsteinsson E, Wald LL, White JK, Daniel L. Fast electromagnetic analysis of MRI transmit RF coils based on accelerated integral equation methods. *IEEE Trans Biomed Eng.* 2016;63:2250-2261.

48. Hoult DI, Lauterbur PC. The sensitivity of the zeugmatographic experiment involving human samples. *J Magn Reson.* 1979;34:425-433.

49. Redpath TW. Signal-to-noise ratio in MRI. *Br J Radiol.* 1998;71:704-707.

50. Pohmann R, Speck O, Scheffler K. Signal-to-noise ratio and MR tissue parameters in human brain imaging at 3, 7, and 9.4 Tesla using current receive coil arrays. *Magn Reson Med.* 2016;75:801-809.

51. Vaughan JT, Garwood M, Collins CM, Liu W, DelaBarre L, Adriany G, Andersen P, Merkle H, Goebel R, Smith MB, Ugurbil K. 7T vs. 4T: RF power, homogeneity, and signal-to-noise comparison in head images. *Magn Reson Med.* 2001;46:24-30.

52. Avdievich NI. Transceiver-phased arrays for human brain studies at 7 T. *Appl Magn Reson.* 2011;41:483-506.

53. Adriany G, Van de Moortele PF, Ritter J, Moeller S, Auerbach EJ, Akgün C, Snyder CJ, Vaughan T, Uğurbil K. A geometrically adjustable 16-channel transmit/receive transmission line array for improved RF efficiency and parallel imaging performance at 7 Tesla. *Magn Reson Med.* 2008;59:590-597.

54. Adriany G, Auerbach EJ, Snyder CJ, Gözübüyük A, Moeller S, Ritter J, Van de Moortele PF, Vaughan T, Uğurbil K. A 32-channel lattice transmission line array for parallel transmit and receive MRI at 7 tesla. *Magn Reson Med.* 2010;63:1478-1485.

55. Gilbert KM, Belliveau JG, Curtis AT, Gati JS, Klassen LM, Menon RS. A conformal transceive array for 7 T neuroimaging. *Magnetic Resonance in Medicine.* 2012;67:1487-1496.

56. Avdievich NI, Giapitzakis IA, Pfrommer A, Henning A. Decoupling of a tight-fit transceiver phased array for human brain imaging at 9.4T: loop overlapping rediscovered. *Magn Reson Med.* 2018;79:1200-1211.

57. Shajan G, Kozlov M, Hoffmann J, Turner R, Scheffler K, Pohmann R. A 16-channel dual-row transmit array in combination with a 31-element receive array for human brain imaging at 9.4 T. *Magn Reson Med.* 2014;71:870-879.

58. Ibrahim TS, Lee R, Baertlein BA, Abduljalil AM, Zhu H, Robitaille PML. Effect of RF coil excitation on field inhomogeneity at ultra high fields: a field optimized TEM resonator. *Magn Reson Imaging.* 2001;19:1339-1347.

59. Collins CM, Liu W, Swift BJ, Smith MB. Combination of optimized transmit arrays and some receive array reconstruction methods can yield homogeneous images at very high frequencies. *Magn Reson Med.* 2005;54:1327-1332.

60. Mao W, Smith MB, Collins CM. Exploring the limits of RF shimming for high-field MRI of the human head. *Magn Reson Med.* 2006;56:918-922.

61. Hoffmann J, Shajan G, Scheffler K, Pohmann R. Numerical and experimental evaluation of RF shimming in the human brain at 9.4 T using a dual-row transmit array. *Magn Reson Mater Phy.* 2014;27:373-386.

62. Katscher U, Börnert P, Leussler C, van den Brink JS. Transmit SENSE. *Magn Reson Med.* 2003;49:144-150.

63. Zhu Y. Parallel excitation with an array of transmit coils. *Magn Reson Med.* 2004;51:775-784.

64. Setsompop K, Wald LL, Alagappan V, Gagoski B, Hebrank F, Fontius U, Schmitt F, Adalsteinsson E. Parallel RF transmission with eight channels at 3 Tesla. *Magn Reson Med.* 2006;56:1163-1171.

65. Lattanzi R, Sodickson DK, Grant AK, Zhu Y. Electrodynamic constraints on homogeneity and radiofrequency power deposition in multiple coil excitations. *Magn Reson Med.* 2009;61:315-334.

66. Lee RF, Giaquinto RO, Hardy CJ. Coupling and decoupling theory and its application to the MRI phased array. *Magn Reson Med.* 2002;48:203-213.

67. Roemer PB, Edelstein WA, Hayes CE, Souza SP, Mueller OM. The NMR phased array. *Magn Reson Med.* 1990;16:192-225.

68. Wright SM. Full-wave analysis of planar radiofrequency coils and coil arrays with assumed current distribution. *Concepts Magn Reson B: Magn Reson Eng.* 2002;15:2-14.

69. Wei PS, King SB, Smith MJ, Matwiy J, Bidinosti CP. Accurate phased array modeling in the presence of coupling. *Proceedings of the 21st Annual Meeting of ISMRM,* Salt Lake City, USA; 2013. p 2721.

70. Vesselle H, Collin R. The signal-to-noise ratio of nuclear magnetic resonance surface coils and application to a lossy dielectric cylinder model—I: Theory. *IEEE Trans Biomed Eng.* 1995;42:497-506.

71. Vesselle H, Collin R. The signal-to-noise ratio of nuclear magnetic resonance surface coils and application to a lossy dielectric cylinder model—II: The case of cylindrical window coils. *IEEE Trans Biomed Eng.* 1995;42:507-520.

72. Avdievich NI, Hoffmann J, Shajan G, Pfrommer A, Giapitzakis IA, Scheffler K, Henning A. Evaluation of transmit efficiency and SAR for a tight fit transceiver human head phased array at 9.4 T. *NMR in Biomed.* 2017;30:e3680.

73. Harrington RF. Matrix methods for field problems. *Proc IEEE.* 1967;55:136-149.

4 Appended Publications

The following scientific articles are appended:

PUBLICATION 1: Pfrommer A, Henning A. On the contribution of curl-free current patterns to the ultimate intrinsic signal-to-noise ratio at ultra-high field strength. *NMR Biomed.* 2017;30:e3691.

PUBLICATION 2: Pfrommer A, Henning A. The ultimate intrinsic signal-to-noise ratio of loop- and dipole-like current patterns in a realistic human head model. *Magn Reson Med.* 2018. doi: 10.1002/mrm.27169.

PUBLICATION 3: Pfrommer A, Henning A. On the superlinear increase of the ultimate intrinsic signal-to-noise ratio with regard to main magnetic field strength in a spherical sample. *IEEE International Conference on Electromagnetics in Advanced Applications (ICEAA).* 2017; 684-687.

PUBLICATION 4: Avdievich* NI, Pfrommer* A, Giapitzakis IA, Henning A. Analytical modeling provides new insight into complex mutual coupling between surface loops at ultrahigh fields. *NMR in Biomed.* 2017;30:e3759.

Publication 1

WILEY NMR IN BIOMEDICINE

RESEARCH ARTICLE

On the Contribution of Curl-Free Current Patterns to the Ultimate Intrinsic Signal-to-Noise Ratio at Ultra-High Field Strength

Andreas Pfrommer[1] | Anke Henning[1,2]

[1]Max Planck Institute for Biological Cybernetics, High-Field Magnetic Resonance Center, Tuebingen, Germany

[2]Ernst-Moritz-Arndt University Greifswald, Institute of Physics, Greifswald, Germany

Correspondence

Andreas Pfrommer, Max Planck Institute for Biological Cybernetics, High-Field Magnetic Resonance Center, Spemannstrasse 41, 72076, Tuebingen, Germany.
Email: andreas.pfrommer@tuebingen.mpg.de

The ultimate intrinsic signal-to-noise ratio (SNR) is a coil independent performance measure to compare different receive coil designs. To evaluate this benchmark in a sample, a complete electromagnetic basis set is required. The basis set can be obtained by curl-free and divergence-free surface current distributions, which excite linearly independent solutions to Maxwell's equations. In this work, we quantitatively investigate the contribution of curl-free current patterns to the ultimate intrinsic SNR in a spherical head-sized model at 9.4 T. Therefore, we compare the ultimate intrinsic SNR obtained with having only curl-free or divergence-free current patterns, with the ultimate intrinsic SNR obtained from a combination of curl-free and divergence-free current patterns. The influence of parallel imaging is studied for various acceleration factors. Moreover results for different field strengths (1.5 T up to 11.7 T) are presented at specific voxel positions and acceleration factors. The full-wave electromagnetic problem is analytically solved using dyadic Green's functions. We show, that at ultra-high field strength ($B_0 \geqslant 7T$) a combination of curl-free and divergence-free current patterns is required to achieve the best possible SNR at any position in a spherical head-sized model. On 1.5- and 3T platforms, divergence-free current patterns are sufficient to cover more than 90% of the ultimate intrinsic SNR.

KEYWORDS

dipole antenna, dyadic Green's functions, electrodynamics, RF coils, ultimate intrinsic SNR

1 | INTRODUCTION

When moving towards ultra-high field magnetic resonance imaging (MRI) the wavelength of the radio frequency (RF) magnetic field is smaller than the human body dimensions and the free-space wavelength cannot be assumed to be much larger than the conductor dimensions of the RF coils. This presents a huge engineering challenge regarding the design of RF coils at ultra-high frequencies and has resulted in a variety of new coil designs.[1-8]

To compare different coil designs, it is essential to have a benchmark. In the receive case, one possible benchmark is the signal-to-noise ratio (SNR) which is the ratio of the received signal voltage divided by the accumulated noise voltage from the sample and coil. However, the received signal voltage depends also on the imaging technique and imaging parameter being applied and the received noise voltage depends on the electronic noise in the receiver chain of the MR scanner.

Edelstein et al.[9,10] suggested a procedure to measure an intrinsic SNR that is independent of any imaging technique/parameter and the receiving electronics of the MRI system. Nonetheless, this reference value still depends on the coil geometry. In a fundamental paper,[11] Ocali investigated the so called ultimate intrinsic SNR, which is instead an ultimate benchmark, because the intrinsic SNR is only limited by Maxwell's equations themselves and is not based on a specific coil geometry. In contrast to earlier works,[12,13] these authors solved Maxwell's equations without a quasistatic assumption. Their underlying model assumes, that the only source of noise is the RF power dissipated in the human body. All other noise sources such as conductor losses, radiation losses, lumped element losses or noisy receive electronics are excluded. As a consequence, the ultimate intrinsic SNR is an upper bound for the measured intrinsic SNR of any real coil configuration. Mathematically speaking, finding the ultimate intrinsic SNR is a cooptimization problem where the optimization variables

---

Abbreviations: RF, radiofrequency; SENSE, sensitivity encoding; SNR, signal-to-noise ratio;

are expansion coefficients of a basis set of electromagnetic solutions to Maxwell's equations in a given sample. The goal is to minimize the noise voltage, under the constraint that the value of the differential signal voltage is constant.[11] With the invention of parallel imaging methods[14–16] the concept of ultimate intrinsic SNR was extended by Ohliger[17] and Wiesinger.[18] Both used the weak SENSE approach[15] as a constraint in the optimization procedure. Schnell et al.,[19] derived the ultimate intrinsic SNR for surface and body coils with a dyadic Green's function approach. The author was able to show, that curl-free current patterns do not contribute to the ultimate intrinsic SNR along the z-axis of a cylinder for frequencies below 100 MHz. Recently Lattanzi et al. presented ideal current patterns that indicate how an optimal receive array must be designed to reach the ultimate intrinsic SNR in a cylinder and a sphere.[20] These authors found out, that curl-free current patterns can significantly contribute to SNR at higher

field strengths and specific voxel positions. However, Lattanzi et al. did not quantify this contribution and only considered a few voxel positions. By visually inspecting ideal current patterns, their analysis was meant to be only qualitatively. The influence of parallel imaging was not investigated either. So far, all mentioned literature is limited to simple geometrical models as (elliptical) cylinders,[11,17,19,20] spheres[18,20] and half-spaces.[19] To our knowledge, the first preliminary results dealing with the ultimate intrinsic SNR in a realistic body model were published by Felder.[21] The author used plane waves impinging on a human head model to create the basis set. In his model, there are no current patterns exciting the plane waves. Therefore it is not possible to separate the contribution of curl-free and divergence-free current patterns. Recently Guerin et al. presented a different method.[22] Thereby the electromagnetic basis set was numerically created by randomly exciting many dipole elements on a body conformed surface. However, with

TABLE 1 Symbols used in this work

$A_{M,N}^{22}$	boundary coefficients for $\bar{G}_e^{22}$
$\alpha_{l,m}^M, \alpha_{l,m}^E$	expansion coefficient for magnetic-/electric-type current expansion
$\tilde{\alpha}_{l,m}^M, \tilde{\alpha}_{l,m}^E$	expansion coefficient for magnetic-/electric-type multipole expansion
B	magnetic field vector
$\mathcal{B}_i$	basis set of magnetic fields inside head region
$B_{M,N}^{22}$	boundary coefficients for $\bar{G}_e^{22}$
$C_{M,N}^{22}, C_{M,N}^{32}$	boundary coefficients for $\bar{G}_e^{22}$ and $\bar{G}_e^{32}$
$D_{M,N}^{22}, D_{M,N}^{32}$	boundary coefficients for $\bar{G}_e^{22}$ and $\bar{G}_e^{32}$
$\delta(r)$	Dirac-Delta distribution
$\delta_{ll'}$	Kronecker-Delta
ε_0, μ_0	vacuum permittivity, permeability
E	electric field vector
$\mathcal{E}_i$	basis set of electric fields inside head region
ζ	ultimate intrinsic SNR
ϑ	polar angle in spherical coordinate system
$\bar{G}_e^{jk}$	electric dyadic Green's function with field in layer j and source in layer k
$h_l^{(1)}$	spherical Hankel function of first kind
i	imaginary unit: $\sqrt{-1}$
$I, \mathbf{J}$	amplitude of volume current density, volume current density
j_l	spherical Bessel function
k_0, k	propagation constant in vacuum/head layer
L, M, N	Stratton's fundamental solutions to homogeneous Helmholtz equation
P_l^m	associated Legendre function of degree l and order m
ρ	acceleration factor in parallel imaging
$\mathbf{r}, \mathbf{r}'$	field point in 3D space, source point in 3D space
r	radial variable in spherical coordinate system
R_c, R_h, R_s	radius of surface current distribution, head and shield
S	receive sensitivity matrix
σ	electric conductivity in head layer
φ	azimuth angle in spherical coordinate system
Ψ	noise covariance matrix
ω	angular Lamor frequency
Ω	solid angle of a sphere with $d\Omega = \sin\vartheta d\vartheta d\varphi$
$V_{l,m}^M, V_{l,m}^E$	extended boundary coefficients
$\mathbf{X}_{l,m}$	Jackson's vector spherical harmonic of degree l and order m
$Y_{l,m}$	scalar spherical harmonic of degree l and order m

this approach, the surface current patterns are a random combination of curl-free and divergence-free current patterns and the contribution of each component to the ultimate intrinsic SNR cannot be evaluated.

In this work, we quantitatively investigate the contribution of curl-free current patterns to the ultimate intrinsic signal-to-noise ratio in a spherical model approximating the human head. We quantitatively compare the ultimate intrinsic SNR obtained with divergence-free only or curl-free only current patterns with the ultimate intrinsic SNR obtained from a combination of curl-free and divergence-free current patterns. This analysis is done for all voxel positions in the spherical model at 9.4 T field strength. The influence of parallel imaging is studied for various acceleration factors. Moreover, we present results for specific voxel positions at 1.5 T, 3 T, 7 T and 11.7 T. Based on our analysis, we finally deduce practical guidelines for RF coil design regarding head applications at different field strengths. This includes fields strength specific recommendations of combining dipole and loop elements.

2 | THEORY

2.1 | The Ultimate Intrinsic SNR

We are interested in the ultimate intrinsic SNR in the human head, which we approximate by a uniform sphere. Wiesinger obtained an expression for the ultimate intrinsic SNR ζ in the case of Cartesian parallel imaging[18]:

$$\zeta(\mathbf{r}_0) \propto \frac{1}{\sqrt{\left[\left(\mathbf{S}^H \mathbf{\Psi}^{-1} \mathbf{S}\right)^{-1}\right]_{0,0}}} \quad (1)$$

In this formula (see Table 1 and appendix for mathematical notation) we obtain the ultimate intrinsic SNR at voxel position $\mathbf{r}_0$ by taking the first diagonal entry of the matrix expression $(\mathbf{S}^H \mathbf{\Psi}^{-1} \mathbf{S})^{-1}$. We ignore all proportionality constants because we are only interested in SNR ratios, such as $\text{SNR}_{\text{div-free}}/\text{SNR}_{\text{div-free + curl-free}}$. The receive sensitivity matrix $\mathbf{S}$ consists of the sensitivities of all basis vectors at the original voxel position $\mathbf{r}_0$ and all aliased positions.[23] The receive sensitivity of an RF coil at position $\mathbf{r}_0$ can be calculated by the principle of reciprocity from the complex left-handed component of the circularly polarized RF magnetic field[20,24]:

$$S(\mathbf{r}_0) = \frac{B_x(\mathbf{r}_0) - iB_y(\mathbf{r}_0)}{2}. \quad (2)$$

Note that the induced signal voltage in the receiver coil is proportional to the complex conjugate of the transverse RF field component which rotates in the opposite direction as nuclear precession.[24]

The system's noise covariance matrix $\mathbf{\Psi}$ describes the noise received by each basis vector and the correlated noise between different basis vectors.[23] The element $\Psi_{j,k}$ refers to basis vector number j and k and is related to the overlap integral of the electric fields of the corresponding basis vectors [25,26]:

$$\Psi_{j,k} = \int_{\text{sample}} \sigma(\mathbf{r}) \mathbf{E}_j \cdot \mathbf{E}_k^* \, dV. \quad (3)$$

2.2 | Electromagnetic Fields in a Spherically Multilayered Model

In Figure 1 we show a proposed simplified three-layered spherical model mimicking the electromagnetic field problem of an electric current distribution $\mathbf{J}$ surrounding the human head in the presence of an electric shield. For the rest of the paper, we assume that a perfect conducting metallic shield is placed at a distance of $R_1 = R_s$ and completely fills layer one. No electromagnetic fields can penetrate into the first layer and we have $|k_1| = \infty$. Furthermore, let the second layer of our model be a vacuum with propagation constant $k_2 = k_0$. The electric current distribution $\mathbf{J}$ may flow entirely on a spherical surface at a distance $R_s \geqslant R_c \geqslant R_h$, where $R_2 = R_h$ is the radius of the "head" and the interface between layers two and three. The electromagnetic properties in the "head layer" are specified by the conductivity σ and relative permittivity ε_r. Both are frequency dependent as documented in the table in Figure 1. With a time harmonic dependence of $\exp(-i\omega t)$ the complex propagation constant in layer three becomes $k_3 = k = \omega\sqrt{\mu_0 \varepsilon_0 \varepsilon_r(1 + i\sigma/(\omega \varepsilon_0 \varepsilon_r))}$. In order to calculate the ultimate intrinsic SNR in the "head region" (layer 3), the knowledge of a complete basis set of all possible solutions to Maxwell's equations within this region is essential. If such a basis set is known, all electric and magnetic fields can be calculated as a linear combination of this basis set[18]:

$$\mathbf{E}_{\text{head}} = \sum_i \tilde{\alpha}_i \mathcal{E}_i \quad (4)$$

$$\mathbf{B}_{\text{head}} = \sum_i \tilde{\alpha}_i \mathcal{B}_i \quad (5)$$

Having an infinite dimensional vector space, the basis set needs to be truncated in numerical simulations. There exists an analytic basis set for spherical setups. This will be derived in the following. To start with, the homogeneous free-space Helmholtz equation for any vector quantity $\mathbf{A}$ is given by:

$$\nabla\nabla \cdot \mathbf{A} - \nabla \times \nabla \times \mathbf{A} + k_0^2 \mathbf{A} = \mathbf{0}. \quad (6)$$

In a spherical coordinate system Stratton observed that there are three linearly independent solutions to the above Helmholtz equation[27]:

$$\mathbf{L}_{l,m}(k_0 r, \vartheta, \varphi) = \nabla j_l(k_o r) Y_{l,m}(\vartheta, \varphi) \quad (7)$$

$$\mathbf{M}_{l,m}(k_0 r, \vartheta, \varphi) = j_l(k_0 r) \mathbf{X}_{l,m}(\vartheta, \varphi) \quad (8)$$

$$\mathbf{N}_{l,m}(k_0 r, \vartheta, \varphi) = \frac{1}{k_0} \nabla \times \mathbf{M}_{l,m} \quad (9)$$

Here, we slightly adapted the definition of the $\mathbf{L}$, $\mathbf{M}$ and $\mathbf{N}$ solution by using Jackson's scalar spherical harmonic Y and vector spherical harmonic $\mathbf{X}$ (see Equations (A1)–(A3) in the appendix). The reason for this change is to make $\mathbf{M}$ and $\mathbf{N}$ orthonormal over the unit sphere (Equations (A9)–(A15) in the appendix). It can be shown that these three linearly independent solutions create a complete basis set.[28] For our purpose, these solutions will be linked to the electric $\mathbf{E}$- and magnetic $\mathbf{B}$-fields. While the $\mathbf{B}$-field is always a purely solenoidal field ($\nabla \cdot \mathbf{B} = 0$), for the $\mathbf{E}$-field this is only true in source-free matter, i.e. matter with no free-volume charges. As this is the case for most dielectric materials and good conductors (e.g. gold, silver, copper), we will assume that the electric field is also purely solenoidal. This is in accordance with the models used in the cited literature, including the work of Wiesinger[18] and Lattanzi.[20] As a consequence, the solution space is only spanned by the $\mathbf{M}$- and $\mathbf{N}$-solutions. At this point, the field expansion in the "head"-layer (s. Equations (4), (5)) can be specified by the fundamental solutions given in Equations (8) and (9). Since the wave
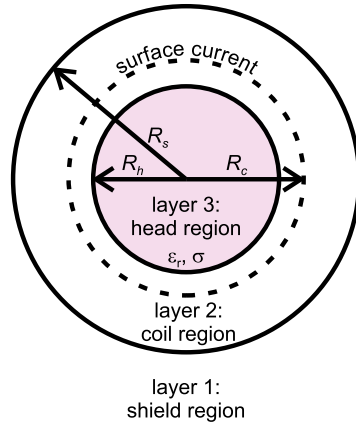
Electromagnetic properties for the „head" region:

The values for the permittivity and conductivity are averaged for gray and white matter.

B_0 [T]	1.5	3	7	9.4	11.7
ε_r	82.7	63.1	52.0	49.8	48.4
σ [S/m]	0.40	0.46	0.55	0.59	0.63

FIGURE 1 We model the electromagnetic field problem of an electric current distribution surrounding the human head in the presence of an electric shield. For this, we used a simplified three-layered spherical setup. The outermost layer (number one) starts at a radius of R_s and extends to infinity. It represents the RF shield and is completely filled with perfect conducting material. The second layer is filled with vacuum and extends between R_s and R_h. In this layer a surface current distribution of divergence-free and curl-free current patterns is flowing on a sphere at a radius of R_c. The innermost layer (number three) models the human head and the radius of the sphere is R_h. The electromagnetic properties of the "head" region are summarized in the table to the right for different field strengths. The values for the permittivity and conductivity are averaged for gray and white matter according to Gabriel et al.[32]

propagation is no longer in free-space, the vacuum propagation constant k_0 should be replaced by the complex propagation constant k in the "head" layer:

$$\mathbf{E}_{\text{head}} \propto \sum_{l,m} \tilde{\alpha}_{l,m}^M \mathbf{M}_{l,m}(kr, \vartheta, \varphi) + \tilde{\alpha}_{l,m}^E \mathbf{N}_{l,m}(kr, \vartheta, \varphi) \qquad (10)$$

$$\mathbf{B}_{\text{head}} \propto \sum_{l,m} \tilde{\alpha}_{l,m}^M \mathbf{N}_{l,m}(kr, \vartheta, \varphi) + \tilde{\alpha}_{l,m}^E \mathbf{M}_{l,m}(kr, \vartheta, \varphi) \qquad (11)$$

Such an expansion is called a multipole expansion of an electromagnetic field.[29] In general, every electromagnetic field within the sphere is a combination of two types of fields: a magnetic multipole field with coefficients $\tilde{\alpha}_{l,m}^M$ and an electric multipole field with coefficients $\tilde{\alpha}_{l,m}^E$. Wiesinger et al.,[18] calculated the ultimate intrinsic SNR by optimizing the expansion coefficients of such a multipole expansion. In practice, the RF engineer can optimize the electromagnetic field only indirectly by using dedicated conductor geometries. We therefore follow Lattanzi's approach[20] to optimize a current distribution and afterwards calculate the excited electromagnetic field inside the "head". Any current source $\mathbf{J}$, positioned in layer 2 and flowing on a spherical surface of radius R_c, excites an electric field in the "head" layer $\mathbf{E}_{\text{head}}$ that can be obtained by dyadic Green's functions[30,31]:

$$\mathbf{E}_{\text{head}}(\mathbf{r}) = i\omega\mu_0 \int \int \int_{V_2} \bar{\mathbf{G}}_e^{(32)}(\mathbf{r}, \mathbf{r}') \cdot \mathbf{J}(\mathbf{r}') \, dV'. \qquad (12)$$

The dyadic Green's function $\bar{\mathbf{G}}_e^{(32)}$ is given in the appendix (Equation (A4)). By comparing Equation (10) with Equation (12) the expansion of the current distribution $\mathbf{J}$ must be chosen in such a way, that both solutions $\mathbf{M}$ and $\mathbf{N}$ are excited. Lattanzi et al. suggested the following expansion[20]:

$$\mathbf{J} = \frac{I}{R_c}\delta(r - R_c) \sum_{l=1}^{L} \sum_{m=-l}^{l} \alpha_{l,m}^M \mathbf{X}_{l,m}(\vartheta, \varphi) + \alpha_{l,m}^E (\hat{\mathbf{r}} \times \mathbf{X}_{l,m}(\vartheta, \varphi)). \qquad (13)$$

With the given orthogonality relations in the appendix (Equations (A9)–(A15)), the reader can convince himself that indeed both solutions are excited. It can be shown on a spherical surface with constant radius:

$\nabla \cdot \mathbf{X}_{l,m} = 0$ and $\nabla \times \hat{\mathbf{r}} \times \mathbf{X}_{l,m} = \mathbf{0}$. Therefore, the terms $\alpha_{l,m}^M$ and $\alpha_{l,m}^E$ are the expansion coefficients for the divergence-free component of the current (also denoted magnetic-type) and the curl-free component (electric-type). All divergence-free current patterns, however, are only able to excite electric fields as a linear superposition of the fundamental **M**-solution and therefore might miss important contributions from the other independent solution. Therefore, a complete current expansion has to excite both solutions. Consequently, additional curl-free current paths are needed. When combining Equations (12) and (13) and taking advantage of the orthogonality relations, the electromagnetic fields inside layer 3 can be evaluated:

$$\mathbf{E}_{\text{head}}(\mathbf{r}) = -IR_c k_0 \omega\mu_0 \sum_{l=1}^{L} \sum_{m=-l}^{l} \alpha_{l,m}^M V_{l,m}^M \mathbf{M}_{l,m} + \alpha_{l,m}^E V_{l,m}^E \mathbf{N}_{l,m} \qquad (14)$$

$$\mathbf{B}_{\text{head}}(\mathbf{r}) = iIR_c k_0 k\mu_0 \sum_{l=1}^{L} \sum_{m=-l}^{l} \alpha_{l,m}^M V_{l,m}^M \mathbf{N}_{l,m} + \alpha_{l,m}^E V_{l,m}^E \mathbf{M}_{l,m} \qquad (15)$$

The extended boundary coefficients $V_{l,m}^M$ and $V_{l,m}^E$ originate from the integration of the dot product between the primed vector functions $\mathbf{M}'_{l,m}$ or $\mathbf{N}'_{l,m}$ and the source distribution $\mathbf{J}$ over the second layer of our model:

$$V_{l,m}^M = C_M^{32} j_l(k_0 R_c) + D_M^{32} h_l^{(1)}(k_0 R_c) \qquad (16)$$

$$V_{l,m}^E = \frac{C_N^{32}}{k_0 R_c} \frac{\partial}{\partial r}(r j_l(k_0 r))\Big|_{r=R_c} + \frac{D_N^{32}}{k_0 R_c}\frac{\partial}{\partial r}\left(r h_l^{(1)}(k_0 r)\right)\Big|_{r=R_c} \qquad (17)$$

The boundary coefficients C_M^{32}, C_N^{32}, D_M^{32} and D_N^{32} are listed in the appendix in Equations (A27)–(A30). Finally, the receive sensitivity matrix $\mathbf{S}$ in Equation (1) can be calculated as in[20]:

$$\mathbf{S} = \begin{pmatrix} S_{1,-1}^M(\mathbf{r}_0) & \cdots & S_{1,-1}^M(\mathbf{r}_{\rho-1}) \\ \vdots & \ddots & \vdots \\ S_{L,L}^M(\mathbf{r}_0) & \cdots & S_{L,L}^M(\mathbf{r}_{\rho-1}) \\ S_{1,-1}^E(\mathbf{r}_0) & \cdots & S_{1,-1}^E(\mathbf{r}_{\rho-1}) \\ \vdots & \ddots & \vdots \\ S_{L,L}^E(\mathbf{r}_0) & \cdots & S_{L,L}^E(\mathbf{r}_{\rho-1}) \end{pmatrix} = \begin{pmatrix} \mathbf{S}^M \\ \mathbf{S}^E \end{pmatrix} \qquad (18)$$

The subscripts indicate the degree l and order m of the spherical harmonic. Here, the electric- and magnetic-type currents

(superscripts E and M) are treated individually as they can be seen as separate coil elements. The matrix has a total size of $2 \cdot ((L+1)^2 - 1) \times \rho$ entries. L is the maximum expansion degree in Equation (13) to reach convergence of the ultimate intrinsic SNR. ρ is the reduction factor associated with parallel imaging.[15] For two dimensional k-space under-sampling, we simply use a superindex for the aliased voxel positions and let $\rho = \rho_x \rho_y$ be the product of skipped phase encoding steps in both directions. The receive sensitivities $S^M_{l,m}(\mathbf{r})$ and $S^E_{l,m}(\mathbf{r})$ can be calculated by inserting Equation (15) into Equation (2):

$$S^M_{l,m}(\mathbf{r}) = \frac{1}{2} i l R_c k_0 \mu_0 V^M_{l,m} \left(\mathbf{N}_{l,m}(\mathbf{r})|_x - i \mathbf{N}_{l,m}(\mathbf{r})|_y \right) \quad (19)$$

$$S^E_{l,m}(\mathbf{r}) = \frac{1}{2} i l R_c k_0 \mu_0 V^E_{l,m} \left(\mathbf{M}_{l,m}(\mathbf{r})|_x - i \mathbf{M}_{l,m}(\mathbf{r})|_y \right) \quad (20)$$

The noise covariance matrix element $\Psi_{(l,m)(l',m')}$ between basis vector of degree l and order m and basis vector of degree l' and order m' can be calculated according to Equations (3) and (14):

$$\Psi_{(l,m),(l',m')} = \sigma |l R_c k_0 \omega \mu_0|^2 \int_{V_3} \left[\left(V^M_{l,m} \mathbf{M}_{l,m} + V^E_{l,m} \mathbf{N}_{l,m} \right) \cdot \right.$$
$$\left. \left(V^M_{l',m'} \mathbf{M}_{l',m'} + V^E_{l',m'} \mathbf{N}_{l',m'} \right)^* \right] dV \quad (21)$$

$$= \sigma |l R_c k_0 \omega \mu_0|^2 \int_{V_3} V^M_{l,m} \mathbf{M}_{l,m} \cdot \left(V^M_{l',m'} \mathbf{M}_{l',m'} \right)^* dV +$$
$$\sigma |l R_c k_0 \omega \mu_0|^2 \int_{V_3} V^E_{l,m} \mathbf{N}_{l,m} \cdot \left(V^E_{l',m'} \mathbf{N}_{l',m'} \right)^* dV \quad (22)$$

$$= \Psi^M_{(l,m)(l',m')} + \Psi^E_{(l,m)(l',m')}. \quad (23)$$

Note that there is no coupling between magnetic- and electric-type currents because the vector wave functions $\mathbf{M}_{l,m}$ and $\mathbf{N}_{l',m'}$ are orthogonal to each other for every l, l', m and m'. Therefore, it is possible to split the noise covariance matrix $\mathbf{\Psi}$ into a magnetic noise covariance matrix $\mathbf{\Psi}^M$ and an electric $\mathbf{\Psi}^E$:

$$\mathbf{\Psi} = \begin{pmatrix} \mathbf{\Psi}^M & \mathbf{0} \\ \mathbf{0} & \mathbf{\Psi}^E \end{pmatrix} \quad (24)$$

The individual elements for $\mathbf{\Psi}^M$ and $\mathbf{\Psi}^E$ are given to:

$$\Psi^M_{(l,m),(l',m')} = \sigma |l R_c k_0 \omega \mu_0|^2 V^M_{l,m} \left(V^M_{l',m'} \right)^* \int_{r=0}^{R_h} |j_l(kr)|^2 r^2 \, dr \, \delta_{ll'} \delta_{mm'} \quad (25)$$

$$\Psi^E_{(l,m),(l',m')} = \sigma |l R_c k_0 \omega \mu_0|^2 \frac{V^E_{l,m} \left(V^E_{l',m'} \right)^*}{|k|^2} \int_{r=0}^{R_h} \left(l(l+1)|j_l(kr)|^2 + \right.$$
$$\left. \left| \frac{\partial}{\partial r} r j_l(kr) \right|^2 \right) dr \, \delta_{ll'} \delta_{mm'} \quad (26)$$

Both the magnetic- and electric-type currents are perfectly decoupled resulting in purely diagonal matrices:

$$\mathbf{\Psi}^M = \begin{pmatrix} \Psi^M_{(1,-1)(1,-1)} & \cdots & 0 \\ \vdots & \ddots & \vdots \\ 0 & \cdots & \Psi^M_{(L,L)(L,L)} \end{pmatrix} \quad (27)$$

$$\mathbf{\Psi}^E = \begin{pmatrix} \Psi^E_{(1,-1)(1,-1)} & \cdots & 0 \\ \vdots & \ddots & \vdots \\ 0 & \cdots & \Psi^E_{(L,L)(L,L)} \end{pmatrix}. \quad (28)$$

2.3 | Contribution of the Curl-Free Current Pattern to the Ultimate Intrinsic SNR

In the last paragraph it was shown, that there is no correlation between the electric- and magnetic noise covariance matrix in our spherical

model. Therefore it is possible to rewrite Equation (1):

$$\zeta(\mathbf{r}_0) = \frac{1}{\sqrt{\left[\left((\mathbf{S}^M)^H (\mathbf{\Psi}^M)^{-1} \mathbf{S}^M + (\mathbf{S}^E)^H (\mathbf{\Psi}^E)^{-1} \mathbf{S}^E \right)^{-1} \right]_{0,0}}}. \quad (29)$$

Now we are able to define the achievable ultimate intrinsic SNR with having only divergence-free current patterns as

$$\zeta^M(\mathbf{r}_0) = \frac{1}{\sqrt{\left[\left((\mathbf{S}^M)^H (\mathbf{\Psi}^M)^{-1} \mathbf{S}^M \right)^{-1} \right]_{0,0}}}. \quad (30)$$

Accordingly, we define ζ^E as the achievable ultimate intrinsic SNR with having only curl-free current patterns:

$$\zeta^E(\mathbf{r}_0) = \frac{1}{\sqrt{\left[\left((\mathbf{S}^E)^H (\mathbf{\Psi}^E)^{-1} \mathbf{S}^E \right)^{-1} \right]_{0,0}}}. \quad (31)$$

From Equations (29)–(31) it immediately follows that $\zeta(\mathbf{r}_0) \neq \zeta^M(\mathbf{r}_0) + \zeta^E(\mathbf{r}_0)$ or in words: The ultimate intrinsic SNR obtained from both divergence-free and curl-free current patterns is not the sum of the ultimate intrinsic SNR of only divergence-free and curl-free current patterns. For the ongoing discussion we use two figure of merits: First we define the contribution of curl-free current patterns to the ultimate intrinsic SNR as the ratio ζ^E/ζ. Accordingly, we define the contribution of divergence-free current patterns to the ultimate intrinsic SNR as the ratio ζ^M/ζ. Second, we quantify the enhancement in SNR obtained by a combination of curl-free and divergence-free current patterns over divergence-free current patterns only as the term ζ/ζ^M.

Without parallel imaging and with the given diagonal noise covariance matrix of our chosen model, rewriting Equation (29) results in a more traceable expression:

$$\zeta(\mathbf{r}_0) = \frac{1}{\sqrt{\left(\sum_{l=1}^{L} \sum_{m=-l}^{l} \frac{\left| S^M_{l,m}(\mathbf{r}_0) \right|^2}{\Psi^M_{l,m}} + \frac{\left| S^E_{l,m}(\mathbf{r}_0) \right|^2}{\Psi^E_{l,m}} \right)^{-1}}}$$
$$= \sqrt{\sum_{l=1}^{L} \sum_{m=-l}^{l} \frac{\left| S^M_{l,m}(\mathbf{r}_0) \right|^2}{\Psi^M_{l,m}} + \frac{\left| S^E_{l,m}(\mathbf{r}_0) \right|^2}{\Psi^E_{l,m}}}. \quad (32)$$

The above equation illustrates the contribution of each basis vector to the final SNR at voxel position $\mathbf{r}_0$. To assess the contribution of a basis vector to the final SNR, its individual power loss (noise) and receive sensitivity (signal) must be known.

3 | METHODS

3.1 | Study Design

If not otherwise stated, we studied the ultimate intrinsic SNR within a sphere of radius 9.2 cm at a field strength of 9.4 T (400.2 MHz Lamor frequency for protons) and different acceleration factors. The electromagnetic properties of the sphere are summarized in Figure 1 and represent averaged values for gray and white matter.[32] We placed a conducting shield at a distance of 16.2 cm from the center and let a surface current flow on a spherical surface of radius 12.2 cm. To calculate the ultimate intrinsic SNR within this setup, we applied the dyadic Green's function approach,[30] the same technique that was already used by Lattanzi.[20] Lattanzi worked with a two-layerd spherical setup

(sample and coil layer). In this work, we added an additional layer (sample, coil and shield layer) and investigated the separable contributions of divergence-free and curl-free current patterns to the ultimate SNR. In the appendix (Equations (A35)–(A42)), we prove that for a spherical model the ultimate intrinsic SNR is not a function of the extended boundary coefficients V^M and V^E. In Equation (1) the extended boundary coefficients cancel out. By looking at Equations (16), (17) and Equations (A27)–(A30) it turns out that the ultimate intrinsic SNR neither depends on the radius of the shield nor on the radius of the surface current distribution. Therefore, the shied has no influence on the ultimate intrinsic SNR and our results are identical with Lattanzi's two-layered setup. This is confirmed in Supporting Figure S1 (available online). Wiesinger et al.,[18] used a multipole approach to calculate the ultimate SNR. This methods differs from the dyadic Green's function approach that instead of optimizing current patterns the electromagnetic field is directly optimized.

We first analyzed the quantitative contribution of curl-free and divergence-free current patterns to the ultimate intrinsic SNR at 9.4 T field strength and different acceleration factors. Apart from calculating the spatial distribution of the ratios ζ^E/ζ and ζ^M/ζ, we compared the results from a central and intermediate voxel position (about half of the sphere's radius above the center in the positive z-direction) with the average ratios over all voxel positions. In a next step, we investigated the SNR enhancement of a combination of curl-free and divergence-free current patterns over divergence-free current patterns alone. We proceeded with investigation of the influence of the divergence-free current type at different field strengths of 1.5 T, 3 T, 7 T, 9.4 T and 11.7 T and radii of the sphere ranging from 5 cm to 11 cm for the aforementioned distinct voxel positions. The frequency dependence of the conductivity and relative permittivity was adjusted according to Figure 1. To get a better understanding of why divergence-free and curl-free current patterns have a different contribution to the ultimate intrinsic SNR, we analyzed the power losses, as the dissipated RF power in the conducting sphere of both types individually. As SNR is the ratio of received signal voltage to noise voltage, we additionally compared the receive sensitivities (proportional to signal voltage[24]) obtained from divergence-free and curl-free current patterns for all modes up to the fourth degree on its own. We compared our results with previous work done by Lattanzi et al.[20] and plotted ideal current patterns. These authors showed, that the ideal current patterns are different for each voxel position but the impact of parallel imaging was not investigated. Therefore in this work, we visualized ideal current patterns for different voxel positions and acceleration factors. Finally, the SNR penalty of parallel imaging was measured as the ultimate g-factor.

3.2 | Algorithmic Implementation

To evaluate the analytic expressions presented in the theory section we implemented a toolbox in MatLab (MathWorks, Natick, MA) on a standard PC (six cores @ 2.3 GHz, 16 GB RAM). In the first step, the receive sensitivity matrix **S** was evaluated according to Equation (18). We used a Cartesian grid where the spatial resolution was a multiple of $2 \cdot \rho$ for the specific undersampling direction. This resulted in at most $\rho - 1$ voxels being aliased. If two-dimensional acceleration in the x- and

y-direction was investigated, there were maximally $\rho = \rho_x \rho_y - 1$ aliased voxels. For unaccelerated ultimate intrinsic SNR, we worked with 80 samples in each dimension, resulting in an isotropic resolution of 2.3 mm for a sphere of radius 92 mm. Regarding 2×2, 4×4, 5×5, 8×8 and 10×10 acceleration the number of samples was also set to 80. For 3×3 fold acceleration, we used 78 samples and for 6×6 and 7×7, we used 84 samples. In the second step we obtained the noise covariance matrix Ψ. The integrals in Equations (25) and (26) were calculated with trapezoidal numerical integration on a uniformly spaced grid. Now having obtained the receive sensitivity- and noise covariance matrices, implementation of Equation (1) is straight-forward. The inversion of the matrix product $\mathbf{S}^H \mathbf{\Psi}^{-1} \mathbf{S}$ only works well if the resulting matrix is well-conditioned. This is the case if the basis functions provide enough spatial variety to separate the aliased voxels. The more basis functions are used, the higher the spatial variety. Therefore, the number of basis functions should be chosen much larger than the acceleration factor. On the other hand increasing the number of basis functions increases the matrix size of $\mathbf{S}$ and Ψ and the computation time and memory. Therefore, setting the maximum expansion degree L is a trade-off between computational cost and convergence accuracy. We truncated the series expansion at $L = 60$. To check whether this truncation order was high enough, we investigated the convergence behavior of the ultimate intrinsic SNR for three exemplary voxel positions and all relevant field strengths prior to further analysis. For all calculations, we used floating point arithmetic with double precision.

4 | RESULTS

In Supporting Figure S2 (available online) we demonstrate the convergence of the ultimate intrinsic SNR as a function of the expansion degree l and field strength B_0 for three exemplary voxel positions. The central and intermediate voxels converge very fast, whereas the peripheral voxel has much slower convergence. This is in accordance with previous studies.[17,18] Having ensured that our results converged sufficiently, we illustrate the contribution of curl-free and divergence-free current patterns to the ultimate intrinsic SNR at 9.4 T field strength in Figure 2. Up to an acceleration of 5×5, the curl-free current has substantial contribution to the ultimate intrinsic SNR in the intermediate region of the xz/yz- plane of the sphere. The asymmetry between xy- and xz/yz- plane is due to the alignment of B_0 in z-direction. For the peripheral part of the sphere, only the divergence-free currents contribute to the ultimate intrinsic SNR regardless of what acceleration is applied. For low acceleration factors ($\rho \leqslant 3x3$), central SNR is completely dominated by divergence-free current patterns.

The bar chart in Figure 3 shows the (normalized) achievable ultimate intrinsic SNR obtained by divergence-free only (ζ^M/ζ) or curl-free only (ζ^E/ζ) current patterns. Averaged over the entire sphere, divergence-free currents achieve always more than 90% (Figure 3a) of the ultimate intrinsic SNR. Curl-free current patterns achieve in average around 30% of the ultimate intrinsic SNR, if the acceleration is in a practically applicable regime. We also calculated the ratios ζ^M/ζ and ζ^E/ζ for two distinct voxel positions (indicated with "+" and "o" in Figure 2). For the central voxel position, divergence-free current patterns alone reach the ultimate value for low acceleration
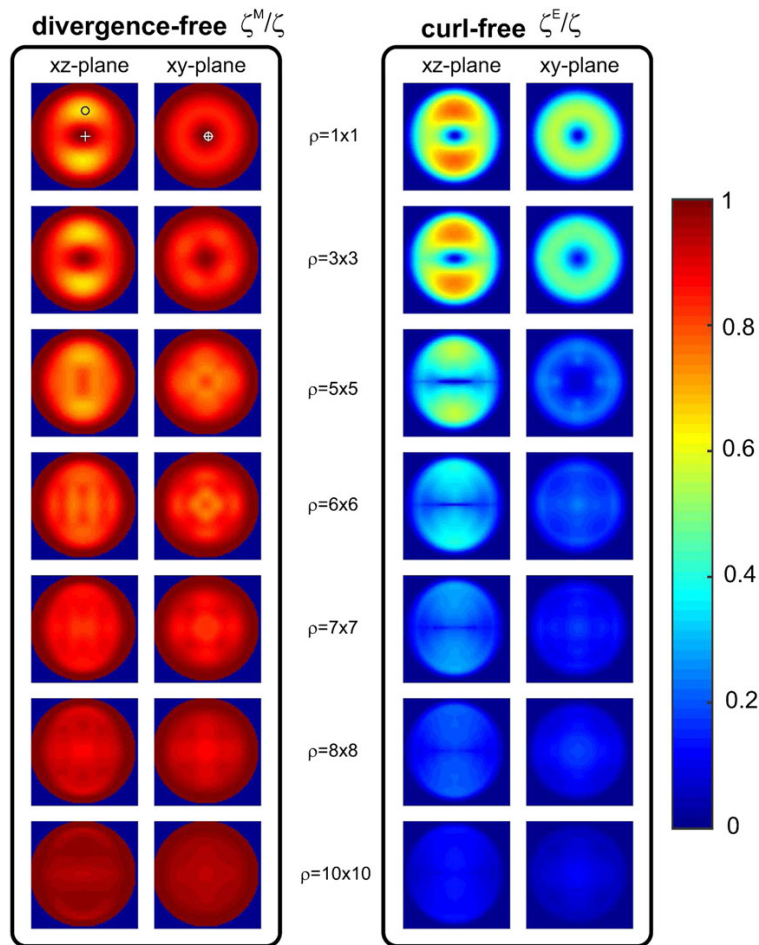
FIGURE 2 The contribution of the divergence-free current to the ultimate intrinsic SNR is plotted as the ratio ζ^M/ζ for a range of acceleration factors (left column). Accordingly, the contribution of the curl-free current to the ultimate intrinsic SNR is shown as the ratio ζ^E/ζ (right column). By ζ^M, we mean the ultimate intrinsic SNR obtained when only divergence-free (magnetic-type) current patterns are used as a basis set. Analogously by ζ^E, we mean the ultimate intrinsic SNR obtained when only curl-free (electric-type) current patterns are used as a basis set. The total ultimate intrinsic SNR ζ is obtained from a complete basis set of divergence-free and curl-free current patterns. Phase encoding was assumed to be in x- and y-direction. The cutting planes are close to the center. Due to the spherical geometry and chosen phase encoding direction the distribution is rotationally symmetric about the z-axis

factors, whereas curl-free current patterns are hardly able to gain any SNR (Figure 3b). Regarding the intermediate voxel position, Figure 3c shows, that curl-free current patterns alone are more efficient than divergence-free current patterns alone for low acceleration factors. However, this is a very small region compared to the whole sphere. In Figure 4 we demonstrate the enhancement in SNR obtained by a combination of curl-free and divergence-free current patterns over divergence-free current patterns alone as the term ζ/ζ^M. By considering all the voxels in the sphere, the average SNR gain is slightly more than 10% for lower acceleration factors. We found that the maximum achievable SNR gain is about 57% for $\rho \leqslant 4x4$. Again, we calculated the ratio ζ/ζ^M for the aforementioned two distinct voxel positions. In the case of low acceleration ($\rho \leqslant 2x2$), adding curl-free current patterns does not significantly increase SNR at a central voxel position. On the other hand, the intermediate voxel position benefits from the additional curl-free current patterns by an SNR increase of 57%.

In Figure 5, we show the contribution of the divergence-free current at an intermediate and central voxel position for a sweep through the parameter space $B_0 \in \{1.5, 3, 7, 9.4, 11.7\}$ T, $R_h \in [5,11]$ cm and $\rho \in \{1 \times 1, 4 \times 4, 5 \times 5, 6 \times 6, 8 \times 8\}$. For low field strengths ($B_0 \leqslant 3$T), divergence-free current patterns reach more than 90% of the ultimate intrinsic SNR at both voxel positions and all acceleration factors. For ultra-high field strength $\geqslant 7$ T such general statements no longer hold true: Keeping $\rho \leqslant 4x4$, the contribution of divergence-free current patterns to the ultimate intrinsic SNR at the center is higher than at the intermediate voxel position. As a consequence, adding curl-free current patterns to the divergence-free current patterns increases SNR substantially for all intermediate positions of the xz/yz-plane between the very periphery and the center of the spherical head model.

Figure 6 displays the power losses originating from divergence-free and curl-free current patterns as the diagonal entries of the noise
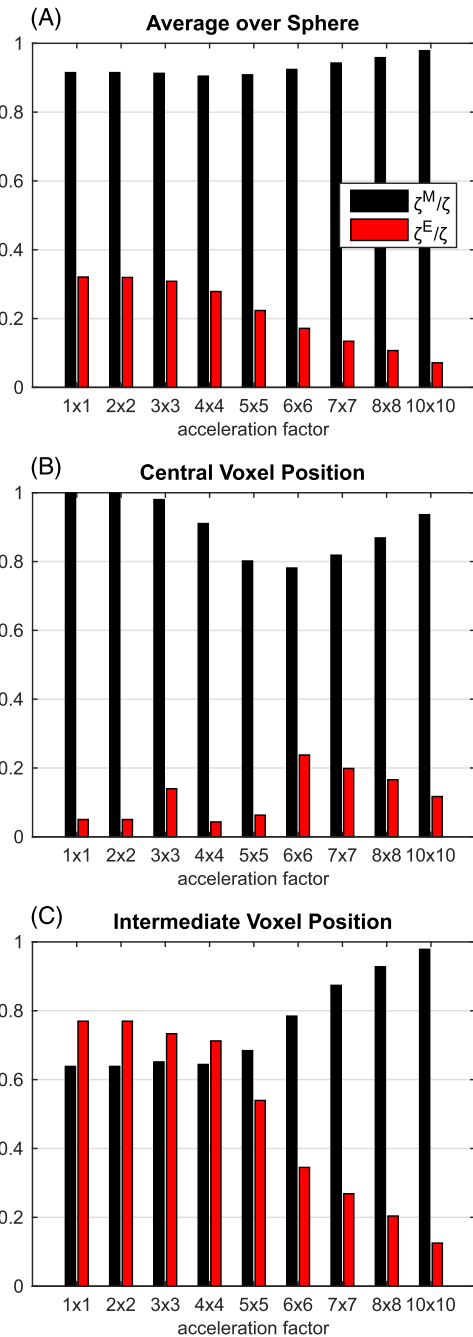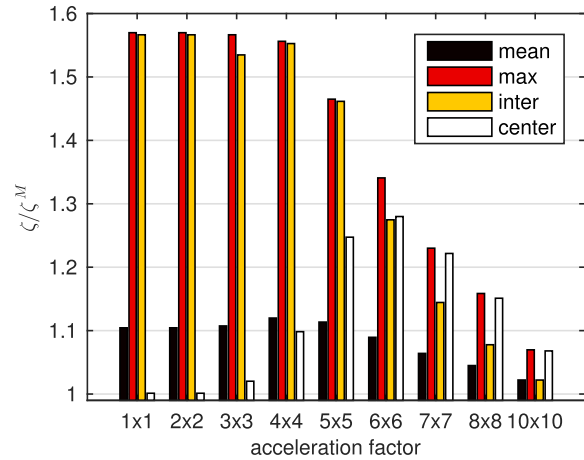
(A) **Average over Sphere**

(B) **Central Voxel Position**

(C) **Intermediate Voxel Position**

FIGURE 3 The bar charts show the (normalized) achievable ultimate intrinsic SNR with having only divergence-free current patterns (ζ^M/ζ) or only curl-free current patterns (ζ^E/ζ) as a basis set. The total ultimate intrinsic SNR ζ is obtained from a complete basis set of divergence-free and curl-free current patterns. Subfigure A, shows the average value of the ratios over the entire sphere. Moreover, we investigated the ratios for two distinct voxel positions: B, at a central voxel (s. "+" in Figure 2) and in C, at an intermediate voxel located about 4.4 cm in z-direction above the central voxel (s. "o" in Figure 2)

FIGURE 4 The bar chart shows the enhancement in SNR obtained by a combination of curl-free and divergence-free current patterns over divergence-free current patterns alone as the term ζ/ζ^M. By ζ^M, we mean the ultimate intrinsic SNR obtained when only divergence-free (magnetic-type) current patterns are used as a basis set. The total ultimate intrinsic SNR ζ is obtained from a complete basis set of divergence-free and curl-free current patterns. The black bars illustrate the SNR enhancement averaged over all voxels within the spherical volume ("head" region). The red bars summarize the maximal SNR gain appearing in the sphere. Moreover, the ratio ζ/ζ^M is investigated for two distinct voxel positions: The white bars characterize the SNR enhancement at a central voxel (s. "+" in Figure 2) whereas the yellow bars show the SNR gain at an intermediate voxel located about 4.4 cm in z-direction above the central voxel (s. "o" in Figure 2)

covariance matrix from Equation (24). With the chosen material and boundary parameters, the losses caused by the divergence-free

current are slightly higher for up to and including the fourth degree terms but substantially lower for all other higher degree terms. However, the ratio of the power losses caused by curl-free to divergence-free current patterns increases more than quadratically with the expansion order for $l \gg 4$. The ultimate intrinsic SNR depends on the receive sensitivities of the fundamental current modes of divergence-free (magnetic-type) and curl-free (electric-type) vector spherical harmonics (s. Equations (19) and (20)). We illustrate the spatial behavior of the magnetic- and electric-receive sensitivities up to the fourth degree in Figure 7. It is noticeable that the sensitivity with the highest signal strength originates from a divergence-free current distribution with $l = m = 1$. This is the only harmonic that has a nonzero value at the center. On the z-axis, the only harmonics contributing to receive sensitivity are the terms of order $m = 1$.

To validate our results with the literature and to investigate how ideal current patterns depend on position and acceleration factor, we plot ideal current patterns for maximal SNR at two exemplary voxel positions and acceleration factors in Figure 8. All plots show the ideal current patterns for the time instant zero and are only a snapshot of the time harmonic current patterns. Animated current patterns, which illustrate time-harmonic behavior, are available online in Supporting Videos S1-S4. Comparison of our results for the central voxel with previous work done by Lattanzi[20] shows good agreement. Moreover, for the first time we provide ideal current patterns when parallel imaging
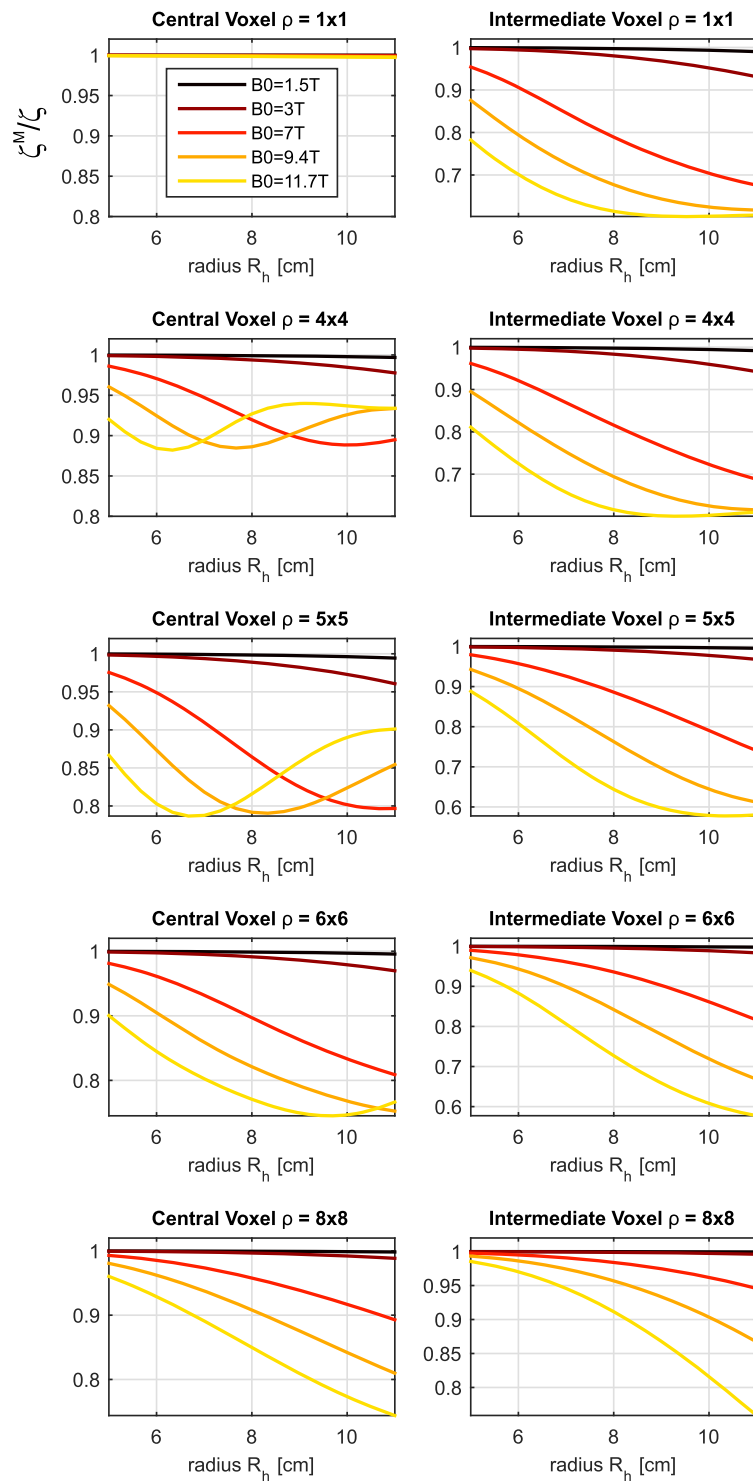
FIGURE 5 The contribution of divergence-free current patterns to the ultimate intrinsic SNR is plotted as the ratio ζ^M/ζ for two distinct voxel positions: The first voxel is located in the center and the second one at an intermediate position (s. Figure 2). We varied the radius of the sphere modeling the human head between 5 and 11 cm. We show the results for several magnetic field strengths B_0 and acceleration factors ρ

is present using an acceleration factor of 4×4 in x- and y-direction. For both target voxels, the ideal current patterns are concentrated on four positions on the spherical surface. Finally, we plot ultimate g-factors for

9.4 T in Figure 9. The transition from acceleration factors between 4×4 and 5×5 marks the upper bound of the regime of practically applicable parallel imaging.
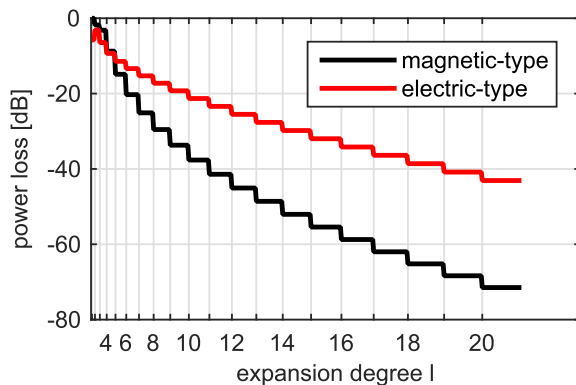
FIGURE 6 Power loss spectra originating from divergence-free (magnetic-type) and curl-free (electric-type) current patterns as the diagonal entries of the noise covariance matrix of Equation (24). All values are normalized to the maximum loss Ψ_{max} occurring for the magnetic-type with $l=1$, $m=0$ and plotted in logarithmic scale as $10 \log_{10}(\Psi_{l,m}/\Psi_{max})$

5 | DISCUSSION

To summarize our results, we found the following ultimate SNR trends:

- A complete basis set of surface current patterns, exciting all possible electromagnetic modes in a spherical sample, needs to have both, curl-free and divergence-free patterns.
- At low field ($B_0 \leqslant 3$ T), divergence-free patterns are the major contributor to the ultimate intrinsic SNR.
- At ultra-high field ($B_0 \geqslant 7$ T) and reasonable acceleration ($\rho \leqslant 4 \times 4$) a combination of divergence-free and curl-free patterns is required to reach the ultimate intrinsic SNR in all regions of a spherical model.

5.1 | Practical Guidelines for RF Coil Design

Based on our results, we deduce the following guidelines for RF coil design regarding head applications. On 1.5T and 3T platforms the use of traditional loop-only receive arrays, which correspond to divergence-free current patterns, is sufficient to cover more than 90% of the ultimate intrinsic SNR in a spherical sample of the size of the human head. When approaching field strengths of 7 T and above, we suggest a combination of divergence-free and curl-free current patterns to reach the ultimate intrinsic SNR in all regions of the human head. To realize a combination of divergence-free and curl-free current patterns, loops and electric dipoles can be used together in a receive array. At this point, it needs to be emphasized, that straight, z-directed dipoles are a mixture of both divergence-free and curl-free current patterns.[33] Thus, for specific voxel positions (such as the central voxels in a cylinder) electric dipoles might yield higher SNR than curl-free current patterns alone,[33,34] but in general, electric dipoles do not create a complete basis set. Therefore a combination of loops and dipoles is necessary to achieve the ultimate intrinsic SNR at any voxel position in the human head at ultra-high field strength.

Experimental investigations of SNR enhancement by combining loops and dipoles were done in human body applications. At 7 T,

Wiggins demonstrated a central SNR increase of 22% by a sixteen channel array as a combination of loops and dipoles compared to an eight channel loop-only array[35] for a cylindrical setup of human torso dimensions. The author drew the conclusion that the SNR increase was not due to a higher number of receive elements, as simulation results provided an SNR boost of only 1.2% when going from eight to sixteen loop elements. Wiggins' conclusion is supported by several works investigating the SNR in dependence of the number of loop elements.[36-39] Ertürk et al. showed that at 7 T a combination of loops and dipoles improved SNR and transmit efficiency in the prostate compared to a microstrip array and a fractionated dipole array.[40] For specific voxel positions, dipole-only arrays could be a good choice: Chen showed for example, that an array of dense dipoles approaches the ultimate intrinsic SNR at 7 T in the center of a cylinder of human head dimensions.[34] However, this does not mean, that dipoles perform generally superior than loop coils at ultra-high field strength. Figure 2 demonstrates, that within large areas of the spherical model, only divergence-free current patterns perform much better than only curl-free current patterns. The main limitation of using dipole elements in head imaging is their rather impractical length. Various techniques were discussed to shorten the length of $\lambda/2$ dipoles, inter alia using dielectric substrates[41,42] or reactive elements.[43-45] Besides using dipoles, there are other promising ideas on how to practically implement structures exciting curl-free current patterns, such as vertical coil elements[46-48] or loops with nonuniform current distribution.[49] If ideal current patterns are used as a design guideline, one needs to be aware of their time-harmonic dependence and it needs to be emphasized that they are only ideal for one specific position and acceleration factor.

5.2 | Influence of Boundary Conditions

The dyadic Green's function formalism incorporates the boundary conditions imposed by the RF shield and the transition from the dielectric sample to vacuum. Thereby, the question arises, do we constrain the solution space of the optimization problem by imposing boundary conditions? Wiesinger has already pointed out that boundary conditions (electromagnetic environment outside the sample) do not constrain the solution space inside the sample.[18] He used arguments from inverse source identification.[50] In the appendix, we give an alternative proof based on the diagonal form of the noise covariance matrix (Equations (A35)–(A42)). As a consequence the ultimate intrinsic SNR in the herein presented spherical setup does not change in the presence of any shield (no matter what conductivity it has). Moreover, calculating the ultimate intrinsic SNR in a spherical geometry by either a multipole expansion or with the framework of dyadic Green's functions, yields (apart from a constant scaling factor) exactly the same results (s. Equation (A42)). The main advantage of using a basis set of surface current distributions is that we have access to ideal current patterns and are able to separate divergence-free and curl-free current patterns, which is the major subject of this work.

5.3 | Mechanisms Behind the Contribution of Curl-Free Current Patterns

Based on Equation (32), we can interpret the contribution of curl-free current patterns to the ultimate intrinsic SNR without acceleration.
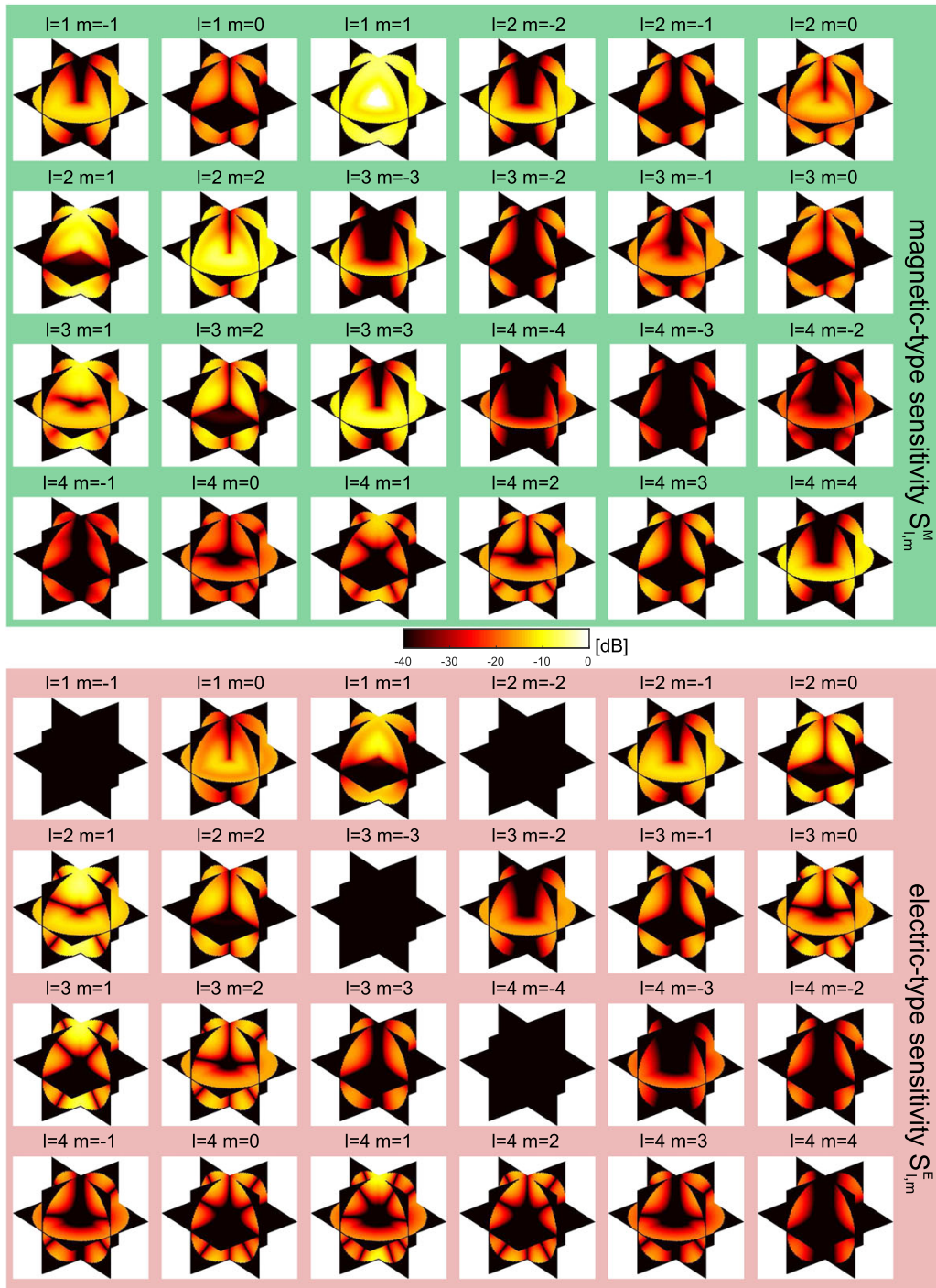
FIGURE 7 Absolute value of the magnetic- and electric-type receive sensitivities associated for a divergence-free and curl-free surface current distribution according to Equations (19) and (20). We normalized all values to the maximum absolute value occurring for the magnetic-type at $l=1$ and $m=1$ and plotted this ratio in logarithmic scale as $20\log_{10}(S(\mathbf{r})/S_{max})$. The absolute value is rotationally symmetric about the z-axis

For the center, the ultimate intrinsic SNR is mainly dominated by divergence-free currents, and additional curl-free current patterns have very little effect on SNR. This is because the magnetic sensitivity with the index $l = m = 1$ is the only harmonic that has nonvanishing signal at the center (Figure 7). Regarding the intermediate region, curl-free harmonics of lower degree have substantial signal strength and additionally have up to $l = 4$ lower power losses compared to the divergence-free harmonics. This results in a high signal-to-noise ratio of curl-free current patterns at this position. The higher the degree of the vector harmonics **M** and **N**, the more their maxima shift to the periphery
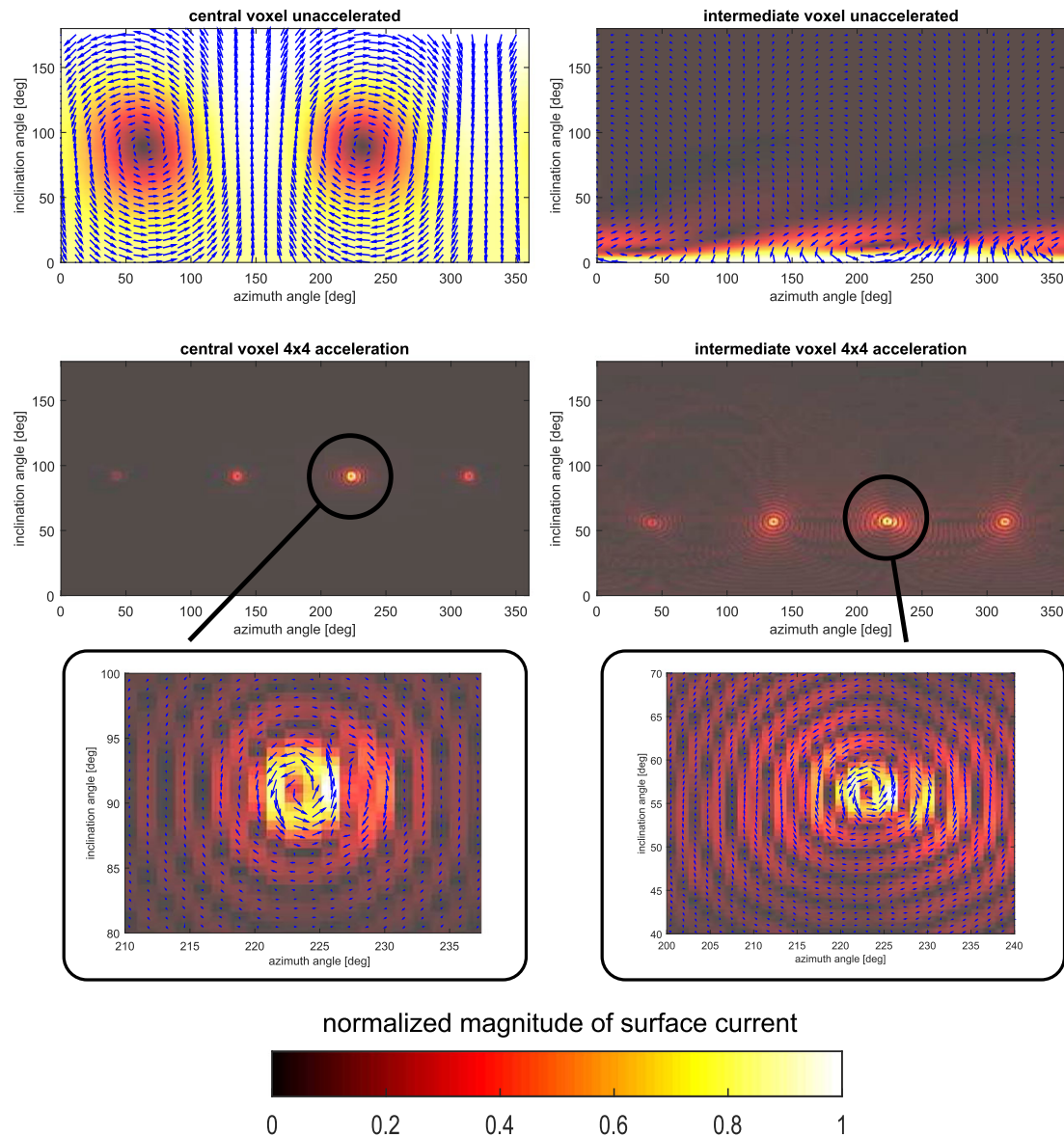
FIGURE 8 Ideal current patterns yielding maximal SNR for a central and intermediate voxel position (4.4 cm in z-direction above the central voxel). The position of the voxels is also indicated in Figure 2. The colormap shows the normalized (to maximum) magnitude of the surface current density $|\mathbf{J}| = (J_\vartheta^2 + J_\varphi^2)^{0.5}$. In the first row no parallel imaging was applied. The second row illustrates ideal current patterns when parallel imaging is present with an acceleration factor of 4×4 in x- and y-direction. Due to very tiny arrows, we present a detail of the accelerated patterns in the third row. All plots show the ideal current patterns for the time instant zero and are only a snapshot of the time variant current patterns. Animated current patterns are available online in Supporting Videos S1–S4

of the sphere. Therefore, to calculate ζ of a voxel close to the sphere's surface, higher degree spherical harmonics must be considered in the summation. For higher degree terms, the curl-free currents' losses are higher than the divergence-free ones. Due to this and the substantial receive sensitivity of higher degree curl-free and divergence-free currents at peripheral voxel positions, peripheral ultimate intrinsic SNR is mostly dominated by the divergence-free currents.

The contribution of the curl-free current to the ultimate intrinsic SNR depends on the acceleration factor. By increasing the acceleration factor, the desired nulls of the net sensitivity at the aliased voxel positions get closer to each other and to the target voxel. As a consequence, the net sensitivity needs to provide high spatial variation. High spatial variation of a net coil[18] can be achieved by higher degree vector spherical harmonics and, moreover, by complementary receive sensitivity profiles (such as produced by curl-free and divergence-free current patterns). The higher the acceleration factor, the more vector spherical harmonics contribute to the overall power loss. This is a general result independent of voxel position. The relative weighting of the magnetic- and electric-type receive sensitivities required to fulfill the weak SENSE constraint depends on the power loss associated with this
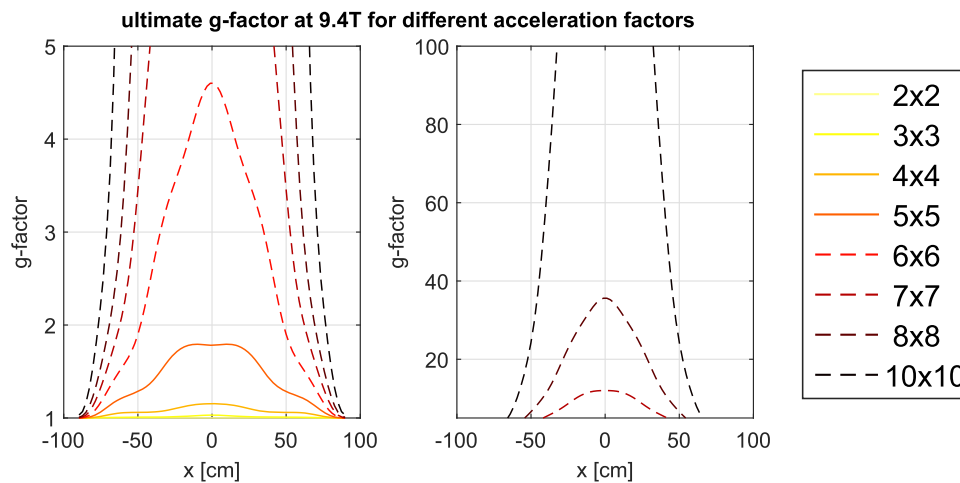
FIGURE 9 For the default setup, the g-factor along the x-axis is plotted with different 2D acceleration factors at a field strength of 9.4 T. The right and left figures have different scaling to depict the large dynamic range of the g-factor

weighting. The relative weighting that generates minimum power loss will be the optimal solution.

5.4 | Realistic Body Models

All our results are derived from a simple spherical model that is analytically manageable. This allows us to work with a basis set that is known to be complete. As the human head is not a homogeneous dielectric sphere our results do not yield the real ultimate intrinsic SNR in a quantitative way. Nevertheless, we believe that our model could be helpful to qualitatively investigate general trends that may hold true in vivo. In future work, the spherical model needs to be replaced by a realistic human head model. Recently, we tried to overcome this limitation and gave preliminary results regarding the contribution of divergence-free current patterns in a realistic head model at 9.4 T.[51] Unfortunately, in this approach the surface current is running on a closed spherical surface, which is an unrealistic situation, as in reality at least one opening for the neck is needed. More research needs to be done to take realistic current distributions under consideration. With the method applied by Guerin et al,[22,52] it is possible to study the impact of electric and magnetic dipole elements on the ultimate SNR in realistic body models. Even though such an approach does not allow investigation of curl-free and divergence-free current contributions to the ultimate intrinsic SNR, it would still be interesting to study the impact of magnetic and electric dipoles on the ultimate SNR.

REFERENCES

1. Adriany G, Van de Moortele P-F, Wiesinger F, et al. Transmit and receive transmission line arrays for 7 Tesla parallel imaging. *Magn Reson Med*. 2005;53(2): 434–445.

2. Adriany G, Van de Moortele P-F, Ritter J, et al. A geometrically adjustable 16-channel transmit/receive transmission line array for improved rf efficiency and parallel imaging performance at 7 Tesla. *Magn Reson Med*. 2008;59(3): 590–597.

3. Brunner DO, De Zanche N, Fröhlich Jürg, Paska J, Pruessmann KP. Travelling-wave nuclear magnetic resonance. *Nature*. 2009;457(7232): 994–998.

4. Brunner DO, Paška J, Froehlich J, Pruessmann KP. Traveling-wave RF shimming and parallel MRI. *Magn Reson Med*. 2011;66(1): 290–300.

5. Aussenhofer SA, Webb AG. An eight-channel transmit/receive array of TE01 mode high permittivity ceramic resonators for human imaging at 7 T. *J Magn Reson*. 2014;243: 122–129.

6. Avdievich NI. Transceiver-phased arrays for human brain studies at 7 T. *Appl Magn Reson*. 2011;41(2): 483–506.

7. Avdievich NI, Giapitzakis IA, Henning A. Novel splittable N-TX/2N-RX transceiver phased array to optimize both signal-to-noise ratio and transmit efficiency at 9.4T. *Magn Reson Med*. 2015;76:1621–1628. doi: 10.1002/mrm.26051

8. Shajan G, Kozlov M, Hoffmann J, Turner R, Scheffler K, Pohmann R. A 16-channel dual-row transmit array in combination with a 31-element receive array for human brain imaging at 9.4 T. *Magn Reson Med*. 2014;71(2): 870–879.

9. Edelstein WA, Bottomley PA, Pfeifer LM. A signal-to-noise calibration procedure for NMR imaging systems. *Med Phys*. 1984;11(2): 180–185.

10. Edelstein WA, Glover GH, Hardy CJ, Redington RW. The intrinsic signal-to-noise ratio in NMR imaging. *Magn Reson Med*. 1986;3(4): 604–618.

11. Ocali O, Atalar E. Ultimate intrinsic signal-to-noise ratio in MRI. *Magn Reson Med*. 1998;39: 462–473.

12. Roemer PB, Edelstein WA. Ultimate sensitivity limit of surface coils. *Proceedings of the 6th Annual Meeting of SMRM*, New York, USA; 1987:410.

13. Wang J, Reykowski A, Dickas J. Calculation of the signal-to-noise ratio for simple surface coils and arrays of coils. *IEEE Trans Biomed Eng*. 1995;42(9): 908–917.

14. Sodickson DK, Manning WJ. Simultaneous acquisition of spatial harmonics (SMASH): Fast imaging with radiofrequency coil arrays. *Magn Reson Med*. 1997;38(4): 591–603.

15. Pruessmann KP, Weiger M, Scheidegger MB, Boesiger P. Sense: Sensitivity encoding for fast MRI. *Magn Reson Med*. 1999;42(5): 952–962.

16. Griswold MA, Jakob PM, Heidemann RM, et al. Generalized autocalibrating partially parallel acquisitions (GRAPPA). *Magn Reson Med*. 2002;47(6): 1202–1210.

17. Ohliger MA, Grant AK, Sodickson DK. Ultimate intrinsic signal-to-noise ratio for parallel MRI: electromagnetic field considerations. *Magn Reson Med*. 2003;50(5): 1018–1030.

18. Wiesinger F, Boesiger P, Pruessmann KP. Electrodynamics and ultimate snr in parallel MR imaging. *Magn Reson Med*. 2004;52(2): 376–390.

19. Schnell W, Renz W, Vester M, Ermert H. Ultimate signal-to-noise-ratio of surface and body antennas for magnetic resonance imaging. *IEEE Trans Antennas Propag*. 2000;48(3): 418–428.

20. Lattanzi R, Sodickson DK. Ideal current patterns yielding optimal signal-to-noise ratio and specific absorption rate in magnetic resonance imaging: computational methods and physical insights. *Magn Reson Med*. 2012;68(1): 286–304.

21. Felder J, Shah NJ. Ultimate intrinsic signal-to-noise ratio of the human head at 9.4T. *Proceedings of the 19th Annual Meeting of ISMRM*, Montréal, Canada; 2011:3878.

22. Guerin B, Villena JF, Polimeridis AG, et al. The ultimate SNR and SAR in realistic body models. *Proceedings of the 22nd Annual Meeting of ISMRM*, Milan, Italy; 2014:617.

23. Lattanzi R, Grant AK, Polimeni JR, et al. Performance evaluation of a 32-element head array with respect to the ultimate intrinsic SNR. *NMR Biomed*. 2010;23(2): 142–151.

24. Hoult DI. The principle of reciprocity in signal strength calculations- a mathematical guide. *Concepts Magn Reson*. 2000;12(4): 173–187.

25. Roemer PB, Edelstein WA, Hayes CE, Souza SP, Mueller OM. The NMR phased array. *Magn Reson Med*. 1990;16(2): 192–225.

26. Hayes CE, Roemer PB. Noise correlations in data simultaneously acquired from multiple surface coil arrays. *Magn Reson Med*. 1990;16(2): 181–191.

27. Stratton JA. *Electromagnetic Theory*. New York and London: McGraw-Hill; 1941.

28. Sarkar D, Halas NJ. General vector basis function solution of maxwell's equations. *Phys Rev E*. 1997;56: 1102–1112.

29. Jackson JD. *Classical Electrodynamics*. New York: John Wiley & Sons; 1999.

30. Tai CT. *Dyadic Green Functions in Electromagnetic Theory*. New York: IEEE Press Series on Electromagnetic Waves; 1994.

31. Li LW, Kooi PS, Leong MS, Yeo TS. Electromagnetic dyadic green's function in spherically multilayered media. *IEEE Trans Microw Theory Techn*. 1994;42(12): 2302–2310.

32. Gabriel S, Lau RW, Gabriel C. The dielectric properties of biological tissues: Iii. parametric models for the dielectric spectrum of tissues. *Phys Med Biol*. 1996;41: 2271–2293.

33. Sodickson DK, Wiggins GC, Chen G, Lakshmanan K, Lattanzi R. More than meets the eye: The mixed character of electric dipole coils, and implications for high-field performance. *Proceedings of the 24th Annual Meeting of ISMRM*, Singapore, Singapore; 2016:389.

34. Chen G, Lattanzi R, Sodickson D, Wiggins G. Approaching the ultimate intrinsic SNR with dense arrays of electric dipole antennas. *Proceedings of the 24th Annual Meeting of ISMRM*, Singapore, Singapore; 2016:168.

35. Wiggins GC, Zhang B, Cloos M, et al. Mixing loops and electric dipole antennas for increased sensitivity at 7 Tesla. *Proceedings of the 21st Annual Meeting of ISMRM*, Salt Lake City, Utah, USA; 2013:2737.

36. Lattanzi R, Grant AK, Sodickson DK. Approaching ultimate SNR and ideal current patterns with finite surface coil arrays on a dielectric cylinder. *Proceedings of the 16th Annual Meeting of ISMRM*, Toronto, Canada; 2008:1074.

37. Vaidya MV, Sodickson DK, Lattanzi R. Approaching ultimate intrinsic SNR in a uniform spherical sample with finite arrays of loop coils. *Concepts Magn Reson Part B*. 2015;44B(3): 53–65.

38. Keil B, Wald LL. Massively parallel MRI detector arrays. *J Magn Reson*. 2013;229: 75–89.

39. Hardy CJ, Giaquinto RO, Piel JE, et al. 128-channel body MRI with a flexible high-density receiver-coil array. *J Magn Reson*. 2008;28: 1219–1225.

40. Ertürk MA, Raaijmakers AJE, Adriany G, Uğurbil K, Metzger GJ. A 16-channel combined loop-dipole transceiver array for 7 Tesla body MRI. *Magn Reson Med*. 2016. doi:10.1002/mrm.26153

41. Raaijmakers AJE, Ipek O, Klomp DWJ, Possanzini C, Harvey PR, Lagendijk JJW, van den Berg CAT, et al. Design of a radiative surface coil array element at 7 T: The single-side adapted dipole antenna. *Magn Reson Med*. 2011;66(5): 1488–1497.

42. Winter L, Özerdem C, Hoffmann W, et al. Design and evaluation of a hybrid radiofrequency applicator for magnetic resonance imaging and RF induced hyperthermia: Electromagnetic field simulations up to 14.0 Tesla and proof-of-concept at 7.0 Tesla PLOS ONE. 8:e61661. 2013.

43. Wiggins GC, Zhang B, Lattanzi R, Chen G, Sodickson D. The electric dipole array: an attempt to match the ideal current pattern for central SNR at 7 Tesla. *Proceedings of the 20th Annual Meeting of ISMRM*, Melbourne, Australia; 2012:541.

44. Raaijmakers AJE, Italiaander M, Voogt IJ, et al. The fractionated dipole antenna: A new antenna for body imaging at 7 Tesla. *Magn Reson Med*. 2016;75: 1366–1374.

45. Steensma B, Andrade AVO, Klomp D, van den Berg N, Luijten P, Raaijmakers A. Body imaging at 7 Tesla with much lower sar levels: An introduction of the snake antenna array. *Proceedings of the 24th Annual Meeting of ISMRM*, Singapore, Singapore; 2016:395.

46. Wang ZJ. Towards a complete coil array. *MRI*. 2008;26: 1310–1315.

47. Wang ZJ. Improving SNR of RF coils using composite coil elements. *NMR Biomed*. 2009;22: 952–959.

48. Maunder A, Fallone BG, Daneshmand M, De Zanche N. Experimental verification of snr and parallel imaging improvements using composite arrays. *NMR Biomed*. 2015;28(2): 141–153.

49. Lakshmanan K, Cloos M, Lattanzi R, Sodickson D, Wiggins G. The loopole antenna: capturing magnetic and electric dipole fields with a single structure to improve transmit and receive performance. *Proceedings of the 22nd Annual Meeting of ISMRM*, Milan, Italy; 2014:397.

50. Bleistein N, Cohen JK. Nonuniqueness in the inverse source problem in acoustics and electromagnetics. *J Math Phys*. 1977;18(2): 194–201.

51. Pfrommer A, Henning A. About the ultimate SNR for cylindrical and spherical RF arrays in a realistic human head model. *Proceedings of the 24th Annual Meeting of ISMRM*, Singapore, Singapore; 2016:175.

52. Guerin B, Villena JF, Polimeridis AG, et al. Ultimate hyperthermia: Computation of the best achievable radio-frequency hyperthermia treatments in non-uniform body models. *Proceedings of the 24th Annual Meeting of ISMRM*, Singapore, Singapore; 2016:351.

SUPPORTING INFORMATION

Additional Supporting Information may be found online in the supporting information tab for this article.

APPENDIX

Mathematical Notation

Vectors and matrices are printed in bold and dyads are additionally indicated with a bar. For the Hermitian transpose of a matrix $\mathbf{A}$, we write $\mathbf{A}^H$. Complex conjugation of a variable x is symbolized by x^*.

Vector spherical harmonics

The vector spherical harmonic $\mathbf{X}_{l,m}(\vartheta,\varphi)$ of degree l and order m is defined according to Equation (9.119) in Jackson[29]:

$$\mathbf{X}_{l,m}(\vartheta,\varphi) = \frac{-i}{\sqrt{l(l+1)}}\mathbf{r}\times\nabla Y_{l,m}(\vartheta,\varphi) \tag{A1}$$

$$Y_{l,m}(\vartheta,\varphi) = \sqrt{\frac{(2l+1)}{4\pi}\frac{(l-m)!}{(l+m)!}}P_l^m(\cos\vartheta)e^{im\varphi} \tag{A2}$$

$$P_l^m(x) = \frac{(-1)^m}{2^l l!}\left(1-x^2\right)^{m/2}\frac{d^{l+m}}{dx^{l+m}}\left(x^2-1\right)^l \qquad x\in\mathbb{R};\ |x|\leqslant 1 \tag{A3}$$

Dyadic Green's functions

The electric-type dyadic Green's functions $\bar{\mathbf{G}}_e^{22}$ (field in layer 2, source in layer 2) and $\bar{\mathbf{G}}_e^{32}$ (field in layer 3, source in layer 2) for a three-layered setup at field point $\mathbf{r}$ and with the source located at $\mathbf{r}'$ is given in Li et al.[31] To account for boundary conditions when the propagation constant changes between layer three and two, the boundary coefficients $C_{M,N}^{32}$, $D_{M,N}^{32}$, $A_{M,N}^{22}$, $B_{M,N}^{22}$, $C_{M,N}^{22}$ and $D_{M,N}^{22}$ were added:

$$\begin{aligned}\bar{\mathbf{G}}_e^{32}(\mathbf{r},\mathbf{r}') = ik_0\sum_{l=1}^{\infty}\sum_{m=-l}^{l}&\mathbf{M}_{l,m}(k,\mathbf{r})\left[C_M^{32}\mathbf{M}'_{l,m}(k_0,\mathbf{r}')+D_M^{32}\mathbf{M}'^{(1)}_{l,m}(k_0,\mathbf{r}')\right]\\&+\mathbf{N}_{l,m}(k,\mathbf{r})\left[C_N^{32}\mathbf{N}'_{l,m}(k_0,\mathbf{r}')+D_N^{32}\mathbf{N}'^{(1)}_{l,m}(k_0,\mathbf{r}')\right]\end{aligned} \tag{A4}$$

$$\begin{aligned}\bar{\mathbf{G}}_e^{22}(\mathbf{r},\mathbf{r}') = &\bar{\mathbf{G}}_{e0}(\mathbf{r},\mathbf{r}')\\&+ik_0\sum_{l=1}^{\infty}\sum_{m=-l}^{l}\mathbf{M}^{(1)}_{l,m}(k_0,\mathbf{r})\left[A_M^{22}\mathbf{M}'_{l,m}(k_0,\mathbf{r}')+B_M^{22}\mathbf{M}'^{(1)}_{l,m}(k_0,\mathbf{r}')\right]\\&+\mathbf{N}^{(1)}_{l,m}(k_0,\mathbf{r})\left[A_N^{22}\mathbf{N}'_{l,m}(k_0,\mathbf{r}')+B_N^{22}\mathbf{N}'^{(1)}_{l,m}(k_0,\mathbf{r}')\right]\\&+\mathbf{M}_{l,m}(k_0,\mathbf{r})\left[C_M^{22}\mathbf{M}'_{l,m}(k_0,\mathbf{r}')+D_M^{22}\mathbf{M}'^{(1)}_{l,m}(k_0,\mathbf{r}')\right]\\&+\mathbf{N}_{l,m}(k_0,\mathbf{r})\left[C_N^{22}\mathbf{N}'_{l,m}(k_0,\mathbf{r}')+D_N^{22}\mathbf{N}'^{(1)}_{l,m}(k_0,\mathbf{r}')\right]\end{aligned} \tag{A5}$$

$$\begin{aligned}\bar{\mathbf{G}}_{e0}(\mathbf{r},\mathbf{r}') = ik_0\sum_{l=1}^{\infty}\sum_{m=-l}^{l}&\mathbf{M}_{l,m}(k_0,\mathbf{r})\mathbf{M}'^{(1)}_{l,m}(k_0,\mathbf{r}')\\&+\mathbf{N}_{l,m}(k_0,\mathbf{r})\mathbf{N}'^{(1)}_{l,m}(k_0,\mathbf{r}') \qquad r<r'\end{aligned} \tag{A6}$$

The term $\bar{\mathbf{G}}_{e0}$ is the free-space Green's function (without the singular term) and for the primed vector wave functions the following definition holds:

$$\mathbf{M}'_{l,m} = j_l(kr)\mathbf{X}^*_{l,m} \tag{A7}$$

$$\mathbf{N}'_{l,m} = \frac{1}{k}\nabla\times\mathbf{M}'_{l,m} \tag{A8}$$

If the vector wave functions $\mathbf{M}^{(1)}_{l,m}$ or $\mathbf{N}^{(1)}_{l,m}$ are used, the function $j_l(kr)$ has to be replaced by $h_l^{(1)}(kr)$.

Orthogonality relations

$$\int_{r=0}^{R_c}\iint_{\Omega}\mathbf{M}'_{l,m}\cdot\mathbf{X}_{l',m'}\delta(r-R_c)r^2\,d\Omega dr = R_c^2 j_l(kR_c)\delta_{ll'}\delta_{mm'} \tag{A9}$$

$$\int_{r=0}^{R_c}\iint_{\Omega}\mathbf{N}'_{l,m}\cdot\hat{\mathbf{r}}\times\mathbf{X}_{l',m'}\delta(r-R_c)r^2\,d\Omega dr = \frac{R_c}{k}\frac{\partial}{\partial r}(rj_l(kr))\bigg|_{r=R_c}\delta_{ll'}\delta_{mm'} \tag{A10}$$

$$\int_{r=0}^{R_c}\iint_{\Omega}\mathbf{M}'_{l,m}\cdot\hat{\mathbf{r}}\times\mathbf{X}_{l',m'}\delta(r-R_c)r^2\,d\Omega dr = 0 \tag{A11}$$

$$\int_{r=0}^{R_c}\iint_{\Omega}\mathbf{N}'_{l,m}\cdot\mathbf{X}_{l',m'}\delta(r-R_c)r^2\,d\Omega dr = 0 \tag{A12}$$

$$\int_{r=0}^{R_h}\iint_{\Omega}\mathbf{M}_{l,m}\cdot\mathbf{N}^*_{l',m'}r^2\,d\Omega dr = 0 \tag{A13}$$

$$\int_{r=0}^{R_h}\iint_{\Omega}\mathbf{M}_{l,m}\cdot\mathbf{M}^*_{l',m'}r^2\,d\Omega dr = \int_{r=0}^{R_h}|j_l(kr)|^2r^2\,dr\,\delta_{ll'}\delta_{mm'} \tag{A14}$$

$$\begin{aligned}\int_{r=0}^{R_h}\iint_{\Omega}\mathbf{N}_{l,m}\cdot\mathbf{N}^*_{l',m'}r^2\,d\Omega dr = &\frac{1}{|k^2|}\int_{r=0}^{R_h}l(l+1)|j_l(kr)|^2\\&+\left|\frac{\partial}{\partial r}(rj_l(kr))\right|^2\,dr\,\delta_{ll'}\delta_{mm'}\end{aligned} \tag{A15}$$

Boundary Coefficients

For the electric-type of dyadic Green's function, the following boundary conditions at the spherical interfaces hold:

$$\hat{\mathbf{r}}\times\bar{\mathbf{G}}_e^{(22)}\Big|_{r=R_1} = \bar{\mathbf{0}} \tag{A16}$$

$$\hat{\mathbf{r}}\times\bar{\mathbf{G}}_e^{(22)}\Big|_{r=R_2} = \hat{\mathbf{r}}\times\bar{\mathbf{G}}_e^{(32)}\Big|_{r=R_2} \tag{A17}$$

$$\hat{\mathbf{r}}\times\nabla\times\bar{\mathbf{G}}_e^{(22)}\Big|_{r=R_2} = \hat{\mathbf{r}}\times\nabla\times\bar{\mathbf{G}}_e^{(32)}\Big|_{r=R_2} \tag{A18}$$

This system can be solved and we get the following results:

$$A_M^{22} = \frac{\hbar_{21}(\partial j_{22}j_{32}-\partial j_{32}j_{22})}{\partial j_{32}(\hbar_{21}j_{22}-\hbar_{22}j_{21})+j_{32}(\partial\hbar_{22}j_{21}-\partial j_{22}\hbar_{21})} \tag{A19}$$

$$B_M^{22} = \frac{j_{21}(\partial j_{32}j_{22}-\partial j_{22}j_{32})}{\partial j_{32}(\hbar_{21}j_{22}-\hbar_{22}j_{21})+j_{32}(\partial\hbar_{22}j_{21}-\partial j_{22}\hbar_{21})} \tag{A20}$$

$$A_N^{22} = \frac{\partial\hbar_{21}(\partial j_{32}j_{22}k_2^2-\partial j_{22}j_{32}k_3^2)}{\partial j_{32}k_2^2(\partial j_{21}\hbar_{22}-\partial\hbar_{21}j_{22})+j_{32}k_3^2(\partial\hbar_{21}\partial j_{22}-\partial\hbar_{22}\partial j_{21})} \tag{A21}$$

$$B_N^{22} = \frac{\partial j_{21}(\partial j_{22}j_{32}k_3^2-\partial j_{32}j_{22}k_2^2)}{\partial j_{32}k_2^2(\partial j_{21}\hbar_{22}-\partial\hbar_{21}j_{22})+j_{32}k_3^2(\partial\hbar_{21}\partial j_{22}-\partial\hbar_{22}\partial j_{21})} \tag{A22}$$

$$C_M^{22} = \frac{\hbar_{21}(\partial j_{32}\hbar_{22}-\partial\hbar_{22}j_{32})}{\partial j_{32}(\hbar_{21}j_{22}-\hbar_{22}j_{21})+j_{32}(\partial\hbar_{22}j_{21}-\partial j_{22}\hbar_{21})} \tag{A23}$$

$$D_M^{22} = \frac{\hbar_{21}(\partial j_{22}j_{32}-\partial j_{32}j_{22})}{\partial j_{32}(\hbar_{21}j_{22}-\hbar_{22}j_{21})+j_{32}(\partial\hbar_{22}j_{21}-\partial j_{22}\hbar_{21})} \tag{A24}$$

$$C_N^{22} = \frac{\partial\hbar_{21}(\partial j_{22}j_{32}k_3^2-\partial j_{32}\hbar_{22}k_2^2)}{\partial j_{32}k_2^2(\partial j_{21}\hbar_{22}-\partial\hbar_{21}j_{22})+j_{32}k_3^2(\partial\hbar_{21}\partial j_{22}-\partial\hbar_{22}\partial j_{21})} \tag{A25}$$

$$D_N^{22} = \frac{\partial\hbar_{21}(\partial j_{32}j_{22}k_2^2-\partial j_{22}j_{32}k_3^2)}{\partial j_{32}k_2^2(\partial j_{21}\hbar_{22}-\partial\hbar_{21}j_{22})+j_{32}k_3^2(\partial\hbar_{21}\partial j_{22}-\partial\hbar_{22}\partial j_{21})} \tag{A26}$$

$$C_M^{32} = \frac{\hbar_{21}(\partial j_{22}\hbar_{22}-\partial\hbar_{22}j_{22})}{\partial j_{32}(\hbar_{21}j_{22}-\hbar_{22}j_{21})+j_{32}(\partial\hbar_{22}j_{21}-\partial j_{22}\hbar_{21})} \tag{A27}$$

$$D_M^{32} = \frac{j_{21}(\partial\hbar_{22}j_{22}-\partial j_{22}\hbar_{22})}{\partial j_{32}(\hbar_{21}j_{22}-\hbar_{22}j_{21})+j_{32}(\partial\hbar_{22}j_{21}-\partial j_{22}\hbar_{21})} \tag{A28}$$

$$C_N^{32} = \frac{\partial\hbar_{21}k_2k_3(\partial\hbar_{22}j_{22}-\partial j_{22}\hbar_{22})}{\partial j_{32}k_2^2(\partial j_{21}\hbar_{22}-\partial\hbar_{21}j_{22})+j_{32}k_3^2(\partial\hbar_{21}\partial j_{22}-\partial\hbar_{22}\partial j_{21})} \tag{A29}$$

$$D_N^{32} = \frac{\partial j_{21}k_2k_3(\partial j_{22}\hbar_{22}-\partial\hbar_{22}j_{22})}{\partial j_{32}k_2^2(\partial j_{21}\hbar_{22}-\partial\hbar_{21}j_{22})+j_{32}k_3^2(\partial\hbar_{21}\partial j_{22}-\partial\hbar_{22}\partial j_{21})} \tag{A30}$$

In the above equations, we used the following abbreviations (where the first index refers to the propagation constant in layer u and the second to the radius at boundary number v):

$$\hbar_{uv} = h_l^{(1)}(k_uR_v) \tag{A31}$$

$$j_{uv} = j_l(k_uR_v) \tag{A32}$$

$$\partial j_{uv} = \frac{\partial(xj_l(x))}{\partial x}\bigg|_{x=k_uR_v} \tag{A33}$$

$$\partial\hbar_{uv} = \frac{\partial(xh_l^{(1)}(x))}{\partial x}\bigg|_{x=k_uR_v} \tag{A34}$$

Influence of boundary conditions on the ultimate intrinsic SNR

First, we define the receive sensitivity and the noise covariance for an electromagnetic field obtained with a multipole expansion as in Equations (10), (11):

$$\tilde{S}_{l,m}^{M}(\mathbf{r}) \propto \left(\mathbf{N}_{l,m}(\mathbf{r})\big|_x - i\,\mathbf{N}_{l,m}(\mathbf{r})\big|_y \right) \tag{A35}$$

$$\tilde{S}_{l,m}^{E}(\mathbf{r}) \propto \left(\mathbf{M}_{l,m}(\mathbf{r})\big|_x - i\,\mathbf{M}_{l,m}(\mathbf{r})\big|_y \right) \tag{A36}$$

$$\tilde{\Psi}_{(l,m),(l',m')}^{M} \propto \sigma \int_{r=0}^{R_h} |j_l(kr)|^2 r^2 \, dr \, \delta_{ll'} \delta_{mm'} \tag{A37}$$

$$\tilde{\Psi}_{(l,m),(l',m')}^{E} \propto \frac{\sigma}{|k|^2} \int_{r=0}^{R_h} \left(l(l+1)|j_l(kr)|^2 + \left| \frac{\partial}{\partial r} r j_l(kr) \right|^2 \right) dr \, \delta_{ll'} \delta_{mm'} \tag{A38}$$

In a next step, we introduce a diagonal boundary coefficient matrix $\mathbf{V}$:

$$\mathbf{V} = \begin{pmatrix} V_{1,-1}^{M} & \cdots & 0 & 0 & \cdots & 0 \\ \vdots & \ddots & \vdots & \vdots & \ddots & \vdots \\ 0 & \cdots & V_{L,L}^{M} & 0 & \cdots & 0 \\ 0 & \cdots & 0 & V_{1,-1}^{E} & \cdots & 0 \\ \vdots & \ddots & \vdots & \vdots & \ddots & \vdots \\ 0 & \cdots & 0 & 0 & \cdots & V_{L,L}^{E} \end{pmatrix} \tag{A39}$$

Now the receive sensitivity matrix and the noise covariance matrix, which are obtained from the dyadic Green's function approach of Equations (18), (24), can be rewritten as:

$$\mathbf{S} \propto \mathbf{V}\tilde{\mathbf{S}} \tag{A40}$$

$$\mathbf{\Psi} \propto \mathbf{V}^H \tilde{\mathbf{\Psi}} \mathbf{V} \tag{A41}$$

To calculate the ultimate intrinsic SNR, we have to evaluate $\mathbf{S}^H \mathbf{\Psi}^{-1} \mathbf{S}$. Using Equations (A40), (A41), we can write:

$$\begin{aligned} \mathbf{S}^H \mathbf{\Psi}^{-1} \mathbf{S} &\propto (\mathbf{V}\tilde{\mathbf{S}})^H (\mathbf{V}^H \tilde{\mathbf{\Psi}} \mathbf{V})^{-1} (\mathbf{V}\tilde{\mathbf{S}}) \\ &= \tilde{\mathbf{S}}^H \mathbf{V}^H (\mathbf{V}^H)^{-1} \tilde{\mathbf{\Psi}}^{-1} \mathbf{V}^{-1} \mathbf{V}\tilde{\mathbf{S}} \\ &= \tilde{\mathbf{S}}^H \tilde{\mathbf{\Psi}}^{-1} \tilde{\mathbf{S}} \end{aligned} \tag{A42}$$

Because of the diagonal form of the noise covariance matrix $\tilde{\mathbf{\Psi}}$, we could invert each matrix in the expression $(\mathbf{V}^H \tilde{\mathbf{\Psi}} \mathbf{V})^{-1}$ separately.

PUBLICATION 2

The ultimate intrinsic signal-to-noise ratio of loop- and dipole-like current patterns in a realistic human head model

Andreas Pfrommer[1] | **Anke Henning[1,2]**

[1] Max Planck Institute for Biological Cybernetics, High-Field Magnetic Resonance Center, Tuebingen, Germany

[2] Ernst-Moritz-Arndt University Greifswald, Institute of Physics, Greifswald, Germany

Correspondence
Andreas Pfrommer, Max Planck Institute for Biological Cybernetics, Max-Planck-Ring 11, 72076 Tuebingen, Germany.
Email: andreas.pfrommer@tuebingen.mpg.de

Purpose: The ultimate intrinsic signal-to-noise ratio (UISNR) represents an upper bound for the achievable SNR of any receive coil. To reach this threshold a complete basis set of equivalent surface currents is required. This study systematically investigated to what extent either loop- or dipole-like current patterns are able to reach the UISNR threshold in a realistic human head model between 1.5 T and 11.7 T. Based on this analysis, we derived guidelines for coil designers to choose the best array element at a given field strength. Moreover, we present ideal current patterns yielding the UISNR in a realistic body model.

Methods: We distributed generic current patterns on a cylindrical and helmet-shaped surface around a realistic human head model. We excited electromagnetic fields in the human head by using eigenfunctions of the spherical and cylindrical Helmholtz operator. The electromagnetic field problem was solved by a fast volume integral equation solver.

Results: At 7 T and above, adding curl-free current patterns to divergence-free current patterns substantially increased the SNR in the human head (locally >20%). This was true for the helmet-shaped and the cylindrical surface. On the cylindrical surface, dipole-like current patterns had high SNR performance in central regions at ultra-high field strength. The UISNR increased superlinearly with B0 in most parts of the cerebrum but only sublinearly in the periphery of the human head.

Conclusion: The combination of loop and dipole elements could enhance the SNR performance in the human head at ultra-high field strength.

KEYWORDS
dipole antenna, dyadic Green's functions, electromagnetic simulation, realistic body model, RF coils, ultimate intrinsic SNR

1 | INTRODUCTION

To maximize the signal-to-noise ratio (SNR) for human head applications at 7 T and above, new receive array designs were suggested. Recently, the electric dipole became the center of interest to boost the SNR of traditional loop-only arrays in certain applications at ultra-high fields. There were first trials with dipole-only[1–6] or combined loop-dipole[7–10]

arrays. Moreover, a combination of surface loops and vertical loops was tested.[11] From a theoretical viewpoint, the SNR of any receive array is bounded by the ultimate intrinsic SNR (UISNR).[12–14] This value describes the fundamental electrodynamic limits of MR signal reception and can be used as an absolute performance metric to select the best array configuration. In electromagnetic theory, loop-only arrays can be modeled by a divergence-free surface current distribution.
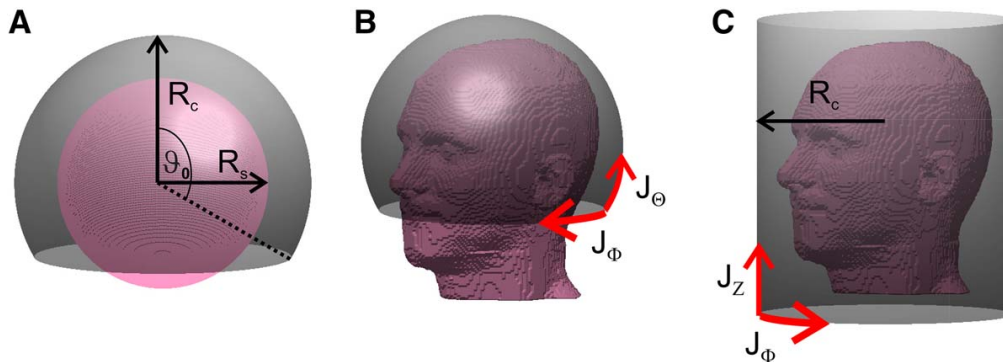
FIGURE 1 Three different setups used to investigate the best possible SNR of loop- and dipole-like surface currents relative to the UISNR: (A) A VSCH basis set is used, where curl- and divergence-free surface current patterns are running on a spherical cap with cap angle ϑ_0 and radius R_c. The UISNR is evaluated in a spherical phantom of human head-size (radius R_s). (B) A VSCH basis set is used and the UISNR is evaluated in a realistic human body model. (C) A VCH basis set is used and the UISNR is evaluated in a realistic human body model

Divergence-free current patterns must be complemented by curl-free current patterns to form a complete electromagnetic basis yielding the UISNR.[15] Straight, Z-directed dipoles positioned on a cylindrical former are characterized by a Z-directed current distribution (Figure 1C). These Z-directed current patterns need to be replenished with Φ-directed patterns to complete the basis set. Knowing the maximum achievable, theoretical SNR limit of divergence-free (loop-like) or Z-directed (dipole-like) current patterns relative to the UISNR is a direct performance measure, to what extent general loop-only or dipole-only receive arrays are able to reach the UISNR threshold.

Prior to UISNR calculation, a complete electromagnetic basis set needs to be created. Several methods have been proposed to calculate the UISNR:

1. Use a linear combination of plane waves impinging on the sample and solve the scattering problem.[14,16,17]

2. Randomly excite a large number of elementary electric and magnetic dipoles lying on a Huygen's surface and solve the Helmholtz equation.[18–20]

3. Use the analytically known eigenfunctions of the Helmholtz operator in spherical[15,21,22] or cylindrical[22,23] coordinate systems. Equivalent surface current patterns, which surround the sample, can be used to excite these eigenfunctions.

The first method was initially used in Ref. 14 and so far is implemented for UISNR calculations in (elliptical) cylinders[14,16] and realistic human body models.[17] The algorithm is relatively simple to program, but for typical spatial resolutions and field strengths the basis set becomes impractically large.[21] A decomposition into curl- and divergence-free current patterns is not possible as no equivalent surface current patterns are used. The second approach is motivated by finding a low-rank approximation of the basis set in body

models.[19,24–26] The strength of the method is that the Huygens' surface can be arbitrarily shaped. The best possible SNR of electric and magnetic dipoles relative to the UISNR can be evaluated. However, the practically more relevant SNR performance of curl- and divergence-free current patterns cannot be directly accessed. The third method is numerically very efficient and results in fast convergence, because the eigenfunctions are orthogonal (for spherical and cylindrical samples). Moreover, it is mathematically proven that the basis set is complete.[27] When combining the dyadic Green's function approach (DGF)[28] with this method, it is straightforward to separate the generic current patterns into curl- and divergence-free modes. The best possible SNR of curl- and divergence-free current patterns relative to the UISNR was briefly studied for cylinders[22,23] and spheres.[22] A rigorous analysis for a spherical head model was done in Ref. 15. The major drawback of the third method is that it cannot be applied to arbitrary coordinate systems, that is, the Huygens' surface of the current patterns cannot be arbitrarily shaped. Only coordinate systems which allow the separation of the vector Helmholtz equation are supported.[29]

This work is the first study that systematically investigates to what extent either loop- or dipole-like current patterns are able to reach the UISNR threshold in a realistic human head model. To evaluate the UISNR in a realistic head model, we use a new approach: We distribute generic surface current patterns on a cylindrical or helmet-shaped surface around the head model. These currents excite eigenfunctions of the spherical or cylindrical Helmholtz operator and a fast volume integral equation solver is used to solve the electromagnetic scattering problem. Based on our analysis we derive guidelines for coil designers to choose the best array elements at a given field strength. For the first time, we present ideal current patterns yielding the UISNR in realistic body models. Additionally, we examine the increase of the UISNR with regard to field strength B_0.

2 $\mid$ THEORY

The following section describes the mathematical background for the newly developed approach to calculate the UISNR in realistic body models. Special functions and mathematical expressions can be found in the supporting information, as well as a list of abbreviations and symbols.

2.1 $\mid$ The ultimate intrinsic SNR

In this manuscript, we follow eq. 6 in Ref. 30 to calculate the UISNR:

$$\zeta(\mathbf{r}_0) = \frac{\omega M_0}{\sqrt{4k_B T \left[\left(\mathbf{S}^H \mathbf{\Psi}^{-1} \mathbf{S} \right)^{-1} \right]_{0,0}}}. \quad (1)$$

Here, M_0 is the equilibrium magnetization and ω the angular Lamor frequency. During the whole study, we use the gyromagnetic ratio of protons. Furthermore, k_B is the Boltzmann constant, T the absolute temperature of the sample, $\mathbf{S}$ the receive sensitivity matrix and $\mathbf{\Psi}$ the noise covariance matrix. According to the principle of reciprocity,[31] the receive sensitivity of basis vector l at position $\mathbf{r}_0$ can be calculated by the complex left-handed component of the circularly polarized RF magnetic field[22]:

$$S_l(\mathbf{r}_0) = \frac{\mathbf{B}_l(\mathbf{r}_0)|_x - i\mathbf{B}_l(\mathbf{r}_0)|_y}{2}. \quad (2)$$

The noise covariance matrix of the basis set describes the noise power received by each basis vector and the correlated noise between different basis vectors.[30] The element $\Psi_{k,l}$ refers to the noise covariance between basis vector number k and l and is given by the following integral over the electric field[32,33]:

$$\Psi_{k,l} = \int_{\text{sample}} \sigma(\mathbf{r}) \mathbf{E}_k \cdot \mathbf{E}_l^* \, dV. \quad (3)$$

2.2 $\mid$ Theoretical SNR limits of curl- or divergence-free current patterns

A complete basis set of equivalent surface current patterns consists of both curl-free (superscript E) and divergence-free (superscript M) modes. We structure the $\mathbf{S}$- and $\mathbf{\Psi}$-matrices as follows:

$$\mathbf{S} = \begin{pmatrix} \mathbf{S}^M \\ \mathbf{S}^E \end{pmatrix} \quad (4)$$

$$\mathbf{\Psi} = \begin{pmatrix} \mathbf{\Psi}^M & \mathbf{\Psi}^{ME} \\ \left(\mathbf{\Psi}^{ME} \right)^H & \mathbf{\Psi}^E \end{pmatrix} \quad (5)$$

The submatrices $\mathbf{S}^M$ and $\mathbf{S}^E$ have size $K \times \rho$, where K is the number of vectors in the divergence-free or curl-free basis set and ρ is the acceleration factor in parallel imaging.[34] In this study, we are only considering the unaccelerated UISNR, i.e. $\rho = 1$. All submatrices of $\mathbf{\Psi}$ are of size $K \times K$. The matrices $\mathbf{\Psi}^M$ and $\mathbf{\Psi}^E$ are the noise covariance matrices of each divergence- and curl-free modes. In general, these modes could be coupled, which is described by the off-diagonal submatrix $\mathbf{\Psi}^{ME}$.

According to Equation 1, the UISNR ζ is obtained by using the entire $\mathbf{S}$ and $\mathbf{\Psi}$ matrix. Now, we define ζ^E as the best possible SNR achievable with curl-free current patterns. Therefore, only the submatrices $\mathbf{S}^E$ and $\mathbf{\Psi}^E$ are used when evaluating Equation 1, that is,

$$\zeta^E(\mathbf{r}_0) = \frac{\omega M_0}{\sqrt{4k_B T \left[\left((\mathbf{S}^E)^H (\mathbf{\Psi}^E)^{-1} \mathbf{S}^E \right)^{-1} \right]_{0,0}}}. \quad (6)$$

Analogously, we define the best possible SNR of divergence-free current patterns by:

$$\zeta^M(\mathbf{r}_0) = \frac{\omega M_0}{\sqrt{4k_B T \left[\left((\mathbf{S}^M)^H (\mathbf{\Psi}^M)^{-1} \mathbf{S}^M \right)^{-1} \right]_{0,0}}}. \quad (7)$$

The ratios ζ^M / ζ and ζ^E / ζ yield a direct performance measure to what extent divergence-free or curl-free current patterns are able to reach the UISNR threshold. It needs to be emphasized that due to the nonlinear SNR formation $\zeta^M / \zeta + \zeta^E / \zeta \neq 1$. In the special case of a diagonal noise matrix $\mathbf{\Psi}$, the relation $(\zeta^M / \zeta)^2 + (\zeta^E / \zeta)^2 = 1$ holds true (c.f. eq. 32 in Ref. 15).

2.3 $\mid$ Theoretical SNR limits of Φ- or Z-directed current patterns

For a surface current distribution defined on a cylinder, instead of curl- and divergence-free current patterns, Φ- and Z-directed current patterns can be used as a basis.[35] Then, the receive sensitivity and noise covariance matrices have the following structure:

$$\mathbf{S} = \begin{pmatrix} \mathbf{S}^Z \\ \mathbf{S}^\Phi \end{pmatrix} \quad (8)$$

$$\mathbf{\Psi} = \begin{pmatrix} \mathbf{\Psi}^Z & \mathbf{\Psi}^{Z\Phi} \\ \left(\mathbf{\Psi}^{Z\Phi} \right)^H & \mathbf{\Psi}^\Phi \end{pmatrix} \quad (9)$$

We define ζ^Φ as the best possible SNR achievable with Φ-directed current patterns, that is,

$$\zeta^\Phi(\mathbf{r}_0) = \frac{\omega M_0}{\sqrt{4k_B T \left[\left((\mathbf{S}^\Phi)^H (\mathbf{\Psi}^\Phi)^{-1} \mathbf{S}^\Phi \right)^{-1} \right]_{0,0}}}. \quad (10)$$

Similarly, we define the best possible SNR of Z-directed current patterns by:

$$\zeta^Z(\mathbf{r}_0) = \frac{\omega M_0}{\sqrt{4k_B T\left[\left((\mathbf{S}^Z)^H(\mathbf{\Psi}^Z)^{-1}\mathbf{S}^Z\right)^{-1}\right]_{0,0}}}. \quad (11)$$

The ratios ζ^Φ/ζ and ζ^Z/ζ yield a direct performance measure to what extent Φ- or Z-directed current patterns are able to reach the UISNR threshold. Again, due to the nonlinear SNR formation $\zeta^\Phi/\zeta + \zeta^Z/\zeta \neq 1$.

2.4 | The basis set

2.4.1 | Free-space fields of surface currents on a spherical cap

In eq. 4 of Ref. 22, Lattanzi and Sodickson used a surface current distribution of vector spherical harmonics (VSH) to excite eigenfunctions of the spherical Helmholtz operator. This surface current is running on a closed sphere around the sample. However, RF coils for human head imaging need to provide access for the human neck and cannot be entirely closed. For this reason, we use a basis set of surface current modes running on a spherical cap (i.e., a helmet-shaped coil holder) at a distance of R_c from the center of the coordinate system (Figure 1A,B). The current is constrained to run only within the range of $0 \leq \vartheta \leq \vartheta_0$. Since only a portion of the sphere is considered, ordinary VSH cannot be applied directly. Instead, for the first time we use vector spherical cap harmonics (definition see supporting information). Scalar spherical cap harmonics have been introduced by Haines to model the magnetic potential in geomagnetism.[36]

At the boundary ($\vartheta = \vartheta_0$), we enforce the ϑ-component of the current to be zero and for $\vartheta > \vartheta_0$ all current components are zero. For the divergence-free current patterns of amplitude I, we define vector spherical cap harmonics (VSCH) $\mathbf{X}_{\mu_k,m}$ of non-integer degree μ_k and integer order m ($m \in \mathbb{Z}$, $|m| < \mu_k$, $k \in \mathbb{N}^+$):

$$\mathbf{J}^M_{\mu_k,m} = \frac{I}{R_c}\delta(r-R_c)\mathbf{X}_{\mu_k,m}. \quad (12)$$

For the curl-free current patterns we use VSCH $\hat{\mathbf{r}} \times \mathbf{X}_{\lambda_k,m}$ of non-integer degree λ_k and integer order m ($m \in \mathbb{Z}$, $|m| < \lambda_k$, $k \in \mathbb{N}^+$):

$$\mathbf{J}^E_{\lambda_k,m} = \frac{I}{R_c}\delta(r-R_c)\hat{\mathbf{r}} \times \mathbf{X}_{\lambda_k,m}. \quad (13)$$

A detailed definition of the fractional degree VSCH can be found in the supporting information (Equations S1-S4). In the special case of $\vartheta_0 = 90°$ and $\vartheta_0 = 180°$ the fractional numbers μ_k and λ_k become integers and standard spherical harmonics are used. At this point, it is important to understand that the basis set is spanned by curl- and divergence-free current modes and that a particular mode is characterized by the integers k and m. To calculate the radiated fields from a

spherical cap surface current distribution, it is useful to express the VSCH as a series over VSH:

$$\mathbf{J}^M_{\mu_k,m} = \frac{I}{R_c}\delta(r-R_c)\sum_{l=|m|}^{\infty}\alpha^M_{l,m}(\mu_k)\mathbf{X}_{l,m} + \alpha^E_{l,m}(\mu_k)\hat{\mathbf{r}} \times \mathbf{X}_{l,m} \quad (14)$$

$$\mathbf{J}^E_{\lambda_k,m} = \frac{I}{R_c}\delta(r-R_c)\sum_{l=|m|}^{\infty}\beta^M_{l,m}(\lambda_k)\mathbf{X}_{l,m} + \beta^E_{l,m}(\lambda_k)\hat{\mathbf{r}} \times \mathbf{X}_{l,m} \quad (15)$$

The expansion coefficients $\alpha^M_{l,m}$, $\alpha^E_{l,m}$, $\beta^M_{l,m}$, and $\beta^E_{l,m}$ are given in Equations S9-S12 in the supporting information. Calculating the VSH transform, it turns out that the term $\alpha^E_{l,m}(\mu_k)$ is always zero. The free-space fields of the above basis set can be calculated with dyadic Green's functions (DGF)[28]:

$$\mathbf{E}^M_{\mu_k,m}(\mathbf{r}) = -\omega\mu_0 IR_c k_0 \sum_{l=|m|}^{\infty}\alpha^M_{l,m}\begin{cases} V^M_l \mathbf{M}^{(1)}_{l,m}(\mathbf{r}) & r > R_c \\ W^M_l \mathbf{M}_{l,m}(\mathbf{r}) & r < R_c \end{cases} \quad (16)$$

$$\mathbf{E}^E_{\lambda_k,m}(\mathbf{r}) = -\omega\mu_0 IR_c k_0 \sum_{l=|m|}^{\infty}\beta^M_{l,m}\begin{cases} V^M_l \mathbf{M}^{(1)}_{l,m}(\mathbf{r}) \\ W^M_l \mathbf{M}_{l,m}(\mathbf{r}) \end{cases}$$
$$+ \beta^E_{l,m}\begin{cases} V^E_l \mathbf{N}^{(1)}_{l,m}(\mathbf{r}) & r > R_c \\ W^E_l \mathbf{N}_{l,m}(\mathbf{r}) & r < R_c \end{cases} \quad (17)$$

$$\mathbf{H}^M_{\mu_k,m}(\mathbf{r}) = iIR_c k_0^2 \sum_{l=|m|}^{\infty}\alpha^M_{l,m}\begin{cases} V^M_l \mathbf{N}^{(1)}_{l,m}(\mathbf{r}) & r > R_c \\ W^M_l \mathbf{N}_{l,m}(\mathbf{r}) & r < R_c \end{cases} \quad (18)$$

$$\mathbf{H}^E_{\lambda_k,m}(\mathbf{r}) = iIR_c k_0^2 \sum_{l=|m|}^{\infty}\beta^M_{l,m}\begin{cases} V^M_l \mathbf{N}^{(1)}_{l,m}(\mathbf{r}) \\ W^M_l \mathbf{N}_{l,m}(\mathbf{r}) \end{cases}$$
$$+ \beta^E_{l,m}\begin{cases} V^E_l \mathbf{M}^{(1)}_{l,m}(\mathbf{r}) & r > R_c \\ W^E_l \mathbf{M}_{l,m}(\mathbf{r}) & r < R_c \end{cases} \quad (19)$$

The vector functions $\mathbf{M}_{l,m}$, $\mathbf{M}^{(1)}_{l,m}$, $\mathbf{N}_{l,m}$, and $\mathbf{N}^{(1)}_{l,m}$ are fundamental solutions to the Helmholtz equation in spherical coordinates and were already defined and discussed in eqs. 8 and 9 in Ref. 15. The boundary coefficients V^M_l, V^E_l, W^M_l, and W^E_l are specified in the supporting information in Equations S17-S20.

2.4.2 | Free-space fields of a cylindrical surface current distribution

Another possibility to provide space for the human neck is to constrain the current to run on a cylindrical surface of radius R_c. In Ref. 23, Schnell defined the following basis set of vector cylindrical harmonics (VCH):

$$\mathbf{J}^M_{n,h} = I\delta(r-R_c)\nabla \times \left(e^{in\Phi}e^{ihz}\mathbf{e}_r\right) \quad (20)$$

$$\mathbf{J}^E_{n,h} = I\delta(r-R_c)\nabla\left(e^{in\Phi}e^{ihz}\right). \quad (21)$$

Again, the basis set is spanned by curl- and divergence-free modes and a particular mode is characterized by the

eigenvalues $n \in \mathbb{Z}$ and $h \in \mathbb{R}$. Applying the DGF formalism to the basis set, this yields the free-space fields[28]:

$$\mathbf{E}_{n,h}^{M} = i\frac{I\omega\mu_0\pi}{2\eta_0^2}\left(V_{n,h}^{MM}\mathbf{M}_{n,h}(\eta_0) + V_{n,h}^{MN}\mathbf{N}_{n,h}(\eta_0)\right) \quad r < R_c$$

(22)

$$\mathbf{E}_{n,h}^{E} = i\frac{I\omega\mu_0\pi}{2\eta_0^2}\left(V_{n,h}^{EM}\mathbf{M}_{n,h}(\eta_0) + V_{n,h}^{EN}\mathbf{N}_{n,h}(\eta_0)\right) \quad r < R_c \quad (23)$$

$$\mathbf{H}_{n,h}^{M} = \frac{Ik_0\pi}{2\eta_0^2}\left(V_{n,h}^{MM}\mathbf{N}_{n,h}(\eta_0) + V_{n,h}^{MN}\mathbf{M}_{n,h}(\eta_0)\right) \quad r < R_c \quad (24)$$

$$\mathbf{H}_{n,h}^{E} = \frac{Ik_0\pi}{2\eta_0^2}\left(V_{n,h}^{EM}\mathbf{N}_{n,h}(\eta_0) + V_{n,h}^{EN}\mathbf{M}_{n,h}(\eta_0)\right) \quad r < R_c \quad (25)$$

The vector functions $\mathbf{M}_{n,h}$ and $\mathbf{N}_{n,h}$ are fundamental solutions to the Helmholtz equation in cylindrical coordinates and were already defined and discussed in Ref. 37. The boundary coefficients $V_{n,h}^{MM}$, $V_{n,h}^{MN}$, $V_{n,h}^{EM}$, and $V_{n,h}^{EN}$ are specified in the supporting information in Equations S27-S30. The term $\eta_0^2 = k_0^2 - h^2$ is the propagation constant in radial direction.

There is a linear transform from the curl- and divergence-free basis to the Φ- and Z-directed basis,[35] which can be directly derived from Equations 20 and 21:

$$\begin{pmatrix} \mathbf{J}_{n,h}^{Z} \\ \mathbf{J}_{n,h}^{\Phi} \end{pmatrix} = \underbrace{\begin{pmatrix} -\dfrac{in}{R_c} & ih \\ ih & \dfrac{in}{R_c} \end{pmatrix}}_{\mathbf{T}_{n,h}} \begin{pmatrix} \mathbf{J}_{n,h}^{M} \\ \mathbf{J}_{n,h}^{E} \end{pmatrix}$$

(26)

With the transformation matrix $\mathbf{T}_{n,h}$ the receive sensitivity and noise covariance matrices can be transformed into:

$$\begin{pmatrix} S_{n,h}^{Z}(\mathbf{r}_0) \\ S_{n,h}^{\Phi}(\mathbf{r}_0) \end{pmatrix} = \mathbf{T}_{n,h}\begin{pmatrix} S_{n,h}^{M}(\mathbf{r}_0) \\ S_{n,h}^{E}(\mathbf{r}_0) \end{pmatrix}$$

(27)

$$\begin{pmatrix} \Psi_{(n,h),(n',h')}^{Z} & \Psi_{(n,h),(n',h')}^{Z\Phi} \\ \left(\Psi_{(n',h'),(n,h)}^{Z\Phi}\right)^* & \Psi_{(n,h),(n',h')}^{\Phi} \end{pmatrix}$$
$$= \mathbf{T}_{n,h}\begin{pmatrix} \Psi_{(n,h),(n',h')}^{M} & \Psi_{(n,h),(n',h')}^{ME} \\ \left(\Psi_{(n',h'),(n,h)}^{ME}\right)^* & \Psi_{(n,h),(n',h')}^{E} \end{pmatrix}\mathbf{T}_{n',h'}^{H}$$

(28)

2.5 | Analytical field calculation in a dielectric sphere

For a closed surface current distribution, a comprehensive study of the UISNR in a dielectric sphere was done in Ref. 15. This paragraph summarizes the theory to calculate the UISNR of a surface current distribution defined on a spherical cap.

A dielectric sphere with radius R_s, electric conductivity σ and relative permittivity ϵ_r is surrounded by a spherical cap surface current distribution of radius R_c and cap angle ϑ_0 (s. Figure 1A). Assuming $e^{-i\omega t}$ time dependence throughout the whole article, the complex propagation constant inside the sphere becomes $k_{in} = \omega\sqrt{\mu_0\epsilon_0\epsilon_r(1 + i\sigma/(\omega\epsilon_0\epsilon_r))}$. For completeness, we also define the vacuum propagation constant $k_0 = \omega\sqrt{\mu_0\epsilon_0}$. With the help of the DGF technique, the electromagnetic fields inside the sphere and excited by the basis set of Equations 14 and 15 can be calculated. For brevity, we do not give expressions for the electric and magnetic fields, but directly present the relevant quantities for the UISNR calculations. The noise covariance elements $\Psi_{(\mu_k,m),(\mu_{k'},m')}^{M}$, $\Psi_{(\mu_k,m),(\lambda_{k'},m')}^{ME}$, and $\Psi_{(\lambda_k,m),(\lambda_{k'},m')}^{E}$ are given by:

$$\Psi_{(\mu_k,m),(\mu_{k'},m')}^{M} = \delta_{mm'}\sum_{l=|m|}^{\infty}\alpha_{l,m}^{M}(\mu_k)\tilde{\Psi}_l^{M}\left(\alpha_{l,m'}^{M}(\mu_{k'})\right)^* \quad (29)$$

$$\Psi_{(\mu_k,m),(\lambda_{k'},m')}^{ME} = \delta_{mm'}\sum_{l=|m|}^{\infty}\alpha_{l,m}^{M}(\mu_k)\tilde{\Psi}_l^{M}\left(\beta_{l,m'}^{M}(\lambda_{k'})\right)^* \quad (30)$$

$$\Psi_{(\lambda_k,m),(\lambda_{k'},m')}^{E} = \delta_{mm'}\sum_{l=|m|}^{\infty}\beta_{l,m}^{M}(\lambda_k)\tilde{\Psi}_l^{M}\left(\beta_{l,m'}^{M}(\lambda_{k'})\right)^*$$
$$+ \beta_{l,m}^{E}(\lambda_k)\tilde{\Psi}_l^{E}\left(\beta_{l,m'}^{E}(\lambda_{k'})\right)^*$$

(31)

Here, $\tilde{\Psi}_l^{M}$ and $\tilde{\Psi}_l^{E}$ are the loss terms associated with the fundamental surface current distributions $I\delta(r - R_c)\mathbf{X}_{l,m}$ and $I\delta(r - R_c)\hat{\mathbf{r}}\times\mathbf{X}_{l,m}$. Mathematical expressions can be found in the supporting information in Equations S31 and S32. The receive sensitivities $S_{\mu_k,m}^{M}(\mathbf{r}_0)$ and $S_{\lambda_k,m}^{E}(\mathbf{r}_0)$ are given by:

$$S_{\mu_k,m}^{M}(\mathbf{r}_0) = \frac{1}{2}iIR_ck_0k_{in}\mu_0\sum_{l=|m|}^{\infty}\alpha_{l,m}^{M}(\mu_k)C_lW_l^{M}\left(\mathbf{N}_{l,m}(\mathbf{r}_0)|_x - i\mathbf{N}_{l,m}(\mathbf{r}_0)|_y\right)$$

(32)

$$S_{\lambda_k,m}^{E}(\mathbf{r}_0) = \frac{1}{2}iIR_ck_0k_{in}\mu_0\sum_{l=|m|}^{\infty}\beta_{l,m}^{M}(\lambda_k)$$
$$C_lW_l^{M}\left(\mathbf{N}_{l,m}(\mathbf{r}_0)|_x - i\mathbf{N}_{l,m}(\mathbf{r}_0)|_y\right) + \ldots$$
$$\beta_{l,m}^{E}(\lambda_k)D_lW_l^{E}\left(\mathbf{M}_{l,m}(\mathbf{r}_0)|_x - i\mathbf{M}_{l,m}(\mathbf{r}_0)|_y\right)$$

(33)

The boundary coefficients C_l and D_l are specified in the supporting information in Equations S21 and S22.

2.6 | Numerical field computation in a heterogeneous head model

A basis set of equivalent surface current patterns is exciting electromagnetic fields in a heterogeneous head model. Due to the linearity of the head model, the resulting field can be decomposed into an incident and scattered field[38]:

$$\mathbf{E} = \mathbf{E}_{inc} + \mathbf{E}_{scat}$$

(34)

$$H = H_{inc} + H_{scat}. \qquad (35)$$

The incident field is defined as the field excited by the sources in free-space, that is, in absence of the head model. The incident field excites polarization currents in the dielectric head, that re-radiate and create the so called scattered fields.[38] With the help of polarization currents (J), Equation 34 can be reformulated as a volume integral equation (VIE), abbreviated with JVIE. Recently, a fast FFT-based volume integral equation method was published to efficiently solve the JVIE-problem.[39–41] The authors distribute their code named "MARIE" under https://github.com/thanospol/MARIE.

Now, evaluating the UISNR in a voxel model is straightforward: First, one of the before mentioned basis sets (either VSCH or VCH) is chosen and the free-space field of each mode is calculated. Afterwards, these incident fields are fed into the JVIE solver "MARIE" to numerically solve the scattering problem. With the resulting electric fields in the scatterer, the modes' noise covariance matrix can be computed (Equation 3) and with the resulting magnetic fields the receive sensitivity matrix (Equation 2).

3 | METHODS

3.1 | Study design

The UISNR was evaluated in three different setups, which are shown in Figure 1. For all three setups, we covered all practically relevant field strengths for human application: 1.5 T (64 MHz), 3 T (128 MHz), 7 T (298 MHz), 9.4 T (400 MHz), 10.5 T (447 MHz), 11.7 T (498 MHz). First, we calculated the UISNR ζ and the best possible SNR of curl- (ζ^E) and divergence-free (ζ^M) modes in a dielectric spherical sample of human head size (Figure 1A). We used the analytic VSCH-DGF framework outlined in the previous section. The radius R_s was 9.2 cm and the electromagnetic properties of the sphere were adjusted to average properties of gray and white matter according to the Gabriel database.[42] We used the same values as listed in fig. 1 in Ref. 15. The radius of the spherical cap was set to $R_c = 12.2$ cm, which is the same radius as in our previous work.[15] To study the effect of the cap angle ϑ_0 on the UISNR, we monotonously increased ϑ_0 in discrete steps from $91°$, $120°$, $160°$ to $180°$. A spatial grid with isotropic resolution of about 1.9 mm was used. For cross-validation purposes, we ran an additional UISNR simulation at 9.4 T and $\vartheta_0 = 120°$ with the numeric VSCH-JVIE method using the same spherical model. The JVIE simulations were done with varying spatial resolutions of 2.9 mm, 2.3 mm, and 1.9 mm isotropically to study the impact of meshgrid resolution. Moreover, convergence of the VSCH-DGF method was investigated at six different voxel positions.

Next, we replaced the spherical sample by a realistic human head model and evaluated ζ^E and ζ^M of a spherical cap surface current distribution (Figure 1B). We chose voxel model "Duke" from the virtual family[43] having an isotropic resolution of 2 mm. To save computational resources and simulation time, we truncated the voxel model beyond the neck. We applied a radius of the surface current distribution of $R_c = 13$ cm and a cap angle of $\vartheta_0 = 120°$. The coordinate center of the spherical cap was placed in the third ventricle. This resulted in an average distance between the spherical cap and the voxel model of about 3.1 cm. The UISNR was numerically calculated by the VSCH-JVIE framework presented in the past section. For validation, we compared our results with the UISNR from a randomized dipole excitation.[19] The random dipole excitation was done in the same body model but with a mesh resolution of 3 mm isotropically. We did not run the dipole simulations but downloaded the results from http://ptx.martinos.org/index.php/Main_Page. As an additional validation step, we checked the convergence of the UISNR at six different voxel positions. We calculated ideal current patterns and their separation into curl- and divergence-free modes for three exemplary voxel positions at 1.5 T and 9.4 T field strength. Besides calculating ζ^E and ζ^M, we also used setup 1b to study the increase of the UISNR ζ with regard to field strength B_0. For every voxel position, we fitted a power series model of the form cB_0^n to the simulated UISNR data points. This was accomplished by MATLAB's (MathWorks, Natick, MA) fit function routine with the model type "power1". As a result, we got a spatial distribution of the exponent n, visualizing sub- and superlinear growth of the UISNR ζ. We repeated this fitting for ζ^E and ζ^M.

Regarding the last setup (Figure 1C), we exchanged the spherical by a cylindrical surface current distribution. Again, the radius R_c was 13 cm. This time, the coordinate center was shifted by 2.3 cm in caudal direction and was located ventrally to the pons. The UISNR was numerically calculated by the VCH-JVIE framework. Besides evaluating the best possible SNR of curl- and divergence-free current modes, we were also interested in the SNR performance of Φ- and Z-directed current patterns. Therefore, we transformed the curl- and divergence-free basis set into a Φ- and Z-directed basis set by applying Equations 27 and 28. We illustrate ideal current patterns and their separation into curl- and divergence-free or Z- and Φ-directed modes for one exemplary voxel position at 9.4 T field strength.

3.2 | Algorithmic implementation

We implemented VSCH-JVIE, VCH-JVIE, and VSCH-DGF in double-precision arithmetic in an object-orientated toolbox in MATLAB, where the JVIE functionality was provided by the MARIE code. All JVIE-simulations were executed on a

dedicated high performance server with 128 GB of RAM, 2×12 core CPU (Intel Xeon E5–2650 v4 @2.2 GHz) and $2\times$ NVIDIA Tesla P100 GPU. Since we had two GPUs available, both, VSCH-JVIE and VCH-JVIE were parallelized in such a way, that the electromagnetic fields of two basis vectors were calculated simultaneously. Simulation times for the VSCH basis set are reported in the Supporting Information Figure S1. The JVIE-system was solved with the biconjugate gradients stabilized method,[44] preimplemented in MATLAB's "bicgstab" solver. The tolerance of the solver was set to 1e−8.

In order to evaluate the UISNR, the infinite dimensional vector spaces of VSCH ($k \in \mathbb{N}^+$, $m \in \mathbb{Z}$) and VCH ($n \in \mathbb{Z}$, $h \in \mathbb{R}$) needed to be truncated to finite dimensionality. Regarding VSCH, k was running from $k=1,2,\ldots,N_k$ and m from $m=0,\pm1,\pm2,\ldots,\pm N_m$. Moreover, the infinite series expansion of Equations 14 and 15 needed to be truncated. We stopped the summation after $l = 80$. This limit was also enforced for the sums in Equations 16-19 and 29-33. When applying VSCH to the spherical model (Figure 1A), we used $N_m=N_k=20$, resulting in totally 1640 basis vectors. In the special case of $\vartheta_0=180°$, the integer degree index l was within the range $l=1,2,\ldots,30$ and the integer order index m was between $-l \leq m \leq l$. All together, the basis set spanned 1920 vectors. For the VSCH-JVIE simulations in Duke (Figure 1B), we increased the values of N_m and N_k to 25, corresponding to 2550 basis vectors. With respect to VCH-JVIE (Figure 1C), the mode index n was running from $n=0,\pm1,\pm2,\ldots,\pm15$ and $h=k\pi/L$, with $k=0,\pm1,\pm2,\ldots,\pm24$ and $2L$ being the spatial periodicity. We chose $L = 15$ cm to have good longitudinal coverage of the head model (c.f. Figure 1C). The VCH basis set comprised 3038 basis vectors.

In order to evaluate the UISNR, the inverse of the noise covariance matrix needs to be calculated (cf. Equation 1). Using the VSCH basis set, we used MATLAB's "inv" function. For the VCH basis set, the condition number of the noise covariance matrix was too high to give reasonable results using "inv". Therefore, we used the more robust "pinv" method.

4 | RESULTS

4.1 | Validation

To check, whether the truncation order of the VSCH basis set was chosen sufficiently high, we plot the convergence of the UISNR for the sphere (Supporting Information Figure S2) and the human voxel model (Figure 2). In the spherical sample (Supporting Information Figure S2), the UISNR obtained by the analytic VSCH-DGF basis set converged at all six voxel positions and for all field strengths B_0. The relative change of the UISNR was below 6.3e−10 for all tested

voxel positions and all field strengths. Proceeding to Figure 2, the UISNR in Duke converged more slowly than in the spherical model. The relative change of the UISNR was below 6.2e−8 for all tested voxel positions and all field strengths.

Figure 3A compares the best possible SNR of divergence-free current patterns ζ^M in a dielectric sphere evaluated by VSCH-JVIE with results from VSCH-DGF. To test the impact of mesh resolution on the ratios ζ^M/ζ and ζ^E/ζ we used a uniform Cartesian grid with 64, 80, and 96 samples in each spatial direction. This corresponds to an isotropic resolution of approximately 2.92 mm, 2.33 mm, and 1.94 mm. Having a mesh resolution of about 1.94 mm, we found a maximum deviation of 5% at 9.4 T. In Supporting Information Figure S3, we plot the ratio ζ^M/ζ for different spatial resolutions of the VSCH-JVIE method. The finer the mesh, the better the numerical JVIE results approach analytic results. In Figure 3B, we show the relative UISNR gain in Duke when increasing B_0 from 7 T to 9.4 T. The results were calculated with VSCH-JVIE and a randomized dipole excitation. Both methods predict an UISNR increase by a factor of two in central head regions. A more comprehensive comparison between UISNR results obtained from VSCH-JVIE and a randomized dipole excitation is presented in the Supporting Information Figure S4. All validation steps underline the validity of the VSCH-JVIE approach.

4.2 | Spherical cap surface current distribution

Figure 4 illustrates the UISNR obtained by an open-pole surface current distribution with cap angle ϑ_0 divided by the UISNR of an entirely closed surface current distribution in a dielectric sphere of human head size. This normalized figure is almost frequency independent. For the case $\vartheta_0=120°$, the ratio $\zeta(\vartheta_0=120°)/\zeta(\vartheta_0=180°)$ has an average value of almost 1 on the northern hemisphere, 0.77 on the southern hemisphere and 0.9 over the entire sphere. The more the cap angle approaches $180°$, the closer these values become 1. To fit the head model into the spherical cap an opening angle of $120°$ was chosen.

In Figure 5, the SNR performance of curl- and divergence-free current patterns relative to the UISNR in the sphere are shown. The total UISNR ζ is obtained from both curl- and divergence-free current modes, whereas ζ^M results from divergence-free modes only and ζ^E from curl-free modes only. In general, the cap angle ϑ_0 influences ζ^M much less than ζ^E. This becomes clear when focusing on one field strength B_0: the spatial distribution of ζ^M/ζ is similar for all cap angles, whereas the spatial distribution of ζ^E/ζ heavily depends on ϑ_0. For example, divergence-free current patterns always achieve 100% of the UISNR in the central region of the sphere, independent of the cap angle. In contrast, curl-
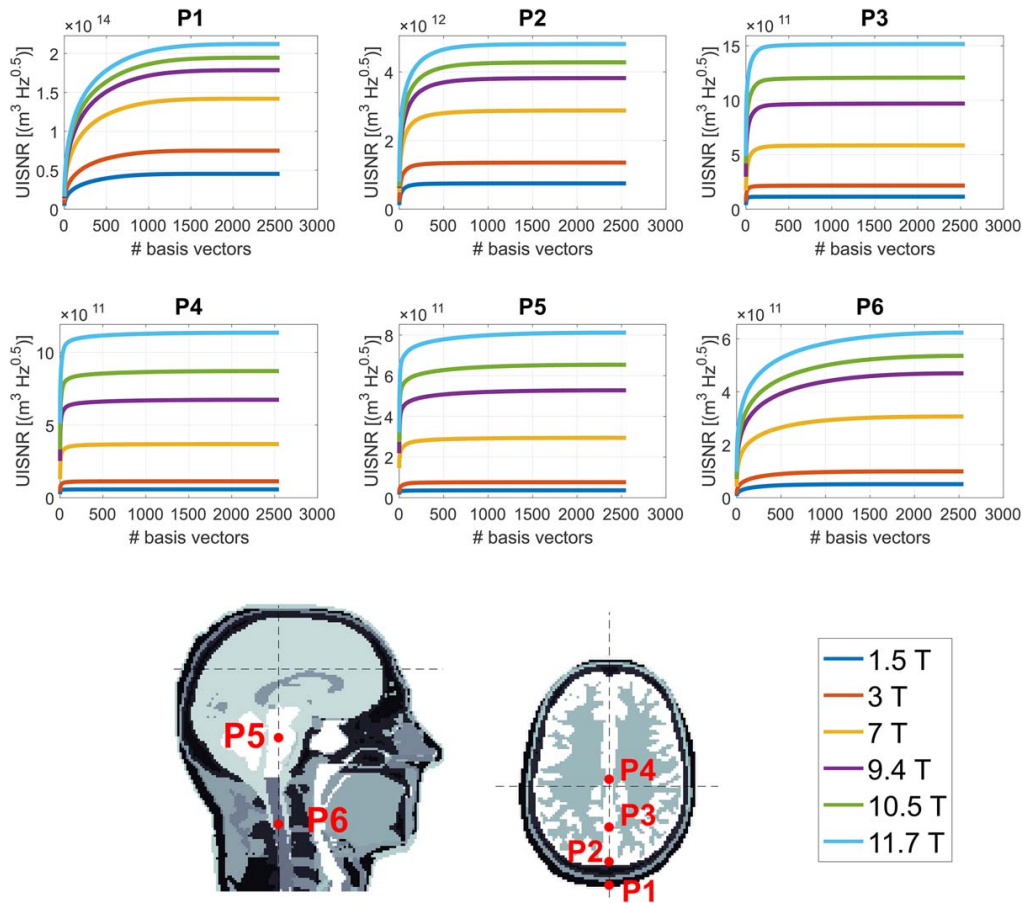
Convergence of VSCH in Duke

FIGURE 2 Convergence of the UISNR at six different locations and field strengths in voxel model Duke with the VSCH-JVIE basis set

free modes have low SNR performance in the center for $\vartheta_0 = 180°$, but with decreasing cap angle ϑ_0 their central SNR ζ^E increases. Moreover, divergence-free current patterns saturate the UISNR in the periphery of the sphere (true for all field strengths) and almost fully achieve the UISNR at all positions at 1.5 T and 3 T. In the case of an open-pole surface current distribution ($\vartheta_0 < 180°$), the ratio ζ^E/ζ reaches its maximum on the southern hemisphere. The effect is especially pronounced at $\vartheta_0 = 120°$ and $\vartheta_0 = 160°$.

Figure 6 illustrates the SNR performance of curl- and divergence-free modes in voxel model Duke. Qualitatively, the spatial distributions of ζ^M/ζ or ζ^E/ζ in Duke resemble the spatial distributions in the spherical model (Figure 5). The SNR ζ^M of divergence-free modes saturates the UISNR in the peripheral and central (midbrain, thalamus) head regions for all field strengths. However, for 7 T and above, there are parts in the human head where divergence-free current patterns cannot reach the UISNR limit. The minimum

values are 81% (7 T), 69% (9.4 T), and 67% (11.7 T) (cf. Figure 6). Consequently, using both curl- and divergence-free current patterns rather than divergence-free currents alone results in 24% (7 T), 45% (9.4 T), and 49% (11.7 T) higher SNR at these positions. At lower field strength the minima of the distribution ζ^M/ζ are around 90%. Whereas the SNR performance of divergence-free current patterns decreases with higher B_0-fields, curl-free currents behave the opposite way. At low field, they are not efficient, but at ultra-high field they have a maximum ratio ζ^E/ζ of 86% (11.7 T). The region of maximum ζ^E falls into a region of minimum ζ^M. In Supporting Information Figure S5, we plot ideal current patterns for voxel P4 (positioning of voxel see Figure 2) at 9.4 T. By visual inspection, the components $\mathbf{J}^M$ and $\mathbf{J}^E$ are truly divergence- and curl-free. We provide additional figures illustrating ideal current patterns on the spherical cap for different field strengths and voxel positions in Supporting Information Figures S6-S11.
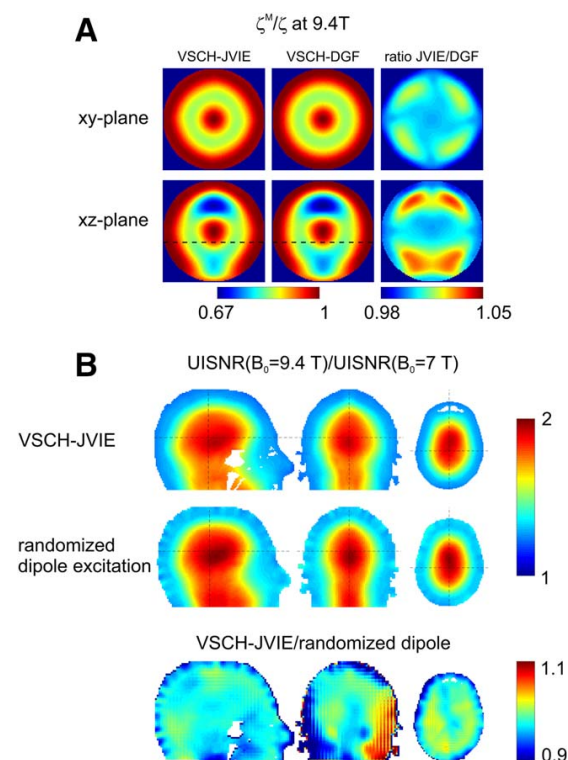
FIGURE 3 Validation of the proposed VSCH-JVIE method: (A) The best possible SNR of divergence-free current modes relative to the UISNR is calculated for a spherical sample with a cap angle of $\vartheta_0 = 120^\circ$. The results obtained by the VSCH-JVIE method are compared to analytic results. (B) The increase of the total UISNR with field strength: the ratio UISNR($B_0 = 9.4$ T)/UISNR($B_0 = 7$ T) in voxel model Duke is shown for the VSCH-JVIE approach, used in this work and compared to a randomized dipole excitation used by Guerin et al.[19]

4.3 | Cylindrical surface current distribution

When a cylindrical surface current distribution is used, Figure 7 visualizes the SNR performance of curl- and divergence-free current patterns in voxel model Duke. The behavior of ζ^M/ζ and ζ^E/ζ with regard to field strength B_0 is similar to the spherical cap setup: When B_0 increases, the minimum of ζ^M/ζ decreases, whereas the maximum of ζ^E/ζ grows. The minimum values for ζ^M/ζ are 83% (7 T), 75% (9.4 T), and 72% (11.7 T). The region of minimum ζ^M is different than in the spherical cap configuration: At ultra-high field, the UISNR threshold in central parts of the head cannot be reached with divergence-free current patterns only. The combination of curl- and divergence-free patterns results in 21% (7 T), 33% (9.4 T), and 39% (11.7 T) higher SNR in deep brain regions in comparison to ζ^M. Ideal current patterns for the cylindrical surface are provided in Supporting Information Figure S12. By visual inspection, the components $\mathbf{J}^M$ and $\mathbf{J}^E$ are truly divergence- and curl-free.

We were also interested to what extent Z- and Φ-directed current patterns are able to reach the UISNR limit. The results are presented in Figure 8. This is of high practical relevance, as the ratio ζ^Z/ζ indicates how close arrays of Z-directed dipoles approach the UISNR threshold. Z-directed current patterns reach their maximal SNR performance in central regions of the human head (Figure 8). In the peripheral parts of the head, they are not efficient. The higher the magnetic field B_0, the closer the maximum of ζ^Z/ζ reaches the UISNR limit. At 7 T and above, Z-directed current patterns achieve 93% of the UISNR at central head positions. Φ-directed current patterns are required to complete the basis set, that is, the combination of Z- and Φ-directed current patterns results in the UISNR. Ideal current patterns for the cylindrical surface are provided in Supporting Information Figure S13. By visual inspection, the components $\mathbf{J}^Z$ and $\mathbf{J}^\Phi$ are truly Z- and Φ-directed.

Finally, we were interested in comparing the SNR efficiency of loop-only and dipole-only head arrays. Therefore, in Figure 9 we plot the ratio ζ^Z/ζ^M. At 1.5 T and 3 T, divergence-free current patterns result in higher SNR than Z-

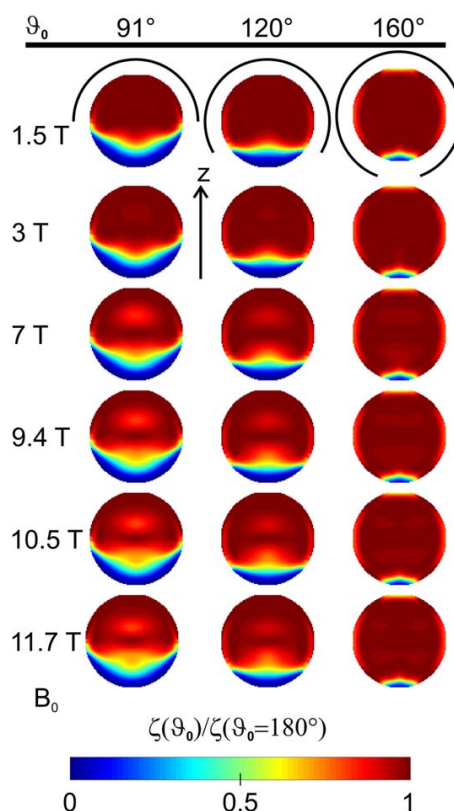**FIGURE 4** The UISNR in a dielectric sphere of human head size obtained by a spherical cap surface current distribution with cap angle ϑ_0 divided by the UISNR of a completely surrounding surface current distribution. The plots show slices in the plane y = 0
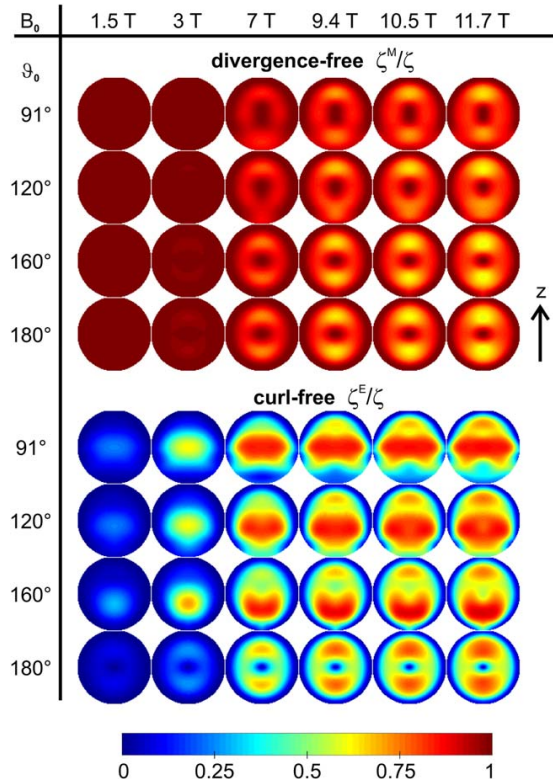
FIGURE 5 The best possible SNR of curl-and divergence-free current patterns relative to the UISNR in a dielectric sphere of human head size. The cap angle ϑ_0 of the spherical cap surface current distribution was varied between $91°$ and $180°$. The plots show slices in the plane y = 0

directed current patterns in the whole head. At 7 T, there is a small volume close to the sphenoidal sinus where Z-directed currents result in higher SNR than divergence-free currents. Otherwise, divergence-free currents have superior SNR performance at 7 T. At 9.4 T and above, Z-directed current patterns start to outperform divergence-free current patterns in central parts of the head. There, the SNR gain over divergence-free current patterns is 24% (9.4 T) and 26% (10.5 T, 11.7 T).

4.4 | The increase of the UISNR with regard to field strength

We demonstrate the increase of the UISNR with regard to B_0 in Figure 10. The UISNR was evaluated with the VSCH basis set. As an example, in subfigure A we plot the fitted curves for three distinct voxel positions in Duke. At positions P1, P3, and P4 (c.f. Figure 2), the fitted exponent n was 0.76, 1.70, and 2.13, respectively. Fitting the UISNR ζ to a power series model $\zeta = cB_0^n$, subfigure B visualizes the spatial distribution of the exponent n. For all voxel positions, the coefficient of determination (R^2) of the fit was larger than

0.98. In the left column, the behavior of the total UISNR is shown: In the peripheral region of the head (skin, skull) the UISNR increases sublinearly. The linear threshold (dashed line) is about 16–20 mm away from the skin and follows the skull bones. In the cerebrum, the UISNR increases superlinearly, with a more than quadratic increase in deep brain regions.

It is interesting to investigate the SNR increase for divergence-free and curl-free modes separately. The middle column illustrates, that the SNR increase of divergence-free modes is very similar to the complete basis set. In contrast, the right column suggests, that the SNR obtained from curl-free modes grows much faster than the SNR obtained from divergence-free modes. In the entire cerebrum, the exponent n was larger than 2 and had a value of about 2.8 deeply in the brain.

5 | DISCUSSION

The aim of this work was to study the SNR performance of loop- and dipole-like current patterns in a realistic human head model. Therefore, we evaluated the best possible SNR
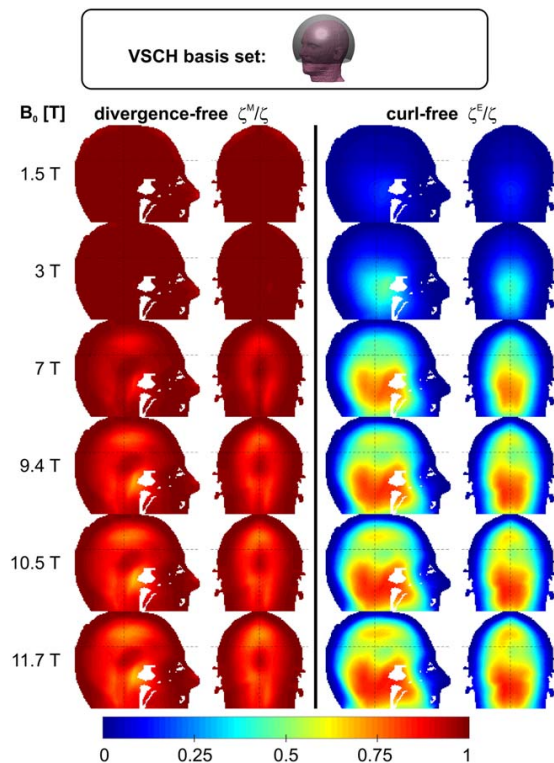

FIGURE 6 The best possible SNR of curl- and divergence free current patterns relative to the UISNR in voxel model Duke for a spherical cap surface current distribution. We used a cap angle of $\vartheta_0 = 120°$
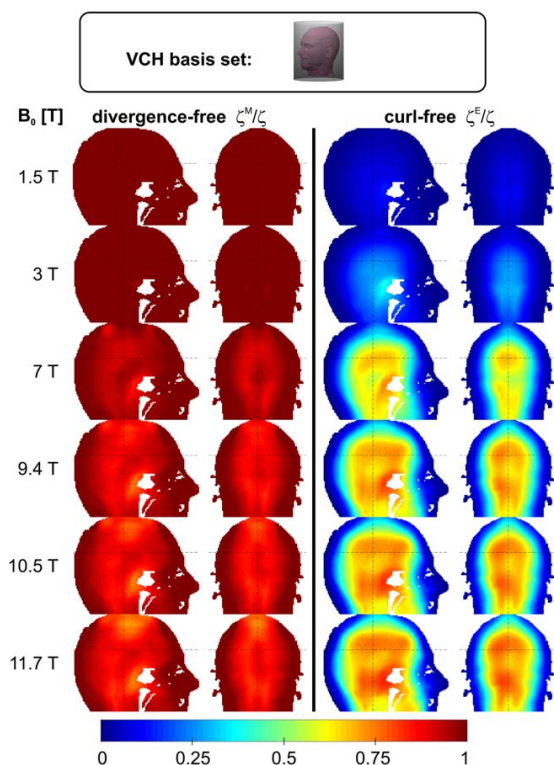
FIGURE 7 The best possible SNR of curl- and divergence-free current patterns relative to the UISNR in voxel model Duke for a cylindrical surface current distribution

achievable with either divergence-free or Z-directed current patterns and compared these values to the UISNR. To summarize our results, we would like to emphasize the following points:

- By definition, the UISNR is independent from the choice of receive array, and therefore from the geometry of the surface where the current patterns are defined. However, the relative SNR performance of curl- and divergence-free and Z- and Φ-directed current patterns depends on the particular choice of the Huygens' surface.

- Using a helmet-shaped coil holder, there is a maximal SNR increase of 24% (7 T), 45% (9.4 T), and 49% (11.7 T) in the human head when using a combination of curl- and divergence-free current patterns over divergence-free current patterns only. For the cylindrical surface the corresponding SNR increase is 21% (7 T), 33% (9.4 T), and 39% (11.7 T).

- Using a cylindrical coil holder, at 9.4 T and above, Z-directed current patterns outperform divergence-free current patterns in central regions of the human head.

- Between 1.5 T and 11.7 T the UISNR increases superlinearly with B_0 in most parts of the cerebrum.

5.1 | Practical guidelines for RF coil design

Regarding RF coil design for the human head, we conclude the following guidelines from our simulation studies. Independent of the array holder geometry, on 1.5T and 3T platforms, we recommend using loop-only receive arrays, which correspond to divergence-free current patterns. This covers more than 90% of the UISNR at every voxel position in the human head. At 7 T and above, the spatial distribution of ζ^M/ζ becomes more inhomogeneous and the minima of the distribution become smaller. This is true for the helmet and the cylindrical holder. As a result, the SNR performance of loop-only receivers can be substantially increased in those regions of low ζ^M/ζ by adding complementary current patterns.

On a cylindrical coil holder, loop elements can be complemented by Z-directed current patterns. The combination of divergence-free and Z-directed currents provides a complete basis set, as Z-directed currents are obtained by a linear transform of curl- and divergence-free currents (see Equation 26). Therefore, divergence-free currents can be complemented by Z-directed currents and the combination of the two results in the UISNR (same value as if basis of divergence- and curl-free currents were used). Comparing the SNR performance of divergence-free current patterns (Figure
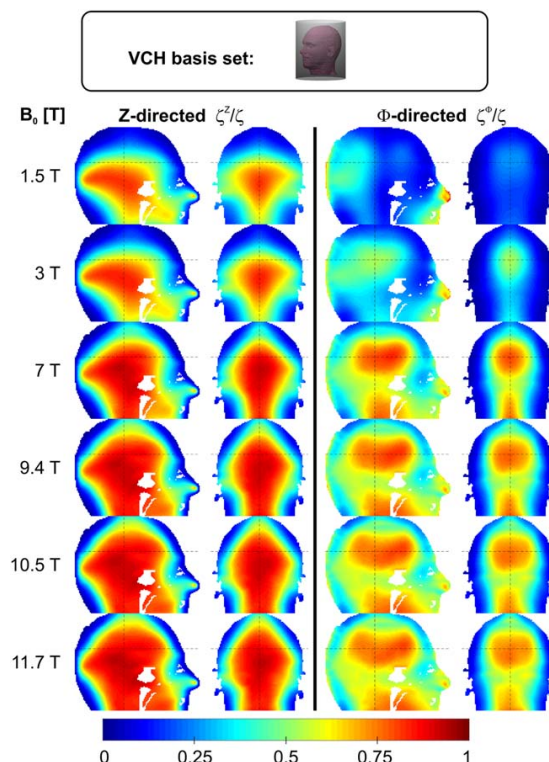

FIGURE 8 The best possible SNR of Z- and Φ-directed current patterns relative to the UISNR in voxel model Duke for a cylindrical surface current distribution
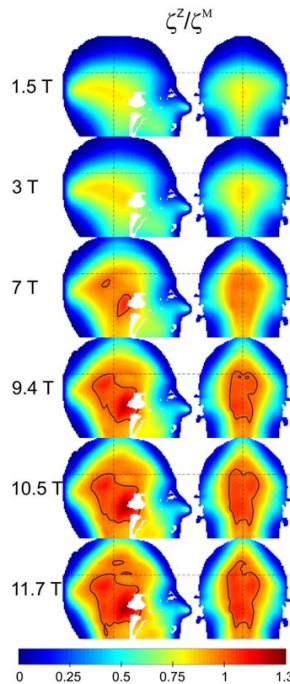
ζ^Z / ζ^M

FIGURE 9 The best possible SNR of Z-directed current patterns (ζ^Z) divided by the best possible SNR of divergence-free current patterns (ζ^M) for a cylindrical surface current distribution. The black contour lines indicate the threshold, where the ratio ζ^Z / ζ^M is larger than one

and hence a linear combination of the two is required to cancel the Φ-component. Another option would be to use vertical loop elements.

5.2 | About the completeness of the VSCH and VCH basis sets

According to the Huygens' field equivalence principle,[50,51] a closed surface current distribution such as on a sphere (VSH) or on an infinitely long cylinder (VCH) forms a complete basis set to calculate the UISNR in the enclosing sample. Unfortunately, a closed spherical surface current distribution is unrealistic, because it does not have an opening for the human neck. Strictly speaking, the spherical cap surface current distribution (VSCH) does not fulfill the conditions of the Huygens' theorem, because it is a non-closed surface. As a consequence, the VSCH basis set is not complete and there are regions in the sample, where the UISNR is underestimated (c.f. Figure 4). However, the figure also demonstrates that an essential underestimation of the UISNR only occurs close to the southern pole. This is due to the absence of generic current patterns in this area. Translating the results of Figure 4 into voxel model Duke, we hypothesize about an underestimation of the UISNR in the brainstem and spinal cord. Notwithstanding the incompleteness of the VSCH basis set, the herein presented UISNR results are ultimate values in terms of the best possible SNR achievable with an open-pole surface current distribution. This ultimate benchmark is directly comparable to the measured SNR of any helmet-shaped receive array.

Also, to calculate the UISNR in the human head, an infinitely long cylindrical surface current distribution is both unrealistic and numerically unstable. The numerical instability is caused by the strong correlation of the resulting electric and magnetic field distributions of the basis vectors: If the current distribution is extending from $z = -\infty$ to $z = +\infty$, the continuous eigenvalues h need to be discretized very densely. However, the smaller the difference Δh between two eigenvectors, the less variation in the electric and magnetic field distributions in a sample of finite length. For this reason, we used a discretization of $\Delta h \approx 21$ 1/m, corresponding to a current distribution extending from $z = -15$ cm to $z = +15$ cm with periodic repetition in z-direction. In this way, the cylindrical surface current patterns were covering the whole head model.

7) with the performance of Z-directed current patterns (Figure 8) reveals, that in those regions of low ζ^M / ζ, the ratio ζ^Z / ζ is high. Hence, Z-directed dipoles are a good choice to complement loop elements on a cylindrical former. There were initial trials to complement loop elements with dipole elements.[7-10] Instead of dipoles, it is also possible to use vertical loop elements.[45-47] These elements have out-of plane currents, which are linearly independent of surface currents and hence add to the overall SNR. At 9.4 T, Avdievich was able to show an SNR boost of approximately 30% in the brain center when combining eight vertical loops with 8 surface loops.[11] This increase is much higher than what could be expected when using 16 surface loops.[48,49] Based on the results of Figure 9, we do not recommend using dipole-only arrays for human head applications below 9.4 T, because Z-directed current patterns result in lower SNR than divergence-free current patterns in most regions of the human head. However, if $B_0 \geq 9.4$ T, dipole-only arrays can outperform loop-only arrays in deep brain regions.

On a helmet-shaped coil holder, loop elements can be complemented by placing additional Θ-directed dipole elements on the spherical surface (Figure 1B).[5] These Θ-directed dipoles are a mixture of both, curl- and divergence-free current patterns. The reason for this is that both curl- and divergence-free VSH have a Φ-component

5.3 | Comparison with other studies

The superlinear increase of the (total) UISNR in a realistic human head model was studied in Ref. 19 by a randomized dipole excitation. The authors reported a sublinear increase of the UISNR for voxels close to the head's surface and a superlinear increase in the center. The linear threshold was at
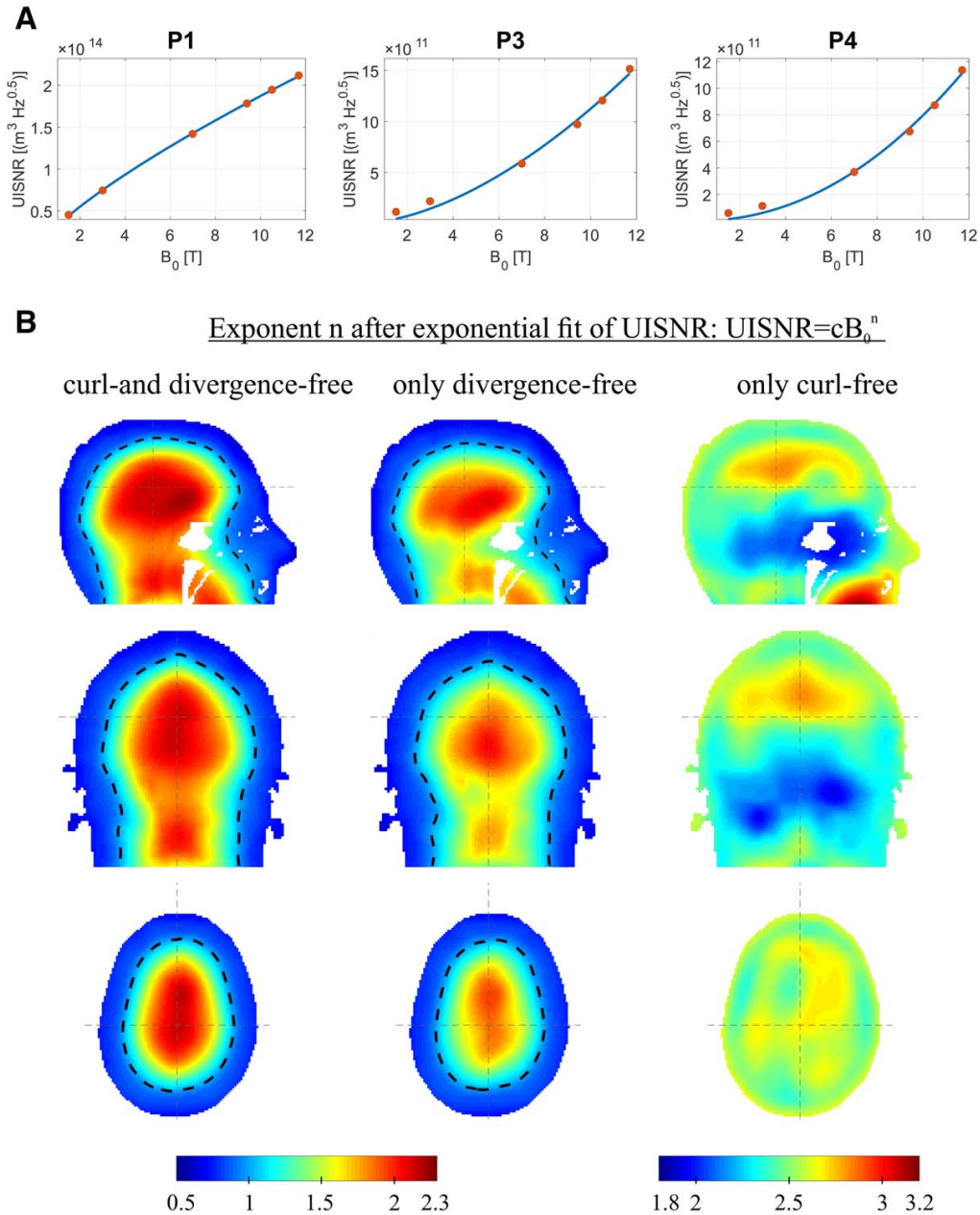
FIGURE 10 The increase of the UISNR in voxel model Duke as a function of B_0 field strength. The UISNR was evaluated with the VSCH basis set. Subfigure (A) shows the UISNR at voxel positions P1, P3, and P4 (s. Figure 2) simulated at 1.5 T, 3 T, 7 T, 9.4 T, 10.5 T, and 11.7 T field strength. An exponential function of the form cB_0^n is fitted to the red datapoints (blue curve). Subfigure (B) visualizes the fitted exponent n regarding the UISNR obtained from curl-and divergence-free current patterns (left column), only divergence-free (middle column) and only curl-free (right column)

about a distance of 1 cm from the skin. In this work, we found the linear threshold in deeper locations about 16–20 mm away from the skin. We believe, this is because the spherical current distribution has a varying distance to the head model (3.1 cm in average), whereas the dipole cloud used in Ref. 19 is conformal to the head shape at a distance

of 3 cm. Pohmann reported a superlinear SNR increase with field strength for the cerebrum.[52] He experimentally measured the SNR at 3 T, 7 T, and 9.4 T with current receive coil arrays and found that in the cerebrum SNR $\propto B_0^{1.65}$. From our simulation studies, we deduce UISNR $\propto B_0^{1.5}$ for the average UISNR in the inner brain region. The comparison of

the UISNR increase of this study with the previously mentioned studies confirms the correctness of our model.

As this work is the first study evaluating ζ^M, ζ^E, ζ^Z, and ζ^Φ in a realistic human head model, we can only compare to results from cylinders and spheres. Regarding the cylindrical Huygens' surface, there are studies for cylinders of human body size: Schnell demonstrated[23] that for a voxel lying on the z-axis of an infinitely long cylinder of 20 cm radius and electric properties of muscle tissue, the ratio ζ^M/ζ is approximately 0.8 at 3 T. In Ref. 22, Lattanzi showed in a similar setup, that central UISNR is dominated by the divergence-free component at 0.2 T and by the curl-free component at 7 T. In Ref. 48, the same author demonstrated ζ^M for various field strengths and sizes of a dielectric cylinder. The results obtained for the realistic head model, suggest a higher SNR performance of divergence-free modes: At 3 T the divergence-free SNR ζ^M is 99% of the total UISNR in the central brain and at 7 T still around 90%. The equivalent cylinder radius circumscribing Duke's head is between 9 and 10 cm and therefore much smaller than body-sized cylinder in the previously mentioned studies. Loop-only arrays on a cylindrical former have higher SNR performance in smaller objects (such as the human head) than in larger samples (such as the human torso).[48] This fact is in line with our findings.

Vaidya investigated the SNR performance of an open-pole 32 channel loop array at 3 T[49] on a spherical Huygens' surface. In a spherical sample of 8.4 cm radius, the unaccelerated SNR performance in the center was not compromised compared to the UISNR. We found the same result when comparing the UISNR of a spherical cap with the UISNR of a completely surrounding surface current distribution (Figure 4). However, the spherical cap design will have lower performance than more encircling designs in the case of parallel imaging. In Ref. 15, we investigated the ratios ζ^M/ζ and ζ^E/ζ at 9.4 T in a spherical phantom of human head size. In Duke, the local SNR performance of loop-only arrays is higher than in the spherical model. The distribution of ζ^M/ζ in Duke is more homogeneous than in the spherical model used in Ref. 15. One reason for this fact is that to calculate the UISNR in Duke, we used an open-pole surface current distribution, whereas a closed surface current distribution was used in Ref. 15. However, when decreasing the cap angle, the minima increase (Figure 5). Another reason explaining this difference is that voxel model Duke is not a homogeneous dielectric and has a different geometry than a simple sphere.

5.4 | Model limitations

Comparing the convergence of the UISNR, in Duke (Figure 2) the UISNR converges more slowly than in the spherical model (Supporting Information Figure S2). This is in agreement with a previous study.[19] The reason for this is, that the voxel model is not symmetric and therefore more basis vectors of the VSCH are required to ensure convergence. We found that the relative change of the UISNR was below 6.3e−10 for all voxel positions and field strengths in the sphere, whereas this value was 6.2e−8 in Duke. These numbers indicate that within the spherical model better convergence could be achieved than in the head model.

All simulations were performed with one particular voxel model ("Duke"). In order to get more general results, several voxel models with different positions could be simulated. Moreover, due to computational limitations, we truncated the voxel model beyond the neck and did not include the shoulders (which are known to influence the RF field of close-by coil elements). This could influence the UISNR in the lower brain regions, such as the cervical spine or the brain stem.

Using a cylindrical coil holder, there is some degree of freedom, where to place the center of the coil with respect to the human head. In this study, we positioned the coordinate center of the cylinder ventrally to the pons (Figure 1C). With this particular positioning, the center of our truncated voxel model was approximately in the $z = 0$ plane of the coordinate system. All results (Figures 7–9) refer to this position. In Supporting Information Figure S14, we demonstrate that by shifting the coordinate center in positive z-direction, the position of maximal ζ^Z/ζ also shifts in positive z-direction, at least at 9.4 T. In general, the UISNR reconstruction for the cylindrical Huygens' surface was more ill-conditioned (i.e., higher condition number of the total noise covariance matrix Ψ) than for the spherical cap Huygens' surface. The cylindrical basis vectors of higher order create highly correlated electric fields within the body model. The reason for this is that a cylindrical Huygen's surface is not very "conformal" to the human head anatomy especially as there is no curvature of the surface toward the head. For this reason we used the Moore-Penrose pseudoinverse in the UISNR reconstruction for the cylindrical Huygens' surface.

By definition the UISNR is only limited by body noise R_{body}. When constructing real array elements, coil noise R_{coil} is inevitable and degrades the SNR performance by a factor $\sqrt{R_{body}/(R_{body}+R_{coil})}$.[53] For example, with body noise being five times higher than the coil noise, SNR is compromised by less than 10%. By translating the SNR performance of curl-and divergence-free current patterns to practical guidelines for RF coil design, we assume all array elements operating in the body noise dominated regime.

REFERENCES

[1] Wiggins GC, Zhang B, Lattanzi R, Chen G, Sodickson D. The electric dipole array: an attempt to match the ideal current pattern for central SNR at 7 Tesla. In Proceedings of the 20th Annual Meeting of ISMRM, Melbourne, Australia, 2012. p. 541.

[2] Chen G, Cloos M, Lattanzi R, Sodickson D, Wiggins G. Bent electric dipoles: a novel coil design inspired by the ideal current pattern for central SNR at 7 Tesla. In Proceedings of the 22nd Annual Meeting of ISMRM, Milan, Italy, 2014. p. 402.

[3] Lagore RL, DelaBarre L, Tian J, Adriany G, Eryaman Y, Vaughan JT. End-loaded dipole array for 10.5T head imaging. In Proceedings of the 24th Annual Meeting of ISMRM, Singapore, 2016. p. 2138.

[4] Tian J, Lagore R, Delabarre L, Vaughan JT. Dipole array design considerations for head MRI at 10.5T. In Proceedings of the 24th Annual Meeting of ISMRM, Singapore, 2016. p. 3524.

[5] Zhang B, Chen G, Cloos M, et al. 29-channel receive-only dense dipole head array for 7T MRI. In Proceedings of the 25th Annual Meeting of ISMRM, Honolulu, HI, 2017. p. 4314.

[6] Oh C, Lee C, Kumar S, et al. Top-hat dipole RF coil with large field of view for 7 T brain MR imaging. In Proceedings of the 25th Annual Meeting of ISMRM, Honolulu, HI, 2017. p. 767.

[7] Wiggins GC, Zhang B, Cloos M, et al. Mixing loops and electric dipole antennas for increased sensitivity at 7 Tesla. In Proceedings of the 21st Annual Meeting of ISMRM, Salt Lake City, UT, 2013. p. 2737.

[8] Eryaman Y, Guerin B, Kosior R, Adalsteinsson E, Wald LL. Combined loop + dipole arrays for 7 T brain imaging. In Proceedings of the 21st Annual Meeting of ISMRM, Salt Lake City, UT, 2013. p. 393.

[9] Chen G, Lakshmanan K, Sodickson D, Wiggins G. A combined electric dipole and loop head coil for 7T head imaging. In Proceedings of the 23rd Annual Meeting of ISMRM, Toronto, Canada, 2015. p. 3133.

[10] Woo MK, Lagore RL, DelaBarre L, et al. A geometrically adjustable loop-dipole (LD) head array for 10.5T. In Proceedings of the 25th Annual Meeting of ISMRM, Honolulu, HI, 2017. p. 1051.

[11] Avdievich NI, Giapitzakis IA, Pfrommer A, Borbath T, Henning A. Combination of surface and 'vertical' loop elements improves receive performance of a human head transceiver array at 9.4 T. *NMR Biomed.* 2018;31:e3878.

[12] Roemer PB, Edelstein WA. Ultimate sensitivity limits of surface coils. In Proceedings of the 6th Annual Meeting of ISMRM, New York, NY, 1987. p. 410.

[13] Wang J, Reykowski A, Dickas J. Calculation of the signal-to-noise ratio for simple surface coils and arrays of coils. *IEEE Trans Biomed Eng.* 1995;42:908-917.

[14] Ocali O, Atalar E. Ultimate intrinsic signal-to-noise ratio in MRI. *Magn Reson Med.* 1998;39:462-473.

[15] Pfrommer A, Henning A. On the contribution of curl-free current patterns to the ultimate intrinsic signal-to-noise ratio at ultra-high field strength. *NMR Biomed.* 2017;30:e3691.

[16] Ohliger MA, Grant AK, Sodickson DK. Ultimate intrinsic signal-to-noise ratio for parallel MRI: electromagnetic field considerations. *Magn Reson Med.* 2003;50:1018-1030.

[17] Felder J, Shah NJ. Ultimate intrinsic signal-to-noise ratio of the human head at 9.4T. In Proceedings of the 19th Annual Meeting of ISMRM, Montréal, Canada, 2011. p. 3878.

[18] Guerin B, Villena JF, Polimeridis AG, et al. Ultimate hyperthermia: computation of the best achievable radio-frequency hyperthermia treatments in non-uniform body models. In Proceedings of the 24th Annual Meeting of ISMRM, Singapore, 2016. p. 351.

[19] Guérin B, Villena JF, Polimeridis AG, et al. The ultimate signal-to-noise ratio in realistic body models. *Magn Reson Med.* 2017; 78:1969-1980.

[20] Guérin B, Villena JF, Polimeridis AG, et al. Computation of ultimate SAR amplification factors for radiofrequency hyperthermia in non-uniform body models: impact of frequency and tumour location. *Int J Hyperth.* 2018;34:87-100.

[21] Wiesinger F, Boesiger P, Pruessmann KP. Electrodynamics and ultimate SNR in parallel MR imaging. *Magn Reson Med.* 2004; 52:376-390.

[22] Lattanzi R, Sodickson DK. Ideal current patterns yielding optimal signal-to-noise ratio and specific absorption rate in magnetic resonance imaging: computational methods and physical insights. *Magn Reson Med.* 2012;68:286-304.

[23] Schnell W, Renz W, Vester M, Ermert H. Ultimate signal-to-noise-ratio of surface and body antennas for magnetic resonance imaging. *IEEE Trans Antennas Propag.* 2000;48:418-428.

[24] Frieze A, Kannan R, Vempala S. Fast Monte-Carlo algorithms for finding low-rank approximations. *J ACM.* 2004;51:1025-1041.

[25] Rokhlin V, Szlam A, Tygert M. A randomized algorithm for principal component analysis. *SIAM J Matrix Anal Appl.* 2010; 31:1100-1124.

[26] Halko N, Martinsson PG, Tropp JA. Finding structure with randomness: probabilistic algorithms for constructing approximate matrix decompositions. *SIAM Rev.* 2011;53:217-288.

[27] Sarkar D, Halas NJ. General vector basis function solution of Maxwell's equations. *Phys Rev E.* 1997;56:1102-1112.

[28] Tai CT. *Dyadic Green Functions in Electromagnetic Theory.* New York: IEEE Press Series on Electromagnetic Waves; 1994.

[29] Moon P, Spencer DE. *Field Theory Handbook.* Berlin: Springer; 1971.

[30] Lattanzi R, Grant AK, Polimeni JR, et al. Performance evaluation of a 32-element head array with respect to the ultimate intrinsic SNR. *NMR Biomed.* 2010;23:142-151.

[31] Hoult DI. The principle of reciprocity in signal strength calculations- a mathematical guide. *Concepts Magn Reson.* 2000;12: 173-187.

[32] Roemer PB, Edelstein WA, Hayes CE, Souza SP, Mueller OM. The NMR phased array. *Magn Reson Med.* 1990;16:192-225.

[33] Hayes CE, Roemer PB. Noise correlations in data simultaneously acquired from multiple surface coil arrays. *Magn Reson Med.* 1990;16:181-191.

[34] Pruessmann KP, Weiger M, Scheidegger MB, Boesiger P. SENSE: sensitivity encoding for fast MRI. *Magn Reson Med.* 1999;42:952-962.

[35] Sodickson DK, Wiggins GC, Chen G, Lakshmanan K, Lattanzi R. More than meets the eye: the mixed character of electric dipole coils, and implications for high-field performance. In Proceedings of the 24th Annual Meeting of ISMRM, Singapore, 2016. p. 389.

[36] Haines GV. Spherical cap harmonic analysis. *J Geophys Res Solid Earth.* 1985;90:2583-2591.

[37] Avdievich NI, Pfrommer A, Giapitzakis IA, Henning A. Analytical modeling provides new insight into complex mutual coupling between surface loops at ultrahigh fields. *NMR Biomed.* 2017; 30:e3759.

[38] Davidson DB. *Computational Electromagnetics for RF and Microwave Engineering*. Cambridge: Cambridge University Press; 2011.

[39] Polimeridis AG, Villena JF, Daniel L, White JK. Stable FFT-JVIE solvers for fast analysis of highly inhomogeneous dielectric objects. *J Comput Phys.* 2014;269:280-296.

[40] Villena JF, Polimeridis AG, Wald LL, Adalsteinsson E, White JK, Daniel L. MARIE – a MATLAB-based open source software for the fast electromagnetic analysis of MRI systems. In Proceedings of the 23rd Annual Meeting of ISMRM, Toronto, Canada, 2015. p. 709.

[41] Villena JF, Polimeridis AG, Eryaman Y, et al. Fast electromagnetic analysis of MRI transmit RF coils based on accelerated integral equation methods. *IEEE Trans Biomed Eng.* 2016;63:2250-2261.

[42] Gabriel S, Lau RW, Gabriel C. The dielectric properties of biological tissues: III. Parametric models for the dielectric spectrum of tissues. *Phys Med Biol.* 1996;41:2271-2293.

[43] Christ A, Kainz W, Hahn EG, et al. The virtual family- development of surface-based anatomical models of two adults and two children for dosimetric simulations. *Phys Med Biol.* 2010;55:N23-N38.

[44] van der Vorst HA. Bi-CGSTAB: a fast and smoothly converging variant of Bi-CG for the solution of nonsymmetric linear systems. *SIAM J Sci Stat Comput.* 1992;13:631-644.

[45] Wang ZJ. Towards a complete coil array. *MRI.* 2008;26:1310-1315.

[46] Wang ZJ. Improving SNR of RF coils using composite coil elements. *NMR Biomed.* 2009;22:952-959.

[47] Maunder A, Fallone BG, Daneshmand M, De Zanche N. Experimental verification of SNR and parallel imaging improvements using composite arrays. *NMR Biomed.* 2015;28:141-153.

[48] Lattanzi R, Wiggins GC, Zhang B, Duan Q, Brown R, Sodickson DK. Approaching ultimate intrinsic signal-to-noise ratio with loop and dipole antennas. *Magn Reson Med.* 2018;79:1789-1803.

[49] Vaidya MV, Sodickson DK, Lattanzi R. Approaching ultimate intrinsic SNR in a uniform spherical sample with finite arrays of loop coils. *Concepts Magn Reson Part B.* 2014;44:53-65.

[50] Schelkunoff SA. Some equivalence theorems of electromagnetics and their applications to radiation problems. *Bell Syst Tech J.* 1936;15:92-112.

[51] Balanis CA. *Antenna Theory Analysis and Design*. Hoboken: Wiley; 2016.

[52] Pohmann R, Speck O, Scheffler K. Signal-to-noise ratio and MR tissue parameters in human brain imaging at 3, 7, and 9.4 Tesla using current receive coil arrays. *Magn Reson Med.* 2016;75: 801-809.

[53] Kumar A, Edelstein WA, Bottomley PA. Noise figure limits for circular loop MR coils. *Magn Reson Med.* 2009;61:1201-1209.

SUPPORTING INFORMATION

Additional Supporting Information may be found online in the supporting information tab for this article.

FIGURE S1. Simulation time for the VSCH basis set (2550 basis vectors).

FIGURE S2. Convergence of the UISNR at six different locations and field strengths for a dielectric sphere of human head size and the analytic VSCH-DGF basis set.

FIGURE S3. Validation of the proposed VSCH-JVIE method: The best possible SNR of divergence-free current modes relative to the UISNR is calculated for a spherical sample with a cap angle of $\vartheta_0 = 120°$. The results obtained by the VSCH-JVIE method are compared to analytic results. The ratio ζ^M/ζ is plotted along the dashed line in figure 3 for different spatial resolutions of the VSCH-JVIE method. The continuous black line is the analytic solution.

FIGURE S4. Comparison of the UISNR results obtained from VSCH-JVIE and a randomized dipole excitation[19]: a) The UISNR ζ as obtained by VSCH-JVIE approach and a randomized dipole excitation for two exemplary field strengths of $B_0 =$ 3 T and 9.4 T. b) The ratios of the UISNR obtained by VSCH-JVIE divided by the UISNR of the randomized dipole approach. c) The increase of the UISNR with field strength in Duke with regard to an exponential model of the form $\zeta = cB_0^n$ for the VSCH-JVIE and the randomized dipole approach.

FIGURE S5. Ideal current patterns on the spherical cap surface loaded by voxel model Duke for voxel P4 (s. figure 2 in the manuscript) at 9.4 T. The divergence-free ($\mathbf{J}^M$) and curl-free ($\mathbf{J}^E$) patterns are plotted separately with a different scaling.

FIGURE S6. Ideal current patterns on the spherical cap surface loaded by voxel model Duke for voxel P2 (s. figure 2 in the manuscript) at 1.5 T.

FIGURE S7. Ideal current patterns on the spherical cap surface loaded by voxel model Duke for voxel P4 (s. figure 2 in the manuscript) at 1.5 T.

FIGURE S8. Ideal current patterns on the spherical cap surface loaded by voxel model Duke for voxel P5 (s. figure 2 in the manuscript) at 1.5 T.

FIGURE S9. Ideal current patterns on the spherical cap surface loaded by voxel model Duke for voxel P2 (s. figure 2 in the manuscript) at 9.4 T.

FIGURE S10. Ideal current patterns on the spherical cap surface loaded by voxel model Duke for voxel P4 (s. figure 2 in the manuscript) at 9.4 T.

FIGURE S11. Ideal current patterns on the spherical cap surface loaded by voxel model Duke for voxel P5 (s. figure 2 in the manuscript) at 9.4 T.

FIGURE S12. Ideal current patterns on the cylindrical surface loaded by voxel model Duke for voxel P4 (s. figure 2 in the manuscript) at 9.4 T. The divergence-free ($\mathbf{J}^{M}$) and curl-free ($\mathbf{J}^{E}$) patterns are plotted separately with a different scaling.

FIGURE S13. Ideal current patterns on the cylindrical surface loaded by voxel model Duke for voxel P4 (s. figure 2 in the manuscript) at 9.4 T. The Z-directed ($\mathbf{J}^{Z}$) and Φ-directed ($\mathbf{J}^{\Phi}$) patterns are plotted separately with a different scaling.

FIGURE S14. Influence of the coordinate system on ζ^{M} and ζ^{Z}. At position 2, the coordinate center is offset by 2.3 cm in foot-head direction relative to position 1. Position 1 is the same location, as described in the manuscript. a) The best possible SNR of divergence-free and Z-directed currents relative to the UISNR for a field strength of 9.4 T. b) To demonstrate differences between the two positions, we plotted the ratios of the corresponding SNR maps in a).

PUBLICATION 3

On the Superlinear Increase of the Ultimate Intrinsic Signal-to-Noise Ratio with Regard to Main Magnetic Field Strength in a Spherical Sample

A. Pfrommer[1]   A. Henning[2,3]

Abstract – In this study, the increase of the ultimate intrinsic signal-to-noise ratio (UISNR) with regard to main magnetic field strength B_0 is investigated. A simplified spherical phantom of human head size is used. In the center of the sphere, the UISNR grows more than quadratically. Within the volume, in which the distance to the center is smaller than 85% of the sphere's radius, the UISNR increases superlinearly. At the surface, the UISNR grows only sublinearly. The SNR of curl-free current patterns grows more than cubically in the center, whereas the SNR of divergence-free current patterns increases quadratically. However, this does not imply, that curl-free modes result in higher SNR than divergence-free modes.

1   INTRODUCTION

Ultra-high field magnetic resonance imaging (MRI) is motivated by the increase of the signal-to-noise ratio (SNR) with static magnetic field strength B_0. Under quasistatic conditions, i.e. the electromagnetic wavelength at the Lamor frequency in tissue is much larger than the dimension of the human body, SNR increases linearly with B_0 [1,2]. However, with increasing B_0, the wavelength in the human body gets smaller and the quasistatic assumption is no longer valid. Various studies reported a superlinear increase of SNR with field strength [3-6]. In [3], Wiesinger used a spherical model and published exponents describing the growth of the ultimate intrinsic SNR (UISNR) as a power of B_0. His analysis was limited to three voxel positions (center, intermediate, and periphery) and he did not investigate the growth of curl- and divergence-free modes separately. Without explicitly giving exponents, the work of Lattanzi [4] includes a similar analysis than [3]. In [5], Pohmann experimentally measured the B_0-dependent SNR increase in vivo with current receive coil technology. Recently, Guérin simulated the UISNR at different field strengths in a realistic human body model [6]. He fitted the UISNR at four different voxel positions and for gray- and white matter averages to a quadratic model.

In this study, we systematically investigated the superlinear behavior of the UISNR in a simplified spherical model. We used a power series model for the fitting and evaluated the exponent with full spatial coverage over the entire sphere. Additionally, we studied the B_0-dependent SNR increase for divergence-free and curl-free modes separately.

2   METHODS

To calculate the UISNR in the human head, we use a basis set of vector spherical harmonics (VSH) in a spherical phantom of human head size. The basis set consists of divergence-free (denoted with superscript M) and curl-free (denoted with superscript E) modes, which complement each other. In total we use N basis vectors with N being sufficiently large to ensure convergence. The unaccelerated UISNR ζ at position r can be evaluated according to the following equation [7]:

$$\zeta(\boldsymbol{r}) = \omega_0 M_0 \frac{\sqrt{\boldsymbol{S}^H(\boldsymbol{r})\boldsymbol{\Psi}^{-1}\boldsymbol{S}(\boldsymbol{r})}}{\sqrt{4k_B T}}. \tag{1}$$

The term k_B is the Boltzmann constant, T is the absolute temperature of the sample, ω_0 the Lamor frequency and M_0 the equilibrium magnetization. Both, ω_0 and M_0 are proportional to B_0 (we used the gyromagnetic ratio of 1H in this work). The receive sensitivity vector $\boldsymbol{S}$ has dimension of Nx1 and represents the complex left-handed component of the circularly polarized RF magnetic field. It consists of both, curl- and divergence-free sensitivities:

$$\boldsymbol{S} = \begin{pmatrix} \boldsymbol{S}^{\mathrm{M}} \\ \boldsymbol{S}^E \end{pmatrix}. \tag{2}$$

The noise covariance matrix $\boldsymbol{\Psi}$ has size NxN and has the following structure:

$$\boldsymbol{\Psi} = \begin{pmatrix} \boldsymbol{\Psi}^M & \mathbf{0} \\ \mathbf{0} & \boldsymbol{\Psi}^E \end{pmatrix}. \tag{3}$$

Note, that the off-diagonal elements are zero. In a spherical sample, divergence-free and curl-free modes are decoupled. The SNR of divergence-free modes can be calculated by using only $\boldsymbol{S}^{\mathrm{M}}$ and $\boldsymbol{\Psi}^M$ in equation (1). Analogously, the SNR of curl-free modes is calculated by using only $\boldsymbol{S}^{\mathrm{E}}$ and $\boldsymbol{\Psi}^E$ in equation (1).

2.1   UISNR in a Spherical Phantom

First, we approximated the human head with a uniform dielectric sphere of radius 9.2 cm. Table 1 lists the electromagnetic properties of the sphere, which were chosen as average values of gray and

[1] High-field Magnetic Resonance Center, Max Planck Institute for Biological Cybernetics Tuebingen, Spemannstrasse 41, 72076 Tuebingen, Germany, e-mail: andreas.pfrommer@tuebingen.mpg.de, tel.: +49 7071 601 918, fax: +49 7071 601 702.
[2] High-field Magnetic Resonance Center, Max Planck Institute for Biological Cybernetics Tuebingen, Spemannstrasse 41, 72076 Tuebingen, Germany, e-mail: anke.henning@tuebingen.mpg.de, tel.: +49 7071 601 723, fax: +49 7071 601 702.
[3] Institute of Physics, Ernst-Moritz-Arndt University Greifswald, Felix-Hausdorff-Strasse 6, 17489 Greifswald, Germany, e-mail: anke.henning@physik.uni-greifswald.de, tel.: +49 3834 420 4743, fax: +49 3834 86 4701.

white matter according to the Gabriel database [8]. The generic VSH surface current patterns were also running on a spherical surface at a distance of 12.2 cm from the coordinate center (s. Figure 1). An analytic expression for the receive sensitivity vector $\boldsymbol{S}$ is given in equations 18, 19 and 20 in [9] (set the coefficients V^M and V^E to one). Moreover the noise covariance matrix can be calculated with the help of equations 24, 25 and 26 in [9] (set the coefficients V^M and V^E to one). To do the numeric evaluation of the analytic formulas, we used a spatial grid of 2 mm resolution and the maximum order of the VSH was set to 30. This resulted in N=1920 basis vectors.

B_0 [T]	conductivity [S/m]	relative permittivity
1.5	0.40	82.7
3	0.46	63.1
7	0.55	52.0
9.4	0.59	49.8
10.5	0.61	49.1
11.7	0.63	48.4

Table 1: Electromagnetic properties of the spherical model.

2.2 Fitting procedure

We evaluated the unaccelerated UISNR at 1.5 T, 3 T, 7 T, 9.4 T, 10.5 T and 11.7 T in all voxel positions within the sample. Afterwards, we fitted for every voxel position $\boldsymbol{r}$ the simulated UISNR data points to a power series model of the form

$$\zeta(B_0, \boldsymbol{r}) = c_{\boldsymbol{r}} B_0^{n_{\boldsymbol{r}}}. \qquad (4)$$

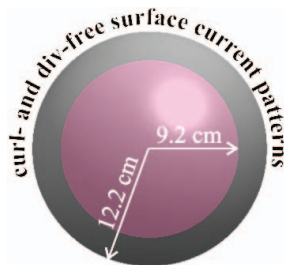We used MATLAB's fit- function routine with the model type "power1".

Figure 1: Simulation setup for dielectric sphere.

3 RESULTS

Figure 2 visualizes the UISNR in the spherical sample at different field strengths in the plane y=0. Due to the large dynamic range of the UISNR, the plots are in logarithmic scale. The first column is the UISNR of a complete basis set of curl- and divergence-free current patterns. By definition, this is the best SNR that is achievable in the spherical sample. The SNR generated with only divergence-free (second column) or curl-free (third column) current patterns is always lower. This is true for all field strengths.

Obviously, the UISNR increases strictly monotonically with B_0. Qualitatively, from figure 2 we see, that central UISNR grows faster with B_0 than peripheral UISNR. Moreover, the right column in Figure 2 reveals that the SNR obtained with curl-free current patterns is much lower at 1.5 T and 3 T compared to divergence-free current patterns. The same is true for peripheral and central regions at ultra-high field strength (7 T-11.7 T). In the intermediate region (between center and periphery in z-direction), the SNR of curl-free modes is about 90% (at 7 T) to 135% (at 11.7 T) of the SNR of divergence-free modes.

Figure 3 illustrates, that the growth of UISNR with B_0 depends on the voxel position: When fitting the power series model from equation (4) to the simulated curves, the exponent n is 2.14, 2.01 and 0.88 at the center, half radius away from the center and in the periphery.

Figure 4 shows the spatial distribution of the fitted exponent n of the power series model. For all voxel positions, the coefficient of determination (R^2) of the fit was larger than 0.99. Figure 4a) shows the UISNR increase when a complete basis set is used. As a general result, we want to state, that the value of the exponent n depends on position. In the peripheral region of the head-sized sphere, the UISNR increase was less than linear with field strength B_0. The linear threshold was about 1.4 cm away from the sample surface. The SNR in all voxels lying innermost to the dashed line grows faster than linear with field strength. In the central region of the sphere, the UISNR increase is more than quadratic (n_{max}=2.21).

It is interesting to investigate the SNR increase for divergence-free and curl-free modes separately. Figure 4b) demonstrates, that the increase in SNR with only divergence-free modes is very similar to the complete basis set. However, Figure 4c) reveals, that the SNR obtained from curl-free modes grows much faster than the previously discussed two cases. We found a more than quadratic increase at the periphery and more than cubic in the center.

4 DISCUSSION

We have shown that the increase of the UISNR with B_0 depends on the voxel position. In a head-sized spherical phantom, voxels lying within 85% of the sphere's radius, have a superlinear increase of the UISNR with field strength. Moreover, the SNR generated by curl-free current patterns only, grows much faster, than the SNR generated by divergence-free current patterns only. Nevertheless, it is very important to emphasize, that this does not mean, that the SNR generated by curl-free modes is higher than the SNR of divergence-free modes. Figure 2 demonstrates, that at low field strength (1.5 T and 3 T) and in the periphery and center at high field strength ($B_0 \geq 7$ T), curl-free modes result in much lower SNR than divergence-free modes. Contrary, in the intermediate region at high field strength, curl-free modes achieve higher SNR than divergence-free modes.

The results of this work are in accordance to other studies about the superlinear increase of the UISNR in spherical models: In [3], Wiesinger reported an exponent n of 1.92, 2.05 and 0.9 for a 30cm- diameter sphere in a central, intermediate and peripheral voxel position. Both, Lattanzi [4] and Guérin [6] demonstrated a superliner increase in the center of a head-sized sphere and sublinear increase in the periphery.

Translating the results of the spherical model to the human head, we expect a superlinear increase of the UISNR in the cerebrum and a sublinear increase in the skull. Indeed, Pohmann experimentally demonstrated, that SNR grows with n=1.65 in the cerebrum [5]. This motivates the implementation of functional or spectroscopic NMR applications in the human brain at ultra-high field strength.

In order to reach the theoretically predicted superlinear SNR increase with field strength, practical receive arrays need to be sample loss dominated. This is the most important design criterion, because the UISNR is only limited by sample losses. Additionally, to reach the UISNR at all voxel positions, a combination of curl- and divergence-free elements needs to be used [9]. In practice, this can be accomplished by adding dipole or vertical elements to the receive loops.
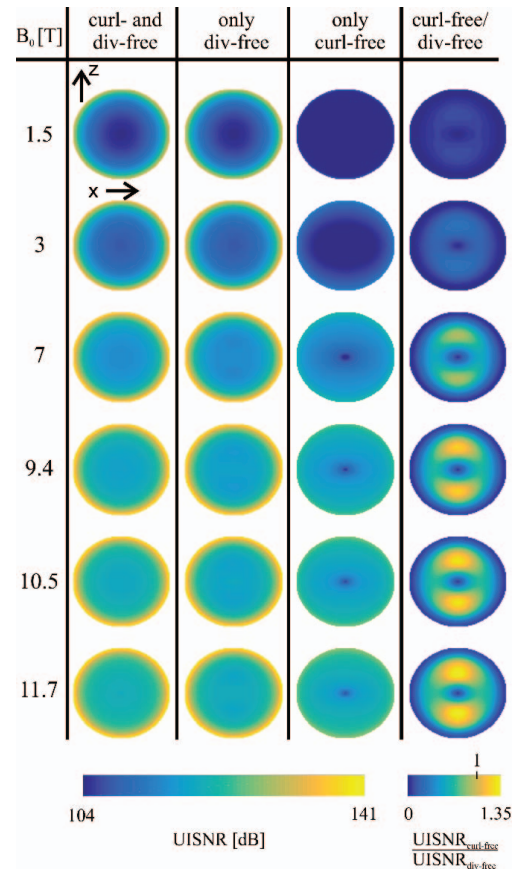

Figure 2: The UISNR for protons (1H) in a homogeneous dielectric sphere of human head size and different field strengths of 1.5 T (64 MHz), 3 T (128 MHz), 7 T (298 MHz), 9.4 T (400 MHz), 10.5 T (447 MHz) and 11.7 T (498 MHz). The left column represents the UISNR of a complete basis set of curl- and div-free current patterns, the middle columns the UISNR of div-free and curl-free modes and the right column the ratio of the UISNR of curl- and divergence-free modes.
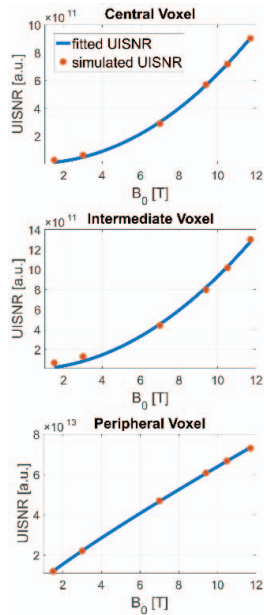
Figure 3: UISNR at different field strengths for central, intermediate and peripheral voxel positions. The voxels are indicated in Figure 4.
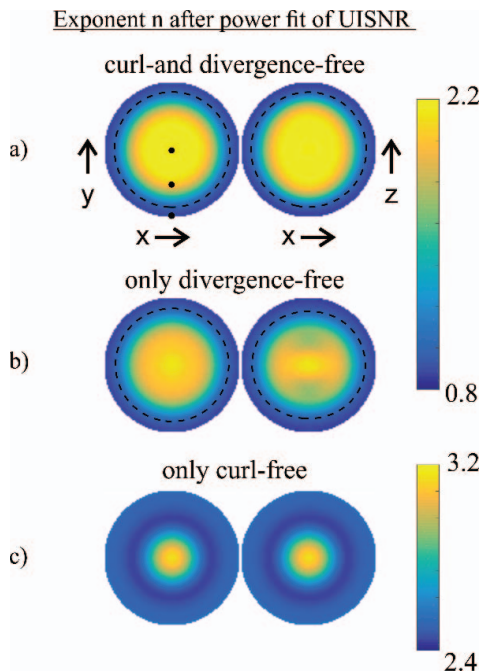

Figure 4: Spatial distribution of the exponent *n* of the power series model. The linear threshold is indicated with a dashed line.

References

[1] D. Hoult. "The Sensitivity of the Zeugmatographic Experiment Involving Human Samples", *Journal of Magnetic Resonance*, vol 34, pp. 425-433, 1979.

[2] T. Redpath. "Signal-to-noise ratio in MRI", *The British Journal of Radiology*, vol 71, pp. 704-707, 1998.

[3] F. Wiesinger, P. Boesiger, and K. Pruessmann. "Electrodynamics and Ultimate SNR in Parallel MR Imaging", *Magnetic Resonance in Medicine*, vol 52, pp. 376-390, 2004.

[4] R. Lattanzi, and D. Sodickson. "Ideal Current Patterns Yielding Optimal Signal-to-Noise Ratio and Specific Absorption Rate in Magnetic Resonance Imaging: Computational Methods and Physical Insights", *Magnetic Resonance in Medicine*, vol 68, pp. 286-304, 2012.

[5] R. Pohmann, O. Speck, and K. Scheffler. "Signal-to-Noise Ratio and MR Tissue Parameters in Human Brain Imaging at 3, 7, and 9.4 Tesla Using Current Receive Coil Arrays", *Magnetic Resonance in Medicine*, vol 75, pp. 801-809, 2016.

[6] B. Guérin, J. Villena, A. Polimeridis, E. Adalsteinsson, L. Daniel, J. White, and L. Wald. "The Ultimate Signal-to-Noise Ratio in Realistic Body Models", *Magnetic Resonance in Medicine*, doi:10.1002/mrm.26564.

[7] R. Lattanzi, A. Grant, J. Polimeni, M. Ohliger, G. Wiggins, L. Wald, and D. Sodickson. "Performance evaluation of a 32-element head array with respect to the ultimate intrinsic SNR", *NMR in Biomedicine*, vol 23, pp. 142-151, 2010.

[8] S. Gabriel, R. Lau and C. Gabriel. "The dielectric properties of biological tissues: III. Parametric models for the dielectric spectrum of tissues", *Physics in Medicine and Biology,* vol 41, pp. 2271-2293, 1996.

[9] A. Pfrommer, and A. Henning. "On the Contribution of Curl-Free Current Patterns to the Ultimate Intrinsic Signal-to-Noise Ratio at Ultra-High Field Strength", *NMR in Biomedicine* , doi:10.1002/nbm.3691.

Publication 4

WILEY **NMR** IN BIOMEDICINE

RESEARCH ARTICLE

Analytical modeling provides new insight into complex mutual coupling between surface loops at ultrahigh fields

N. I. Avdievich[1,2] ⓘ | A. Pfrommer[1] | I. A. Giapitzakis[1] | A. Henning[1,2]

[1] High-Field MR Center, Max Planck Institute for Biological Cybernetics, Tübingen, Germany

[2] Institute of Physics, Ernst-Moritz-Arndt University Greifswald, Greifswald, Germany

Correspondence
N. I. Avdievich, High-Field MR Center, Max Planck Institute for Biological Cybernetics, 72076 Tübingen, Germany.
Email: nikolai.avdievitch@tuebingen.mpg.de

Ultrahigh-field (UHF) (≥7 T) transmit (Tx) human head surface loop phased arrays improve both the Tx efficiency ($B_1^+/\sqrt{P}$) and homogeneity in comparison with single-channel quadrature Tx volume coils. For multi-channel arrays, decoupling becomes one of the major problems during the design process. Further insight into the coupling between array elements and its dependence on various factors can facilitate array development. The evaluation of the entire impedance matrix Z for an array loaded with a realistic voxel model or phantom is a time-consuming procedure when performed using electromagnetic (EM) solvers. This motivates the development of an analytical model, which could provide a quick assessment of the Z-matrix. In this work, an analytical model based on dyadic Green's functions was developed and validated using an EM solver and bench measurements. The model evaluates the complex coupling, including both the electric (mutual resistance) and magnetic (mutual inductance) coupling. Validation demonstrated that the model does well to describe the coupling at lower fields (≤3 T). At UHFs, the model also performs well for a practical case of low magnetic coupling. Based on the modeling, the geometry of a 400-MHz, two-loop transceiver array was optimized, such that, by simply overlapping the loops, both the mutual inductance and the mutual resistance were compensated at the same time. As a result, excellent decoupling (below −40 dB) was obtained without any additional decoupling circuits. An overlapped array prototype was compared (signal-to-noise ratio, Tx efficiency) favorably to a gapped array, a geometry which has been utilized previously in designs of UHF Tx arrays.

KEYWORDS

analytical model, array optimization, decoupling, impedance matrix, transceiver arrays, ultrahigh-field MRI

1 | INTRODUCTION

Ultrahigh-field (UHF) (≥7 T) transmit (Tx)[1,2] and transceiver[1,3-6] human head radiofrequency (RF) surface loop phased arrays improve both the Tx efficiency ($B_1^+/\sqrt{P}$) and homogeneity in comparison with single-channel quadrature Tx volume coils.[4,7,8] Further enhancement in both Tx performance (efficiency, parallel transmission) and receive (Rx) performance [signal-to-noise ratio (SNR), parallel imaging] can be achieved by increasing the number of array elements. Tx arrays with an element count of up to 32 have been developed and evaluated for the imaging of human heads.[1] For such densely populated arrays, decoupling (canceling the cross-talk between the array elements) becomes one of the major problems because of the necessity of using a very large number of adjustable decoupling circuits. For example, a 16-element, two-row (2 × 8) head transceiver array may have up to 40 circuits connecting each pair of adjacent elements.[4] When strong cross-talk between non-adjacent elements also necessitates decoupling,[9] an even larger number of decoupling circuits is required. The growing complexity of the array's decoupling network implies that new methods of decoupling must be developed and existing methods must be improved. Further insight into the coupling between array elements and its dependence on various factors, e.g. the array geometry, resonance frequency, sample positioning and properties, can facilitate such

---

N. I. Avdievich and A. Pfrommer contributed equally to this work

Abbreviations used: AFI, actual flip angle imaging; CP, circular polarized; EM, electromagnetic; GRE, gradient echo imaging; ID, internal diameter; RF, radiofrequency; Rx, receive; SNR, signal-to-noise ratio; SoS, sum-of-squares; TD, transformer decoupling; Tx, transmit; UHF, ultrahigh field

---

development. It is worth noting that not only the reactive coupling L_{12} (mutual inductance), but also the resistive coupling R_{12} (mutual resistance), must be taken into account. For example, phased arrays with overlapped loops improve both the SNR and B_1^+ distributions when compared with gapped arrays by eliminating voids in the gap area and providing a larger penetration depth. However, overlapping is often associated with a large intrinsic R_{12}, e.g. up to ~0.5–0.6 at 3 T.[10-12] This corresponds to a residual coupling of approximately −10 to −12 dB, which is generally insufficient for the decoupling of multi-row Tx arrays. Therefore, UHF head transceiver and Tx arrays are also commonly constructed using non-overlapping loops.[2,4-6]

The evaluation of the entire impedance matrix Z for an array loaded with a realistic voxel model or phantom is a very time-consuming procedure when performed using electromagnetic (EM) solvers (REMCOM, CST, etc.). This motivates the development of an analytical model which could provide a quick assessment of the array Z-matrix. Such a model would aid in finding a solution for a simplified array geometry and phantom, which could then be refined for a realistic array design and a voxel model by using more accurate, albeit much slower, solvers. To evaluate EM fields in a human head at frequencies above 30–40 MHz, full-wave calculations (no quasi-static approximation) must be used. In the past, several groups have developed analytical models using dyadic Green's functions for the calculation of EM fields in lossy samples. Vesselle and Collin[13,14] developed a theory to calculate the SNR of a surface loop loaded by an infinitely long cylinder, a geometry approximating a human head or body. However, the authors did not investigate the coupling between a pair of loops. Using the same approach, Schnell et al.[15] later dealt with the ultimate intrinsic SNR in a homogeneous cylinder and described, *inter alia*, the noise correlation of a cylindrical surface current distribution. Searching for ideal current patterns that yielded optimal SNR, Lattanzi and Sodickson[16] described the expansion coefficients of a rectangular window coil using the same basis functions as in Schnell et al.[15] Again, the authors did not evaluate the Z-matrix. In Wright,[11] the author also performed a full-wave analysis of two planar loops loaded by an infinite half-plane of lossy dielectric material. Using the reaction theorem and the framework of dyadic Green's functions in the spectral domain, the Z-matrix was then calculated. However, the author only considered planar surface loops and the analysis was limited to a frequency of 63 MHz.

In this work, we use dyadic Green's functions to calculate the impedance matrix and mutual coupling between two rectangular loops placed on a cylindrical surface and loaded with a cylindrical phantom. In contrast with the work in Wright,[11] where the impedance matrix of two planar loops, loaded by an infinite half-space, was calculated, we present for the first time, to the best of our knowledge, analytical modeling of the impedance matrix of two loaded rectangular loops placed on a cylindrical surface and mimicking a geometry of loops in a head phased array. First, we validate the analytical results using an EM solver and bench measurements. Then, using the analytical model, we examine the dependence of the coupling between the two loops on the angle between them, the resonance frequency, the loop size and the distance to the sample. Finally, we demonstrate that, by using our model, the geometry of a 9.4-T (400-MHz) two-loop transceiver array can be optimized, such that, by simply overlapping the loops, both the mutual inductance and the mutual resistance can be compensated at the same time. An optimized overlapped array prototype was compared (SNR, Tx efficiency) with a gapped array, which has been utilized previously in designs of UHF Tx arrays.[2,4-6]

2 | METHODS

2.1 | Analytical model

We can describe the EM field problem of two rectangular surface loops irradiating an infinitely long cylindrical sample by a two-layered analytical model (Figure 1). All mathematical symbols used in this work are summarized in Supporting Information Table **S1**. For the dielectric cylinder, we set the permittivity ε_r, conductivity σ and radius a. The geometric parameters for the two equidimensional surface loops include their width, determined by an angle $2\phi_0$, their distance to the center axis b and their length $2d$. The centers of the loops are separated by an angle α. We were interested in the two-port impedance matrix of this configuration. Using the reaction theorem,[17] each element Z_{ij} of the two-port impedance matrix Z can be expressed as:

$$Z_{ij} = \frac{-1}{I_i I_j} \iiint_V E_j \cdot J_i dV \ V \in \text{coil } i \tag{1}$$

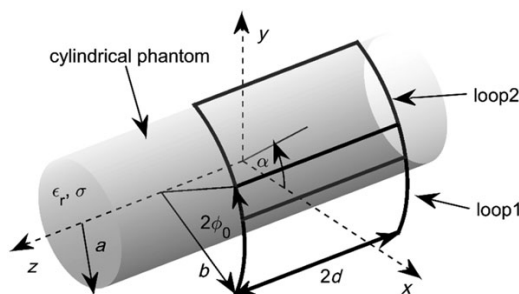**FIGURE 1** Two-loop cylindrical setup for the analytical model

where $\boldsymbol{E}_j$ is the electric field caused by a current density $\boldsymbol{J}_j$ flowing in loop j and $\boldsymbol{J}_i$ is the current density in loop i. It should be noted that, within this model, the two current distributions $\boldsymbol{J}_i$ and $\boldsymbol{J}_j$ are treated as independent from each other. For simplicity, we assume a uniform current distribution of magnitude $I_{i,j}$ along the loop conductor and a time harmonic dependence $e^{-i\omega t}$. Any closed-loop surface current distribution $\boldsymbol{K}$ flowing on a cylinder of radius b can be expanded into an infinite series of vector cylindrical harmonics:

$$\boldsymbol{K} = I \sum_{n=-\infty}^{\infty} \int_{-\infty}^{\infty} dh \; w_n^M(h) \boldsymbol{C}_n(h) \tag{2}$$

The vector cylindrical harmonic is defined as $\boldsymbol{C}_n(h) = \nabla \times e^{in\varphi} e^{ihz} \boldsymbol{e}_r$. We use standard cylindrical coordinates with unit radial vector $\boldsymbol{e}_r$, polar angle $\varphi \in (0, 2\pi)$ and $z \in (-\infty, +\infty)$. The imaginary unit is denoted as $i = \sqrt{-1}$. The variable h is a spatial frequency and the integral expression in Equation 2 is the Fourier transform of a rectangular window loop. The expansion coefficients for the given rectangular window loops with their center at an angle α from the positive x axis can be calculated as:[15,16]

$$w_n^{M_{1,2}}(h) = \frac{\sin(hd)}{\pi h} \cdot \frac{\sin(n\phi_0)}{\pi n} e^{-in\alpha_{1,2}} \tag{3}$$

In order to obtain the mutual impedance Z_{12} between the two loops, according to Equation 1, knowledge of the electric field $\boldsymbol{E}_2$, which is generated by the second loop in the outer vacuum layer, is needed. For a full-wave solution of $\boldsymbol{E}_2$, the framework of dyadic Green's functions was applied.[18] After using the orthogonality relations for vector cylindrical harmonics, we obtain:

$$\boldsymbol{E}_2(\boldsymbol{r}) = iI_2 \frac{\omega\mu_0\pi}{2} \int_{-\infty}^{\infty} dh \sum_{n=-\infty}^{\infty} \frac{w_n^{M_2}(h)}{\eta_0^2} \left(V^{M1} \boldsymbol{M}^{(1)}(\eta_0, \boldsymbol{r}) + V^M \boldsymbol{M}(\eta_0, \boldsymbol{r}) + V^{N1} \boldsymbol{N}^{(1)}(\eta_0, \boldsymbol{r}) + V^N \boldsymbol{N}(\eta_0, \boldsymbol{r}) \right) \tag{4}$$

The functions $\boldsymbol{M}^{(1)}$, $\boldsymbol{M}$, $\boldsymbol{N}^{(1)}$ and $\boldsymbol{N}$ are fundamental solutions to the homogeneous Helmholtz equation in cylindrical coordinates:

$$\begin{aligned}
\boldsymbol{M}(\eta_0, \boldsymbol{r}) &= \nabla \times \left(J_n(\eta_0 r) e^{in\varphi} e^{ihz} \boldsymbol{e}_z \right) \\
\boldsymbol{M}^{(1)}(\eta_0, \boldsymbol{r}) &= \nabla \times \left(H_n^{(1)}(\eta_0 r) e^{in\varphi} e^{ihz} \boldsymbol{e}_z \right) \\
\boldsymbol{N}(\eta_0, \boldsymbol{r}) &= \frac{1}{k_0} \nabla \times \boldsymbol{M}(\eta_0, \boldsymbol{r}) \\
\boldsymbol{N}^{(1)}(\eta_0, \boldsymbol{r}) &= \frac{1}{k_0} \nabla \times \boldsymbol{M}^{(1)}(\eta_0, \boldsymbol{r})
\end{aligned} \tag{5}$$

We use the Bessel function J_n and Hankel function of first kind $H_n^{(1)}$. The complex wave number in the cylinder is $k = \omega\sqrt{\mu_0\varepsilon_0\varepsilon_r + i\sigma\mu_0/\omega}$ and, in a vacuum, we obtain $k_0 = \omega\sqrt{\mu_0\varepsilon_0}$. The propagation constant in the r direction is $\eta_0^2 = k_0^2 - h^2$ in a vacuum and $\eta^2 = k^2 - h^2$ inside the sample. The remaining expansion coefficients stem from the evaluation of the orthogonality relation at $r = b$ and must be incorporated into the solution of $\boldsymbol{E}_2$:

$$\begin{aligned}
V^{M1} &= \widetilde{A}hb\frac{\partial}{\partial r}H_n^{(1)}(\eta_0 r)\Big|_{r=b} + \widetilde{D}nk_0 H_n^{(1)}(\eta_0 b) \\
V^M &= hb\frac{\partial}{\partial r}H_n^{(1)}(\eta_0 r)\Big|_{r=b} \\
V^{N1} &= \widetilde{B}hb\frac{\partial}{\partial r}H_n^{(1)}(\eta_0 r)\Big|_{r=b} + \widetilde{C}nk_0 H_n^{(1)}(\eta_0 b) \\
V^N &= nk_0 H_n^{(1)}(\eta_0 b)
\end{aligned} \tag{6}$$

The coefficients $\widetilde{A}, \widetilde{B}, \widetilde{C}$ and $\widetilde{D}$ originate directly from the general boundary conditions of the underlying Green's functions at $r = a$. Therefore, the following linear system of equations must be solved:

$$
\begin{pmatrix}
0 & -\dfrac{\eta_0^2}{k_0}H_n^{(1)}(\eta_0 a) & 0 & \dfrac{\eta^2}{k}J_n(\eta a) \\[2mm]
-\dfrac{\partial}{\partial r}H_n^{(1)}(\eta_0 r)\Big|_{r=a} & -\dfrac{nh}{k_0 a}H_n^{(1)}(\eta_0 a) & \dfrac{\partial}{\partial r}J_n(\eta r)\Big|_{r=a} & \dfrac{nh}{ka}J_n(\eta a) \\[2mm]
-\eta_0^2 H_n^{(1)}(\eta_0 a) & 0 & \eta^2 J_n(\eta a) & 0 \\[2mm]
-\dfrac{nh}{a}H_n^{(1)}(\eta_0 a) & -k_0\dfrac{\partial}{\partial r}H_n^{(1)}(\eta_0 r)\Big|_{r=a} & \dfrac{nh}{a}J_n(\eta a) & k\dfrac{\partial}{\partial r}J_n(\eta r)\Big|_{r=a}
\end{pmatrix}
\begin{pmatrix}\widetilde{A}\\ \widetilde{B}\\ \widetilde{a}\\ \widetilde{b}\end{pmatrix}
=
\begin{pmatrix}
0 \\[2mm]
\dfrac{\partial}{\partial r}J_n(\eta_0 r)\Big|_{r=a} \\[2mm]
\eta_0^2 J_n(\eta_0 a) \\[2mm]
\dfrac{nh}{a}J_n(\eta_0 a)
\end{pmatrix}
$$

$$
\begin{pmatrix}
-\dfrac{\eta_0^2}{k_0}H_n^{(1)}(\eta_0 a) & 0 & \dfrac{\eta^2}{k}J_n(\eta a) & 0 \\[2mm]
-\dfrac{nh}{k_0 a}H_n^{(1)}(\eta_0 a) & -\dfrac{\partial}{\partial r}H_n^{(1)}(\eta_0 r)\Big|_{r=a} & \dfrac{nh}{ka}J_n(\eta a) & \dfrac{\partial}{\partial r}J_n(\eta r)\Big|_{r=a} \\[2mm]
0 & -\eta_0^2 H_n^{(1)}(\eta_0 a) & 0 & \eta^2 J_n(\eta a) \\[2mm]
-k_0\dfrac{\partial}{\partial r}H_n^{(1)}(\eta_0 r)\Big|_{r=a} & -\dfrac{nh}{a}H_n^{(1)}(\eta_0 a) & k\dfrac{\partial}{\partial r}J_n(\eta r)\Big|_{r=a} & \dfrac{nh}{a}J_n(\eta a)
\end{pmatrix}
\begin{pmatrix}\widetilde{C}\\ \widetilde{D}\\ \widetilde{c}\\ \widetilde{d}\end{pmatrix}
=
\begin{pmatrix}
\dfrac{\eta_0^2}{k_0}J_n(\eta_0 a) \\[2mm]
\dfrac{nh}{k_0 a}J_n(\eta_0 a) \\[2mm]
0 \\[2mm]
k_0\dfrac{\partial}{\partial r}J_n(\eta_0 r)\Big|_{r=a}
\end{pmatrix}
$$

(7)

Again, we make use of the orthogonality of the cylindrical harmonics and end up with:

$$
Z_{12} = 2\omega\mu_0\pi^3\int_{-\infty}^{\infty}dh\sum_{n=-\infty}^{\infty}\frac{1}{\eta_0^2}w_{-n}^{M_1}(-h)w_n^{M_2}(h)\Big(V^{N1}nk_0H_n^{(1)}(\eta_0 b) + V^N nk_0 J_n(\eta_0 b) +
$$
$$
...V^{M1}hb\frac{\partial}{\partial r}H_n^{(1)}(\eta_0 r)\Big|_{r=b} + V^M hb\frac{\partial}{\partial r}J_n(\eta_0 r)\Big|_{r=b}\Big)
$$

(8)

The numerical evaluation of Equation 8 was performed in custom-written MATLAB code. The infinite series over n was truncated at an adjustable order N_{max}. The continuous integration variable h was discretized by $h = \Delta h \cdot m$, $m \in \mathbb{Z}$, and the integral was replaced by a sum within the limits $[-M_{max}, M_{max}]$. However, by discretizing the spectrum, the spatial current distribution becomes periodic. Therefore, the calculated impedance refers to an array configuration, which is periodic in the z-direction. The spatial periodicity L is thereby inversely proportional to the discretization step Δh: $L = \frac{2\pi}{\Delta h}$. It is essential to keep $L \gg 2d$ to make sure that the fields radiating from the periodic alias loops do not interact with the fields of the fundamental loop. We chose a maximum order N_{max} of 50 and, for the discretization of the spatial frequency variable h, we chose a step width of $\Delta h = 2$ (unit is 1/m) and $M_{max} = 2000$. This results in a spatial periodicity L of π m, which is much larger than the coil length $2d$ of 10 cm.

2.2 | Experimental evaluation

To validate the modeling, we experimentally measured the two-port S-parameter matrix for the setup shown in Figure 1 at four frequencies, i.e. 64, 124, 300 and 400 MHz, using a network analyzer (E5071C, Agilent Technology, Santa Clara, CA, USA). The open-port impedance matrices Z were calculated from the S-matrices.[19] Then, the electric k_e and magnetic k_m coupling coefficients were evaluated as $k_e = \text{Real}(Z_{12})/[\sqrt{\text{Real}(Z_{11})\text{Real}(Z_{22})}]$ and $k_m = \text{Im}(Z_{12})/(2\pi f\sqrt{L_1 L_2})$, where L_1 and L_2 are the loop inductances.

In the case of two coupled loops, where each loop is connected to a source through a matching network, an equivalent schematic can be simplified as shown in Figure 2A. Under the condition of weak coupling ($|Z_{12}| \ll R$, where R is the total loop losses), S_{12} can be evaluated as:[19]

$$
S_{12} = \frac{2RZ_{12}}{4R^2 - Z_{12}^2} \approx \frac{Z_{12}}{2R} = \frac{i\omega L_{12} + R_{12}}{2R} = \frac{i\omega k_m L + R_{12}}{2R} = \frac{1}{2}(ik_m Q + k_e)
$$

(9)

where L is the inductance of each loop, $k_m = L_{12}/L$, $k_e = R_{12}/R$ and $Q = \omega L/R$. It is worth noting that, in Equation 9, k_m is multiplied by Q and thus generally has a much greater contribution than k_e to S_{12}.

The loops were constructed of 1.5-mm copper wire and placed on a cylindrical FR4 plastic holder with an outer diameter of 215 mm (wall of 2.5 mm). Each loop measured 100 mm in length (along the holder's central axis) and 80 mm in width (42.5° coverage). To tune each loop to different frequencies, a number of fixed capacitors (100B series, American Technical Ceramics, Huntington Station, NY, USA) and one variable capacitor were uniformly distributed along the loop length. At 64 MHz, the loops contained two fixed capacitors of approximately 43 pF; at 124 MHz, four capacitors each measured 22 or 24 pF; at 300 MHz, eight capacitors each measured 7.5 or 8.2 pF; and at 400 MHz, 10 capacitors each measured 5.6 or 6.2 pF. As an example, Figure 2B shows a schematic of the 400-MHz loop. For S-parameter measurements, each loop was interrupted at a single place (near capacitor 1, Figure 2B), where a calibrated probe was connected. To avoid interaction of the tuned loop with the cable shield, each probe had a cable trap.

For S-matrix measurements, a cylindrical phantom with an inner diameter (ID) of 170 mm was placed symmetrically inside the holder. The phantom was constructed to mimic tissue properties at 400 MHz.[2,20] The relative permittivity ε_r and conductivity σ were measured using a
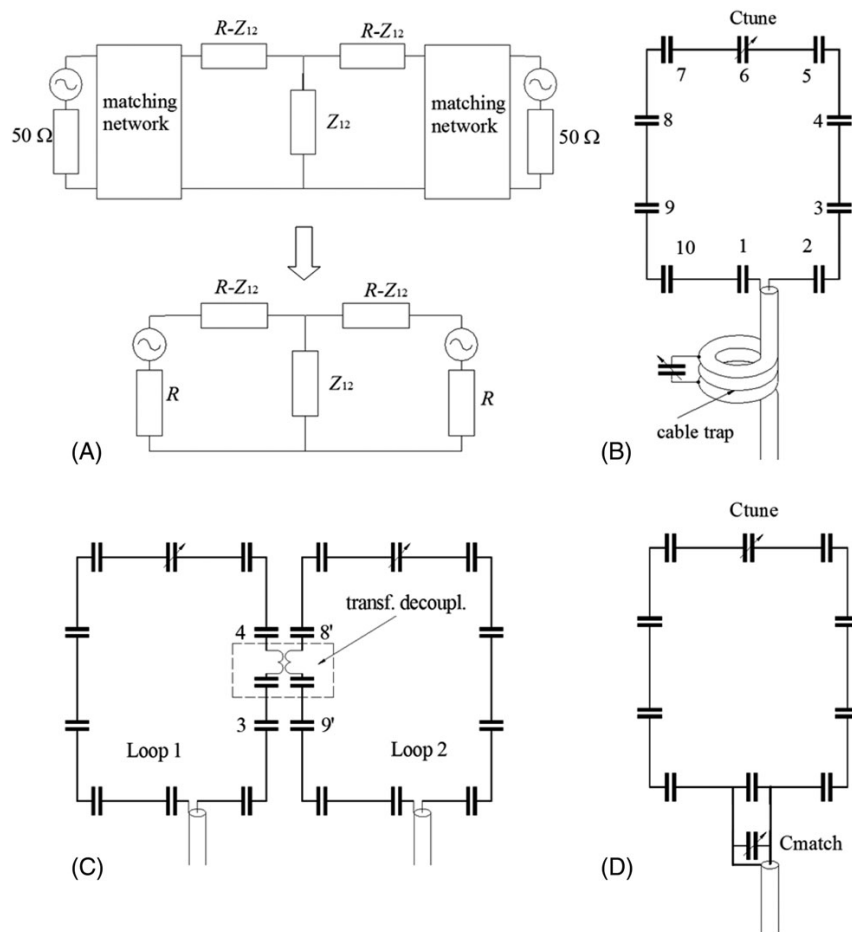
FIGURE 2 (A) equivalent schematic of the matched and coupled two-loop setup. (B) schematic of a 400-MHz loop used in bench measurements. (C) schematic of a two-loop setup with transformer decoupling (TD). (D) schematic of a single loop of the two-loop array with the matching network

dielectric assessment kit (SPEAG, Zurich, Switzerland). Table 1 shows ε_r and σ values at all four frequencies. We also utilized a smaller cylindrical phantom (ID of 14 cm), which was constructed using the same solution.

To assess the mutual resistance in the absence of inductive coupling (magnetically decoupled loops), we decoupled the 400-MHz loop pair using the transformer decoupling (TD) method,[2,4,21] as shown in Figure 2C. The TD circuit was constructed using a 1-mm enameled copper magnet wire as described previously.[4] Two capacitors of 8.2 pF were connected in series with both transformer windings (Figure 2C) to compensate for their inductances. We then measured S-matrices for four α values, i.e. 37°, 40°, 45° and 48°, close to the α angle corresponding to the largest negative mutual inductance (α = 42.5°).

As the analytical modeling does not include the intrinsic coil losses, when evaluating R_{12} we also performed bench measurements of the intrinsic coil losses (unloaded surface loops). At all frequencies, except 64 MHz, the intrinsic coil losses measured below 10% of the sample losses and did not contribute substantially to the R_{12} evaluation. At 64 MHz, coil losses measured approximately 40% of the sample losses and were taken into account during the experimental evaluation of the R_{12} values.

For the evaluation of the Tx efficiency and SNR, a matching network was added to each loop as shown in Figure 2D. Two arrays with two elements each were constructed and evaluated, i.e. an overlapped array (loops of 100 mm × 105 mm; α ≈ 46°), which was optimized based on analytical modeling, and a gapped array (loops of 100 mm × 80 mm; 12-mm gap; α ≈ 49°), which is similar in size to that previously used in UHF head-sized, tight-fit, eight-loop, single-row (1 × 8) transceiver arrays.[4,6] Both arrays were relatively similar in their total coverage, i.e. 92° and 99° for gapped and overlapped arrays, respectively. Although the gapped array was constructed of 1.5-mm copper wire, the overlapped array

TABLE 1 Electromagnetic properties of the phantom

f (MHz)	64	124	300	400
ε_r	65.5	63.6	59.5	58.6
σ (S/m)	0.43	0.46	0.58	0.64

contained a portion constructed of 5-mm copper strips. To minimize radiation losses,[7,22] these arrays were shielded with a cylindrical shield placed at a distance of 40 mm from the loops. We chose this distance following previously reported data.[4,6,7] The gapped array was decoupled using the TD method. Both arrays were well decoupled when loaded, with S_{12} measuring −26 dB and −42 dB for the gapped and overlapped arrays, respectively. During transmission, we used a two-way splitter and a phase shift of 45° between the channels, which is close to the phase shift between adjacent loops of a 1 × 8 cylindrical array driven in the circular polarized (CP) mode.[4,6] Clearly at UHF, RF shimming is required to optimize B_1^+ distribution, and 45° phase shift may not be an optimal solution. However, as the main purpose of the study was to demonstrate the benefits of larger and overlapped loops, we did not perform any further optimization.

Data were acquired on a Siemens (Erlangen, Germany) Magnetom whole-body, 9.4-T, human MRI system. B_1^+ maps were obtained using the three-dimensional actual flip angle imaging (AFI) sequence[23] (field of view, 244 × 244 × 100 mm^3; voxel size, 1.8 × 1.8 × 5 mm^3; TR_1/TR_2 = 20/100 ms; TE = 4 ms). Experimental SNR was evaluated using three-dimensional gradient echo imaging (GRE) with a low flip angle (field of view, 244 × 244 × 100 mm^3; voxel size, 1.8 × 1.8 × 5 mm^3; flip angle, 6°; TR/TE = 8/2 ms) and the pseudo-multiple replica approach.[24] SNR maps were reconstructed by the sum-of-squares (SoS) combination of the Rx channels.[10] Final SNR maps were corrected for the flip angle variation using AFI B_1^+ maps obtained together with GRE.

2.3 | EM simulations

To cross-validate the experimental measurements and analytical modeling, we simulated the same setup in CST microwave studio 2015 (Darmstadt, Germany). The simulated setup consisted of two wire loops and a dielectric phantom with the same sizes and parameters as used in the experimental evaluation. To avoid short-circuiting of the overlapped loops, we offset the center of the wire of one loop by 2 mm from the center of the other in the radial direction. The only coil losses considered were ohmic losses in the loop conductors as a result of the finite conductivity of annealed copper material. The setup was simulated with standard impedance boundary conditions to save memory. We used a frequency domain solver in combination with a tetrahedral mesh and adaptive mesh refinement. The convergence threshold for the iterative mesh refinement was set to ΔS = 1% (maximum relative change in the absolute value of the S-parameter matrix between two consecutive iterations) and a minimum of three iterations. We used a mesh size of approximately 260 000 tetrahedrons. On our computer (Intel Xeon CPU with four cores @ 2.4 GHz and 24 GB RAM), with the previously described simulation parameters and multithreading acceleration, one simulation required between 45 and 90 min depending on the frequency and solver iterations, for the adaptive meshing algorithm. The results of the three-dimensional full-wave EM simulations were fed into a circuit co-simulation environment (CST Design Studio) as an S-parameter block. Both loops were tuned to the corresponding Larmor frequency. Finally, the two-port impedance matrix was extracted. The analytical model did not include the shield which was utilized in our experimental measurements. Therefore, we evaluated the effect of the shield on k_m and k_e at 400 MHz using EM simulations.

3 | RESULTS

3.1 | Validation of the analytical model

At first, we cross-validated the analytical model against bench measurements and CST simulations at all four frequencies. Figure 3A–D shows four k_m and k_e dependences on α. Figure 3E, F demonstrates the magnified k_m and k_e plots shown in Figure 3C, D, respectively.

There was a very large difference in the required simulation time between the commercial CST frequency domain solver and our analytical solver. For example, at 400 MHz, the total time required for 16 data points by the EM solver (Figure 3B, 'CST' curve) was about 24 h on our dedicated CST workstation. In contrast, analytical simulations of 100 data points (Figure 3B, 'model' curve) were obtained in about 3 min on a standard desktop computer.

All EM simulated and experimentally measured curves match each other well at all four frequencies. Analytical k_m dependences are also very similar to the simulated and experimental ones with some differences at smaller angles (α < 40°), where the loops overlap. For example, the first α-axis zero-crossing point, where the mutual inductance is fully compensated (L_{12} = 0) by geometrical overlap (α_{cm}), occurs for all four frequencies at α_{cm} ≈ 35°–36° for simulated and experimental plots, whereas analytical modeling shows α_{cm} ≈ 37°–38°, i.e. with a difference of approximately 5–6%. Analytical k_e plots also match simulated and experimental data well at lower frequencies (64 and 124 MHz). At higher frequencies (300 and 400 MHz), a large difference is observed between the analytical k_e curves and simulations and bench measurements, when a significant magnetic coupling ($|k_m|$ > 0.02) is present. The effect is more pronounced at 400 MHz (Figure 3D). Δk_e (the difference between k_e obtained from simulations or experiments and k_e obtained from analytical modeling) has the same sign as the k_m value, i.e. for large negative k_m (α ~ 42.5°), we measured negative Δk_e, whereas, for large positive k_m (α < 35°), we observed positive Δk_e.

Hypothesizing that the effect of the 'inductively induced mutual resistance' is associated with the presence of the large mutual inductance, we repeated EM simulations and bench measurements for a pair of magnetically decoupled (k_m = 0) loops. In both experiments and simulations, we introduced TD circuits, as shown in Figure 2C. Figure 4 demonstrates the results of these simulations and measurements. As can be seen, all k_e plots (analytical, simulated and experimental) match each other well. Some differences are still observed for large loop overlaps (α < 30°), which, however, are not commonly used in practice when designing loop arrays.

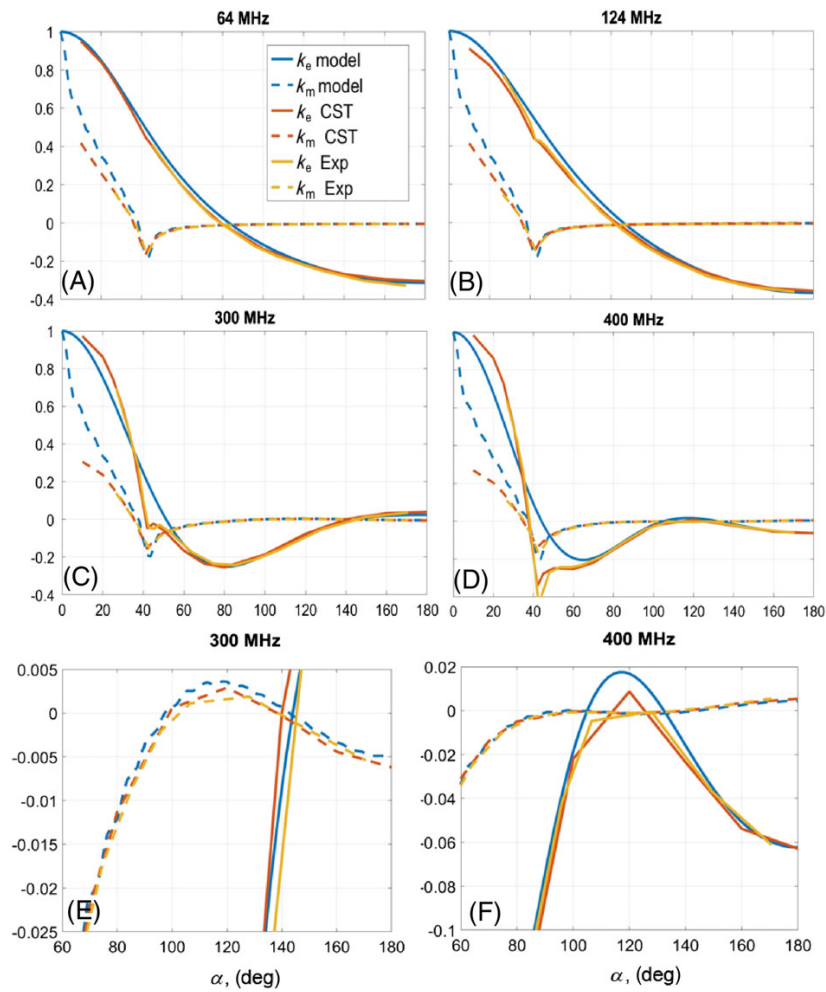**FIGURE 3** Dependence of the magnetic (k_m) and electric (k_e) coupling on the angle between the loop centers (α) obtained using the analytical model, electromagnetic (EM) simulations (CST) and bench measurements at 64 MHz (A), 124 MHz (B), 300 MHz (C) and 400 MHz (D). Magnified k_m and k_e plots obtained at 300 MHz (E) and 400 MHz (F). The magnified plots shown in (E) and (F) correspond to the plots shown in (C) and (D), respectively
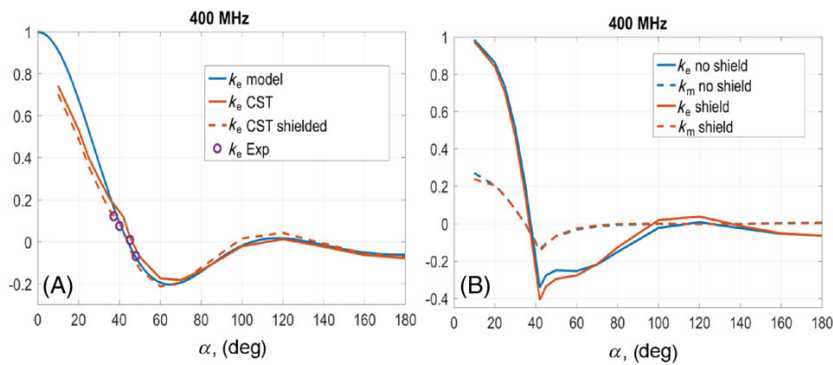

FIGURE 4 (A) dependence of k_e on the angle between the loop centers (α) with transformer decoupling ($M = 0$) using the analytical model, electromagnetic (EM) simulations and bench measurements at 400 MHz. Results of the EM simulations are shown for both the shielded and unshielded two-loop setups. Analytical and experimental data were obtained without the shield. (B) comparison of EM-simulated k_m and k_e plots calculated for the shielded and unshielded two-loop setups at 400 MHz

It is noteworthy that magnetic decoupling is a common feature of most previously described phased arrays, and thus we further evaluated whether $|k_m| < 0.02$, when k_e prediction based on the analytical model is accurate, is achieved under realistic conditions. Using Equation 9 and the lower limit values for S_{12} and the loaded Q-factor, we can estimate the maximal absolute k_m value for a pair of magnetically decoupled loop elements of a phased array. For example, for S_{12} of −13 dB and Q of 30, we obtain, using Equation 9, $k_m = 0.015$, which matches the above criterion. Both of these values (S_{12} = −13 dB and Q = 30) are very conservative. In practice, arrays need to be better decoupled (e.g. $S_{12} \leq$ −20 dB) and Q is usually higher (especially for larger Tx-only arrays), resulting in an even smaller k_m. Thus, for magnetically decoupled arrays, the analytical model evaluates k_e at higher frequencies reasonably well.

Figure 4 also includes the k_e curve calculated by EM simulations for the shielded loops at 400 MHz. No significant difference was observed between shielded and unshielded cases.

3.2 | Analysis and loop geometry optimization

After validation, we used the analytical model to evaluate k_m and k_e dependences on various parameters, including the frequency, loop size and phantom diameter. Figure 5 shows the results of the modeling. As a reference, Figure 5A summarizes the analytical data shown in Figure 3. Magnetic coupling demonstrates a well-known angle dependence with the fully compensated mutual inductance (L_{12} = 0) at the critical overlap ($\alpha = \alpha_{cm} \sim$ 37–38°) and the highest negative k_m at α = 42.5°, corresponding to the window opening of the rectangular loop.[10-12] Interestingly, k_e also changes its sign and is fully compensated at a specific angle ($\alpha = \alpha_{ce}$), which has a strong frequency dependence. This cancellation effect has been shown previously for the flat,[11] spherical[25] and cylindrical[12] sample geometries at lower fields (≤3 T), and can be properly described only by using a full-wave solution. The quasi-static approximation does not reveal such behavior.[10] Both lower frequency k_e plots are very similar with some difference in the k_e value at 180° separation, i.e. −0.3 at 64 MHz *versus* − 0.36 at 124 MHz. The k_e value of −0.36 means that even 180° separated loops can be decoupled no better than −15 dB. At both frequencies, α_{ce} is much larger than α_{cm} and measures ~85° to 90°, which is similar to previously reported values.[12] It is also worth noting that, at $\alpha = \alpha_{cm}$, k_e measures ~0.5–0.6, which corresponds to the S_{12} limit of −10 to −12 dB. Such poor S_{12} values compromise both the decoupling and SNR for multi-channel overlapped loop arrays at lower frequencies (64 and 124 MHz). At higher frequencies, the k_e plot changes significantly and shows a substantially decreased α_{ce} value. This implies that k_e, and thus S_{12}, also decrease for critically overlapped loops ($\alpha = \alpha_{cm}$). At the larger phantom size, both crossing points come even closer to each other. As a result, at 400 MHz, k_e measures ~0.2 at the critical overlap, which corresponds to a reasonable S_{12} of −20 dB. Thus, at UHFs, overlapped arrays can be constructed without compromising decoupling.

At 9.4 T (400 MHz), using the geometry of Figure 5A as a basis, we further optimized a two-loop array by changing the loop's width. Figure 6 shows both k_m and k_e plots with the width changing from 80 to 120 mm, and the other parameters kept the same as in Figure 5A. As can be seen,
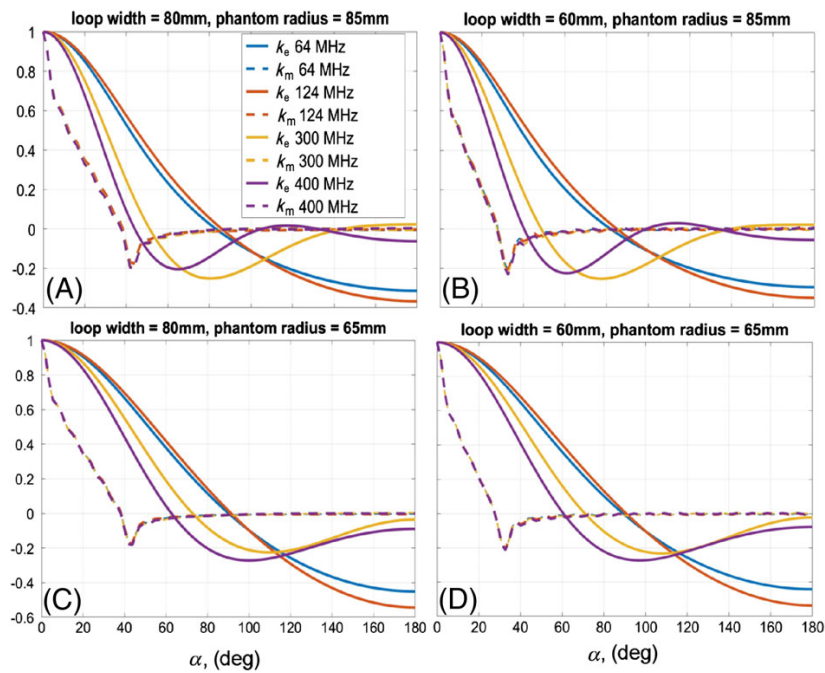

FIGURE 5 Analytical k_m and k_e plots calculated at four frequencies for various loop widths and phantom radii a, i.e. width = 80 mm, a = 85 mm (A), width = 60 mm, a = 85 mm (B), width = 80 mm, a = 65 mm (C) and width = 60 mm, a = 65 mm (D). The loop length $2d$ measured 100 mm in all four cases
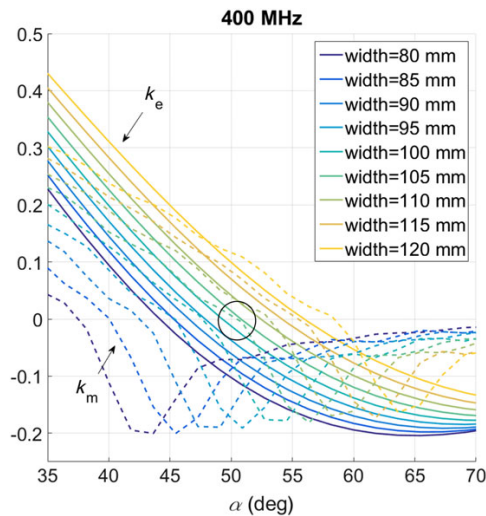
FIGURE 6 Analytical k_m and k_e plots calculated at 400 MHz for the loop width changing from 80 to 120 mm. The other parameters are the same as in Figure 5A

both k_m and k_e curves cross the zero point at the same angle ($\alpha \approx 50°$) for loops with a width of 105 mm. Thus, both magnetic and electrical coupling can be compensated at the same time simply by overlapping without using additional decoupling circuits.

In contrast with the magnetic coupling, electrical coupling strongly depends on loading. Therefore, to make sure that, on variation of loading, the decoupling is not compromised, we also evaluated a change in the residual electrical coupling between a pair of magnetically decoupled ($k_m = 0$) loops loaded with the smaller 14-cm cylindrical phantom placed at various distances from the loops. For these measurements, we used the setup shown in Figure 2C. Figure 7A demonstrates a dependence of the residual k_e value on the distance. Figure 7B shows the achievable decoupling (S_{12}) for the same two loops when they were matched (Figure 2D). In every measurement, TD was slightly adjusted to obtain the lowest S_{12} value to ensure that the magnetic coupling was completely cancelled. As can be seen from Figure 7, k_e increases from -0.3 to ~ 0.2 with the distance to the phantom changing from 10 to 60 mm, with the worst S_{12} of approximately -16.5 dB measured at a distance of 10 mm.

Finally, Figure 8 shows B_1^+ and SNR maps obtained using both two-loop arrays, i.e. the optimized overlapped array (loops of 105 mm × 100 mm) and a gapped array (loops of 80 mm × 100 mm; gap of 12 mm), similar to that which has been used previously for head UHF transceiver arrays.[4,6] For the overlapped array, S_{12} measured below -40 dB. For the gapped array, we measured S_{12} of -26 dB with the mutual inductance completely cancelled. We can then estimate the residual electrical coupling, i.e. $|k_e| \sim 0.1$, which agrees with the analytically evaluated value of -0.08 for $\alpha = 49°$ (Figure 6).

4 | DISCUSSION

We have developed an analytical model to describe the Z-matrix for two loaded rectangular wire loops placed on a cylindrical surface. The model evaluates the coupling between the loops, including both the magnetic k_m and electrical k_e components. Comparison of the analytical, EM-simulated and experimentally measured data shows that our model provides a good match with experimentally measured and simulated k_m for all frequencies and practically applicable overlaps ($\alpha > 30°$). As an example, Figure 3E, F shows magnified plots obtained at two higher frequencies and $\alpha > 60°$. All curves match each other very well, even for small k_m values ($k_m \leq 0.01$). As evident from Equation 9, such accurate evaluation of k_m is quite essential, especially for high Q_L values (low sample loading), e.g. larger Tx-only arrays. Analytical k_e plots match simulated and experimental data well at lower frequencies (64 and 124 MHz). At higher frequencies (300 and 400 MHz), analytical results also match the simulations and experimental data for magnetically decoupled loops, i.e. when the magnetic coupling is sufficiently low ($|k_m| < 0.02$).

The mismatch in k_e values between analytical modelling and numerical and experimental evaluation in the case of large mutual inductance, i.e. the 'inductively induced mutual resistance', most probably occurs because of the assumption in the analytical model that currents in both loops are independent of each other. In contrast, they influence each other by mutual inductive coupling. Obviously, such coupling would produce a correlation of currents, and therefore a correlation of electrical fields generated by both loops. This also explains well the frequency dependence of the effect seen in Figure 3. For our work, however, this effect is not critical as most practical Tx arrays have the mutual inductance compensated. Nevertheless, as it may become important for some specific array designs, we plan to investigate this effect in the future.

After validation, the analytical model was utilized to investigate the dependence of the coupling on various parameters, including the loop size, the angle between the loops, the distance to the sample (loading) and the resonance frequency. Figure 5 shows variations in these parameters. As can be seen from the plots, k_m remains practically unchanged (below 10–15%) with the frequency and sample loading (phantom size). However,
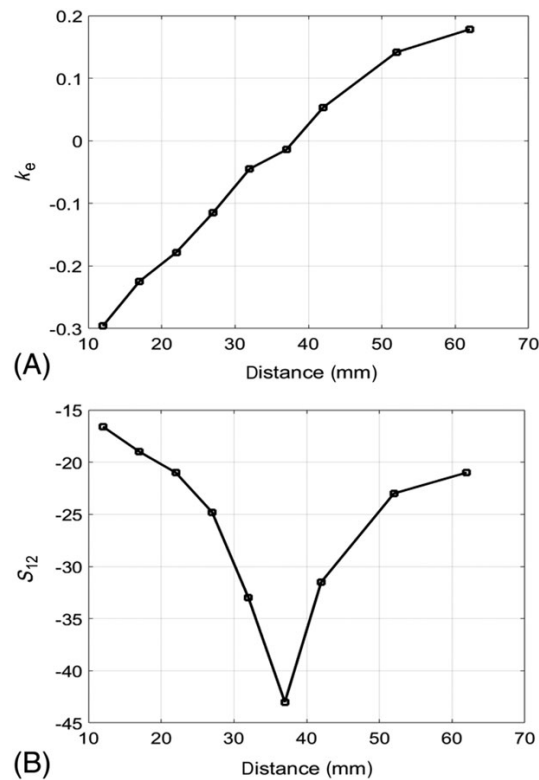
FIGURE 7 k_e (A) and S_{12} (B) dependences on the distance between the surface loops and the phantom obtained using the two-loop gapped array and the 14-cm phantom

changing the loop size (whilst keeping the other parameters the same) influences k_m significantly more than k_e. Alternatively, changing the distance to the phantom by reducing its radius and frequency affect k_e plots drastically. Thus, for a pair of loops, k_m and k_e can be varied relatively independently of each other, which helps to optimize the array geometry. As a result, the decrease in the distance to the phantom (loading) and the increase in the loop's width at higher frequencies bring α_{ce} much closer to α_{cm}, which allows for compensation of both electric and magnetic coupling simply by overlapping without using any additional decoupling circuits.

The relative independence of the mutual inductance on loading is quite important and worthy of discussion. It is also worth noting that the well-known fact that S_{12} between elements of a phased array strongly depends on the loading is explained by changes in the Q-factor rather than in k_m (Equation 9). The independence of k_m on loading is important for practical reasons, as it implies that nearly optimal magnetic decoupling between adjacent elements can be obtained at various loading conditions by using the same detuning circuit optimized for a phantom, which loads the loops similarly to an average sized subject. On the contrary, the electrical coupling strongly depends on the distance to the phantom (loading) and, furthermore, cannot be compensated using common decoupling techniques. Therefore, a knowledge of k_e variation with changing distance to the sample is very critical. For example, as can be seen in Figure 7, to keep S_{12} better than −20 dB ($|k_e| < 0.2$), we have to keep said distance between 20 and 60 mm, which well suits the purpose of constructing a human head phased array and covering practically the entire range of head sizes and shapes. Complete cancelation of the electrical coupling is achieved at a distance of ~37 mm. It is noteworthy that k_e changes its sign when the phantom is moved away from the loops (Figure 7). This dependence of the mutual resistance on the distance to the sample can be qualitatively explained in the following way. Resistive coupling is determined by the sample conductivity and the mutual orientation of the electrical fields produced by the two loops. As described earlier by Hayes and Roemer,[26] near the loops, mutual orientation of electrical fields, and hence noise correlation, is negative, whereas, further away from the loops, it is positive. Moving the sample away from the loops changes the relative contributions of the negative and positive correlation, thus affecting the total k_e value.

Based on the above analysis, a two-loop, 400-MHz array was further optimized. We started with holder and loop sizes similar to those used in previous eight-channel (1 × 8) human head UHF transceiver arrays.[4,6] As can be seen in Figure 5A, k_e is ~0 at $\alpha \approx 45°$, which corresponds to adjacent loops in the 1 × 8 array. Next, we needed to decrease the k_m value without substantially modifying k_e. As k_m is affected more than k_e by changing the loop size, decoupling can be optimized simply by increasing the loop size, whilst keeping the distance to the phantom the same. As can be seen in Figure 6, both k_m and k_e plots cross the α-axis at a slightly larger angle ($\alpha_{cm} \approx \alpha_{ce} \approx 50°$) for loops with a width of 105 mm. Thus, both the electrical and magnetic couplings between adjacent loops were perfectly compensated at the same time and a very good decoupling was obtained simply by overlapping the loops.
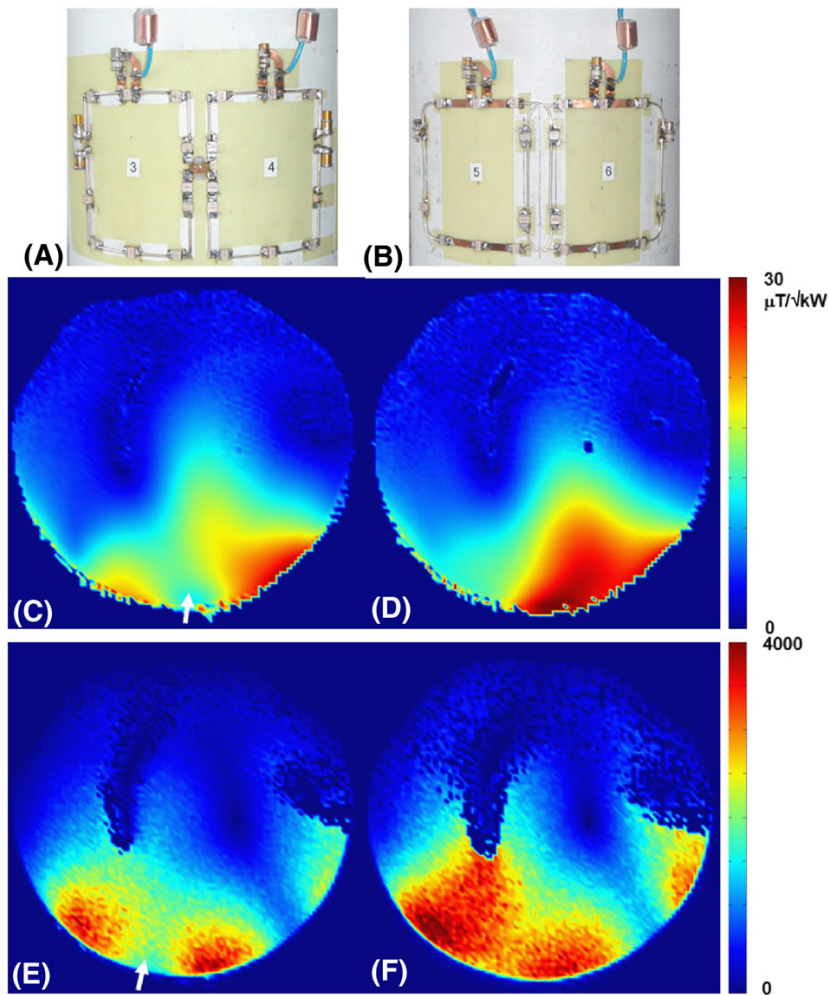
FIGURE 8 Photographs of the gapped (A) and overlapped (B) two-loop, 9.4-T (400-MHz) arrays. B_1^+ transversal maps obtained in the middle of the loops using the gapped (C) and overlapped (D) two-loop, 9.4-T arrays. Signal-to-noise ratio (SNR) transversal maps obtained in the middle of the loops using the gapped (E) and overlapped (F) two-loop, 9.4-T arrays. Voids of the radiofrequency (RF) field and SNR, corresponding to the gaps between the loops, are marked by arrows in (C) and (E)

Following this recipe, we constructed a two-loop, overlapped, 400-MHz array with decoupling between the loops below −40 dB. Finally, we compared the Tx and Rx performances with those of the gapped array, which was similar in size to previously described transceiver 9.4-T arrays.[6] As can be seen in Figure 8, the use of larger and overlapped loops allowed for improvement in both Tx performance and SNR, exhibited by the elimination of voids between the loops and increased penetration depth. It is noteworthy that both the SNR and B_1^+ maps are asymmetrical and skewed in opposite directions. This is explained by the fact that, although Tx excitation is determined by B_1^+ distribution, the reception is defined by the B_1^- profile.[27] It has also been reported previously that this opposite skew is typical for B_1^+ and B_1^- distributions of a surface loop at UHF.[28] Combining together multiple loops circumscribing the entire head into an array (e.g. eight-loop array) will circumvent this effect and provide good coverage for both Tx and Rx profiles. Preliminary results reported for an eight-loop, single-row, overlapped, 9.4-T human head array confirm this fact.[29] The above analysis demonstrates that overlapping can be a very useful decoupling technique for the construction of single-row (1 × 8) and double-row (2 × 8), multi-channel, tight-fit, RF transceiver head arrays at UHFs.

5 | CONCLUSIONS

To provide insight into coupling between the elements of a phased array, we developed an analytical model describing the Z-matrix for two loaded rectangular wire loops placed on a cylindrical surface. The model evaluates the complex coupling between the loops, including both the electric (mutual resistance) and magnetic (mutual inductance) components. Validation of the model using EM simulations and bench measurements demonstrated that it describes well the coupling between the loops at lower fields (≤3 T), as well as at UHFs, for the case of low magnetic coupling

($|k_m| \leq 0.02$). By providing a quick and reasonably accurate evaluation of the complex coupling between the elements of multi-channel transceiver arrays, the analytical model can significantly accelerate the array optimization process. Finally, by using our model, we optimized the geometry of a 9.4-T, two-loop transceiver array, such that, through a simple overlap of the loops, both the mutual inductance and mutual resistance were simultaneously compensated. As a result, nearly perfect decoupling (below −40 dB) were obtained without any additional decoupling circuits.

ACKNOWLEDGEMENTS

REFERENCES

1. Adriany G, Auerbach EJ, Snyder CJ, et al. A 32-channel lattice transmission line array for parallel transmit and receive MRI at 7 tesla. *Magn Reson Med*. 2010;63(6):1478-1485.

2. Shajan G, Kozlov M, Hoffmann J, Turner R, Scheffler K, Pohmann R. A 16-channel dual-row transmit array in combination with a 31-element receive array for human brain imaging at 9.4 T. *Magn Reson Med*. 2014;71:870-879.

3. Adriany G, Van de Moortele P-F, Ritter J, et al. A geometrically adjustable 16-channel transmit/receive transmission line array for improved RF efficiency and parallel imaging performance at 7 tesla. *Magn Reson Med*. 2008;59:590-597.

4. Avdievich NI. Transceiver phased arrays for human brain studies at 7 T. *Appl Magn Res*. 2011;41(2):483-506.

5. Gilbert KM, Belliveau J-G, Curtis AT, Gati JS, Klassen LM, Menon RS. A conformal transceive array for 7 T neuroimaging. *Magn Reson Med*. 2012;67:1487-1496.

6. Avdievich NI, Hoffmann J, Shajan G, et al. Evaluation of transmit efficiency and SAR for a tight fit transceiver human head phased array at 9.4 T. *NMR Biomed*. 2017;30(2):1-12.

7. Vaughan JT, Garwood M, Collins CM, et al. 7T vs. 4T: RF power, homogeneity, and signal-to-noise comparison in head images. *Magn Reson Med*. 2001;46:24-30.

8. Kang C-K, Hong S-M, Han J-Y, et al. Evaluation of MR angiography at 7.0 tesla MRI using birdcage radio frequency coils with end caps. *Magn Reson Med*. 2008;60:330-338.

9. Avdievich NI, Pan JW, Hetherington HP. Resonant inductive decoupling (RID) for transceiver arrays to compensate for both reactive and resistive components of the mutual impedance. *NMR Biomed*. 2013;26(11):1547-1554.

10. Roemer PB, Edelstein WA, Hayes CE, Souza SP, Mueller OM. The NMR phased array. *Magn Reson Med*. 1990;16:192-225.

11. Wright SM. Full-wave analysis of planar radiofrequency coils and coil arrays with assumed current distribution. *Concepts Magn Reson B: Magn Reson Eng*. 2002;15(1):2-14.

12. Wei P-S, King SB, Smith MJ, Matwiy J, Bidinosti CP. Accurate phased array modeling in the presence of coupling. *Proceedings of the 21st Annual Meeting ISMRM*, Salt Lake City, UT, USA, 2013; 2721.

13. Vesselle H, Collin RE. The signal-to-noise ratio of nuclear magnetic resonance surface coils and application to a lossy dielectric cylinder model. Part I. Theory. *IEEE Trans Biomed Eng*. 1995;42:497-506.

14. Vesselle H, Collin RE. The signal-to-noise ratio of nuclear magnetic resonance surface coils and application to a lossy dielectric cylinder model – Part II: The case of cylindrical window coils. *IEEE Trans Biomed Eng*. 1995;42:507-520.

15. Schnell W, Renz W, Vester M, Ermert H. Ultimate signal-to-noise-ratio of surface and body antennas for magnetic resonance imaging. *IEEE Trans Antennas and Propagation*. 2000;48:418-428.

16. Lattanzi R, Sodickson D. Ideal current patterns yielding optimal signal-to-noise ratio and specific absorption rate in magnetic resonance imaging: Computational methods and physical insights. *Magn Reson Med*. 2012;68:286-304.

17. Harrington R. *Time-Harmonic Electromagnetic Fields*. New York: McGraw-Hill; 1961.

18. Tai C-T. Dyadic Green Functions in Electromagnetic Theory. *IEEE Press Series on Electromagnetic Waves*. New York: IEEE Press; 1994.

19. Pozar DM. *Microwave Engineering*. Danvers, MA: John Wiley & Sons; 2011.

20. Beck BL, Jenkins KA, Rocca JR, Fitzsimmons JR. Tissue-equivalent phantoms for high frequencies. *Concepts Magn Reson B*. 2004;20:30-33.

21. Kokubunji TN, Soka TT, Kashiwa YM, Akishima EY, Katakura K. RF probe for MRI. *US Patent*. 1994;5,489,847:

22. Harpen MD. Radiative losses of a birdcage resonator. *Magn Reson Med*. 1993;29:713-716.

23. Yarnykh VL. Actual flip-angle imaging in the pulsed steady state: A method for rapid three-dimensional mapping of the transmitted radiofrequency field. *Magn Reson Med*. 2007;57:192-200.

24. Robson PM, Grant AK, Madhuranthakam AJ, Lattanzi R, Sodickson DK, McKenzies CA. Comprehensive quantification of signal-to-noise ratio and g-factor for image-based and k-space-based parallel imaging reconstructions. *Magn Reson Med*. 2008;60:895-907.

25. King SB, Duensing GR. Zero shared resistance between coil elements of a phased array? *Proceedings of the 8th Annual Meeting ISMRM*, Denver, CO, USA, 2000; 1406.

26. Hayes CE, Roemer PB. Noise correlations in data simultaneously acquired from multiple surface coil arrays. *Magn Reson Med*. 1990;16:181-191.

27. Hoult DI. The principle of reciprocity in signal strength calculations – A mathematical guide. *Concepts Magn Reson*. 2000;12:173-187.

28. Collins CM, Yang QX, Wang JH, et al. Different excitation and reception distributions with a single-loop transmit–receive surface coil near a head-sized spherical phantom at 300 MHz. *Magn Reson Med*. 2002;47:1026-1028.

29. Avdievich NI, Giapitzakis IA, Pfrommer A, Henning A. Optimization of the transceiver phased array for human brain imaging at 9.4 T: Loop overlapping rediscovered. *Proceedings of the 24th Annual Meeting ISMRM*, Singapore, 2002; 169.

SUPPORTING INFORMATION

Additional Supporting Information may be found online in the supporting information tab for this article.